Probing New Physics with hadronic final states at the Large Hadron Collider

A thesis submitted in partial fulfillment of
the requirements for the degree of

Doctor of Philosophy

by

Akanksha Bhardwaj

(Roll No. 15330012)

Under the guidance of

Dr. Partha Konar

Associate Professor

Theoretical Physics Division

Physical Research Laboratory, Ahmedabad, India.

DEPARTMENT OF PHYSICS

INDIAN INSTITUTE OF TECHNOLOGY GANDHINAGAR

2020

my family

&

teachers

Declaration

I declare that this written submission represents my ideas in my own words and where others' ideas or words have been included, I have adequately cited and referenced the original sources. I also declare that I have adhered to all principles of academic honesty and integrity and have not misrepresented or fabricated or falsi ed any idea/data/fact/source in my submission. I understand that any violation of the above will be cause for disciplinary action by the Institute and can also evoke penal action from the sources which have thus not been properly cited or from whom proper permission has not been taken when needed.

Akanksha Bhardwaj

(Signature)

(Name: Akanksha Bhardwaj)

(Roll No: 15330012)

Date: 09/07/2020

CERTIFICATE

It is certified that the work contained in the thesis titled **"Probing New Physics with hadronic final states at the Large Hadron Collider"** by **Akanksha Bhardwaj** (Roll no. 15330012), has been carried out under my supervision and that this work has not been submitted elsewhere for a degree.

I have read this dissertation and in my opinion, it is fully adequate in scope and quality as a dissertation for the degree of Doctor of Philosophy.

Partha Konar

9 July, 2020

Dr. Partha Konar
(Thesis Supervisor)

Associate Professor
Theoretical Physics Division
Physical Research Laboratory
Navrangpura, Ahmedabad
Gujarat - 380 009, India

Thesis Approval

The thesis entitled

Probing New Physics with hadronic final states at the Large Hadron Collider

by

Akanksha Bhardwaj
(Roll No. 15330012)

is approved for the degree of

Doctor of Philosophy

Examiner

Examiner

Supervisor

Chairman

Date:

Place:

List of Publications

I. Publications contributing to this thesis:

1. **Akanksha Bhardwaj**, Juhi Dutta, Partha Konar, Biswarup Mukhopadhyaya and Santosh Kumar Rai, *"Boosted jet techniques for a supersymmetric scenario with gravitino LSP"* (arXiv:2007.00351 [hep-ph]) (Submitted to **JHEP**)

2. **Akanksha Bhardwaj**, Partha Konar, Tanumoy Mandal, and Soumya Sadhukhan, *"Probing the inert doublet model using jet substructure with a multivariate analysis"* **Phys.Rev. D100 (2019) no.5, 055040** arXiv[1905.04195]

3. **Akanksha Bhardwaj**, Arindam Das, Partha Konar and Arun Thalapillil, *"Looking for Minimal Inverse Seesaw scenarios at the LHC with Jet Substructure Techniques"* **J.Phys. G47 (2020) no.7, 075002** arXiv[1801.00797]

4. **Akanksha Bhardwaj**, Partha Konar , Pankaj Sharma and Abhaya Kumar Swain, *"Exploring CP phase in τ-lepton Yukawa coupling in Higgs decays at the LHC"* **J.Phys. G46 (2019) no.10, 105001** arXiv[1612.01417]

II. Research Papers in Proceedings:

1. **Akanksha Bhardwaj**, Partha Konar and Abhaya Kumar Swain, **DOI:10.1007/978-3-319-73171-1128 (Springer Proc.Phys. 203 (2018) 547-550)**

Acknowledgements

First and foremost, I would like to take this opportunity to express my gratitude towards my PhD supervisor Dr Partha Konar, for his invaluable guidance, encouragement and support throughout the course of this work. His continuous support and positive attitude about everything in life have kept me motivated in all kind of situations. He is an amazing person who has been a good friend, philosopher, and great supervisor throughout my PhD.

I thank all the collaborators from whom I learnt a lot during my PhD. Firstly I would like to thank my senior Dr Abhaya Kumar Swain to teach me collider physics in the early stage of my PhD. I thank Dr Pankaj Sharma, Dr Arun thalapilil, Dr Arindam Das, Dr Soumya Sadhukhan and Dr Tanumoy Mondal, Dr Juhi Dutta, Prof. Santosh Kumar Rai, Prof. Biswarup Mukhopadhyaya for collaborating and pursuing some exciting physics with me.

I take this opportunity to thank my Doctoral Studies Committee, Prof. Srubabati Goswami and Prof. Hiranmaya Mishra for evaluating my work regularly. Their valuable comments helped me to improve scientific outcomes. I am also grateful to them for the examination of this thesis.

I would like to thank Prof. Saurabh D. Rindani, Prof. Subhendra Mohanty, Prof. Dilip Angom, Prof. Jitesh R. Bhatt, Prof. Srubabati Goswami, Prof. Raghavan Rangarajan, Prof. Hiranmaya Mishra, Dr Namit Mahajan, Dr Partha Konar and Dr Ketan Patel for teaching many courses in high-energy physics, many-body theory and cosmology during and after the course work.

I thank area chairman Prof. Hiranmaya Mishra for providing necessary facilities to carry out research work. The Theoretical Physics (THE-PH) division provided me with a nice research environment which I always enjoyed. I express my gratitude to all the past and present members of the division.

I express my gratitude to Prof. Anil Bhardwaj, Director, Physical Research Laboratory (PRL) for providing the necessary facilities to carry out my research work. I thank Mr Jigar Raval and Mr Bhavin for helping with the cluster computing in PRL. I am grateful to Indian Institute of Technology, Gandhinagar (IIT Gn) for my PhD registration.

I thank the entire family of PRL for all the research facilities and for providing an excellent hostel the facility at Thaltej.

Office no. 770 turns out to be a wonderful place in my PhD life. Five years ago when I joined as a first-year student I met with some of the most amazing people in my life. Everybody in the office was so learned persons in not only physics and but also in philosophy. Glab Bhai, Ujjal Da, Lata di, Tanmoy and Abhaya. Later *when they left it was joined by new enthusiastic people about physics with Balbeer, Selvaganpay, Vishal, Sudipta and Anupam. It is the smallest space where I gain most of my knowledge of physics and about life.*

It would have been impossible to pass the five years without the joyful company of my dear batch mates, all the seniors and juniors in PRL. A special mention of Shivangi who helped me through challenging times, we have shared some very difficult experiences during the pandemic. Thank you for your constant support and friendship. I would also like to thank Ila and Nisha for being my hiking partners whom company I thoroughly enjoyed. I thank my friends from college and school days– Pooja, Poonam, Jyoti and Gunjan who always kept me cheerful.

I thank my father Mr Pramod Kumar Bhardwaj, my mother Mrs Vimla Bhardwaj, sister Anjali and brother Ankit for their constant support, encouragement, love and care throughout my life.

(Akanksha)

Abstract

The Large Hadron Collider (LHC) fixes the last missing bit of the Standard Model by the remarkable discovery of the Higgs boson in 2012. The LHC now opens a new paradigm with the underlying motivation for determining properties of the Higgs boson and searching for new physics.

Many BSM theories predict heavy resonances which predominantly decay to particles like W, Z, the Higgs boson or the top quark. Study of these model in hadronic final states become very important due to high branching fraction of these particles into jets. However, large QCD background makes the study of hadronic final states remarkably difficult. Recent techniques like jet substructure can be very useful in studying the boosted jets produced through the decay of highly energetic heavy particle. Many jet substructure variables are proposed which are inspired by the idea of different energy distribution between the decay of heavy boosted particle and fragmentation of highly energetic partons. These techniques are utilized to explore the TeV scale BSM models. In this thesis, we explore BSM models such as inverse seesaw, inert doublet model, compressed supersymmetric (SUSY) scenario and CP violation in the Higgs sector. Thes models can address some of the outstanding issues of the SM like neutrino mass generation, dark matter etc. We propose new search strategies using the boosted topology in hadronic final state to probe the BSM physics at the LHC.

First, we discuss the inverse seesaw model which is an elegant and simple mechanism to generate the small neutrino masses at TeV scale together with a large coupling to probe at the LHC. We study collider signatures of heavy pseudo-Dirac neutrinos with a sizable mixing with the SM neutrinos under two different flavour structures, viz., Flavour Diagonal and Flavour Non-Diagonal scenarios. We probe the heavy pseudo-Dirac neutrinos with the opposite-sign di-lepton associated with a fat jet signature at the LHC. The heavy mass sterile neutrinos decay leads to boosted fat jets arising from W boson hadronic decays and helps to overcome the enormous background of opposite sign di-lepton. This signature is very important as it is the characteristic for a class of models with Dirac or pseudo-Dirac type neutrinos. We perform a comprehensive collider analysis to

demonstrate the effectiveness of this channel in both scenarios. The bounds on the right-handed neutrino mass and mixing angles are significantly enhanced and are at least an order of magnitude better than existing limits at the 13 TeV LHC.

Next, we explore the Inert Doublet Model (IDM) which is a minimal extension of the SM that can provide a viable dark matter (DM) candidate which satisfies the observed relic density in different parameter region of the model. We study the challenging hierarchical mass spectrum of the IDM where relatively light dark matter along with much heavier scalar states can fully satisfy the constraints on the relic abundance along with all other theoretical, collider and the astrophysical bounds. The significant mass differences between DM candidate and other scalars present in the model give rise to interesting signal topology characterized by two boosted jets along with large missing transverse energy (MET) from the DM production. With this topology, we capture a hybrid process where the di-fat jet signal is significantly enhanced by the mono-fat jet contribution. We adopt the method of multivariate analysis using jet-substructure observable as inputs. This study brings the entire parameter space well within reach of the 14 TeV LHC runs with the first phase of high luminosity (HL-LHC).

We also study the compressed SUSY scenarios with a higgsino-like $\widetilde{\chi}_1^0$ as the next-to-lightest sparticle (NLSP) and a light keV-scale gravitino ($\widetilde{G}$) as the LSP and potential dark matter candidate. A multi-TeV scale higgsino like NLSP decays highly boosted Higgs or Z bosons along with large MET. At this high energy, capturing the Higgs based on double b-tagger will not be useful as b-tagging deteriorates its efficiency at this high momenta. Rather we utilize 2-prong finder to capture Higgs as well as Z boson in the final state. This method can cover up to 3.2 TeV scale of such compressed SUSY spectrum at HL-HLC. We also design observables which can distinguish between the compressed and uncompressed spectrum.

The new physics signature may be hidden inside the Higgs sector itself. Hence the measurements of Higgs properties are crucial. Therefore, we study the CP properties of the Higgs by determining the CP-violating phase in the $H\tau\tau$ Yukawa coupling. In this study, we present the several CP odd observables which are

sensitive to the CP-violating phase of the $H\tau^-\tau^+$ coupling. We also propose a novel method to reconstruct the τ momenta.

In this thesis, we demonstrate the efficacy of jet-substructure variable in various model and probe the most challenging parameter space of these models. The analysis presented in this thesis can be applicable to a wide range of BSM models due to its generic nature.

Keywords: Beyond the Standard Model,Jet substructure, TeV scale seesaw, Extended Scalar Sector, Compressed SUSY, Higgs CP violation, Collider Phenomenology

Contents

List of Figures

List of Tables

List of Abbreviations

2HDM	Two Higgs Doublet Model
AK	Anti-k_T
ATLAS	A Toroidal LHC ApparatuS
BDT	Boosted Decision Tree
BP	Benchmark Point
BSM	Beyond the Standard Model
CA	Cambridge-Aachen
CBA	Cut Based Analysis
CC	Charged Current
CMBR	Cosmic Microwave Background Radiation
CMS	Compact Muon Solenoid
CP	Charge conjugation & Parity
CPV	CP Violation
DM	Dark Matter
ECAL	Electromagnetic Calorimeter
ECF	Energy Correlation Functions
EWPD	Electro-Weak Precision Data
EWSB	Electro-Weak Symmetry Breaking
FD	Flavor Diagonal
FND	Flavor Non-Diagonal
HCAL	Hadronic Calorimeter
HL-LHC	High Luminosity Large Hadron Collider
IDM	Inert Higgs Doublet Model
IH	Inverted Hierarchy
ISR	Initial State Radiation
LEP	Large Electron Positron Collider
LFV	Lepton Flavour Violation
LH	Left Handed
LHC	Large Hadron Collider
LO	Leading Order
LSP	Lightest Supersymmetric Particle
MET	Missing Transverse Momentum
MSSM	Minimal Supersymmetric Standard Model
MVA	MultiVariate Analysis

NC	Neutral Current
NH	Normal Hierarchy
NLO	Next-to Leading Order
NP	New Physics
NSLP	Next-to Lightest Supersymmetric Particle
OSDL	Opposite Sign Di-Lepton
PMNS	Pontecorvo - Maki - Nakagawa - Sakata
QCD	Quantum ChromoDynamics
RH	Right Handed
RHN	Right Handed Neutrino
SM	Standard Model
SUSY	SuperSymmetry
VBF	Vector Boson Fusion
vev	Vacuum Expectation Value
WIMP	Weakly Interacting Massive Particle
ZMF	Zero Momentum Frame

Chapter 1

Introduction

When we try to understand the fundamental laws of Nature, we confront many open questions. Over the past few decades, the field of high energy physics has delivered a lot of potential answers to most of the important questions. The mathematical model of these answers can be summarised in the Standard Model (SM) [1–4] of particle physics. The Standard Model describes the interaction and the dynamics of three fundamental forces (Strong, Electromagnetic and Weak) with the elementary particles. The SM is tested and supported at different energy scale by various experiments, and currently, the Large Hadron Collider (LHC) is exploring the same at multi-TeV scale.

Although the SM encapsulated most of the fundamental issues, there are several unanswered questions, such as non zero neutrino mass, the existence of dark matter, hierarchy problem and baryonic asymmetry. These issues build a strong foundation to search the physics beyond the standard model (BSM). Searching for these new physics models which provide the answers to the aforementioned issues is the underlying motivation for the LHC at present. These search poses new challenges as the new physics is either weakly interacting or at around TeV scale or higher. In this chapter, we briefly discuss the SM, its shortcomings and also why we need to look beyond the SM.

1.1 The standard model

The construction of the Standard Model is based on gauge symmetries. The direct product of three different local gauge symmetries $(SU(3)_C \otimes SU(2)_L \otimes U(1)_Y)$ embeds the gauge group of the SM, where C, L and Y stand for color, left-haded isospin and hypercharge, respectively. The strong sector is governed by the $SU(3)_C$ gauge symmetry while electromagnetic and weak interactions are governed by the $SU(2)_L \otimes U(1)_Y$ gauge group. The particle content of the SM is shown in Tab. 1.1. The matter content of the SM consists of six *quarks* and six *leptons*. Quarks are $SU(3)_C$ multiplets and have strong interactions whereas leptons are singlet under the strong interaction. The fermions are further divided into three generations.

Names	**Fields**	$SU(3)_c$, $SU(2)_L$, $U(1)_Y$
Quarks	$Q^i_L = \begin{pmatrix} u^i_L \\ d^i_L \end{pmatrix}$	(3, 2, 2/3)
	u^i_R	(3, 1, 4/3)
	d^i_R	(3, 1, -2/3)
Leptons	$L^i_L = \begin{pmatrix} \nu^i_L \\ e^i_L \end{pmatrix}$	(1, 2, -1)
	e^i_R	(1, 1, -2)
Gauge bosons	G	(8,1,0)
	$W^\pm, W^3$	(1,3,0)
	B	(1,1,1)
Scalar	Φ	(1,2,-1)

Table 1.1: Particle content of the Standard Model of particle physics.

The electromagnetic interaction is mediated by the photon γ, whereas the $W^\pm$ and the Z (admixture of W^3 and B which is orthogonal to γ) bosons are the mediator of charged and the neutral currents respectively for the weak interaction. The mixing between the W^3 and B will be discussed later in this chapter. The gluons are the mediator for the strong current. The mass of the W and Z bosons are obtained by the symmetry breaking known as *Higgs Mechanism* [5–8]. In this mechanism, the $SU(2)_L \otimes U(1)_Y$ gauge group is broken to $U(1)_{em}$ while the $SU(3)_C$ sector remains unbroken. The interaction of the gauge bosons with the Higgs is given by the kinetic term of the scalar potential whereas fermions interact with the Higgs through Yukawa term. The full Standard Model Lagrangian is composed of four terms,

$$\mathcal{L}_{\rm SM} = \mathcal{L}_{\rm Matter} + \mathcal{L}_{\rm Gauge} + \mathcal{L}_{\rm Scalar} + \mathcal{L}_{\rm Yukawa}. \tag{1.1}$$

We will discuss each term in Eq. 1.1 in this chapter.

1.1.1 Fermion Sector

The fermions are the matter fields of the SM and transform according to their respective charges under the gauge group. The left-handed fields transform as a doublet while the right-handed fields transform as a singlet under $SU(2)$. The gauge-invariant fermion Lagrangian can be written as

$$\mathcal{L}_{\rm Matter} = \sum_f i\,\overline{\psi_f} \not{D} \psi_f, \tag{1.2}$$

where, $\not{D} = \gamma^\mu D_\mu$ with D_μ is the covariant derivative. The covariant derivative for the SM gauge group is given by

$$D_\mu \equiv \partial_\mu + i\, g_s \frac{\lambda^a}{2} G^a_\mu + i\, g \frac{\sigma^a}{2} W^a_\mu + i\, g' \, Y \, B_\mu \,, \tag{1.3}$$

where g_s and g are the gauge coupling constants which determine the strength of strong and weak interaction respectively. The g' is the coupling constant of $U(1)_Y$. Here λ^a $(a = 1, 2, \cdots, 8)$ are the generators of $SU(3)$ and known as the Gell-Mann matrices whereas the Pauli matrices σ^a $(a = 1, 2$ & $3)$ are the generator of $SU(2)$ gauge group. Here G^a_μ, W^a_μ and B_μ are the massless gauge bosons of $SU(3)_C$, $SU(2)_L$ and $U(1)_Y$ respectively.

1.1.2 The Gauge sector

The kinetic term for the gauge boson fields can be written as

$$\mathcal{L}_{\text{Gauge}} = -\frac{1}{4}\, G^{\alpha}_{\mu\nu}\, G^{\mu\nu\alpha} - \frac{1}{4}\, W^{k}_{\mu\nu}\, W^{\mu\nu k} - \frac{1}{4}\, B_{\mu\nu}\, B^{\mu\nu}, \tag{1.4}$$

where $G^{\alpha}_{\mu\nu}, W^{k}_{\mu\nu}$ and $B_{\mu\nu}$ are the field strengths tensor for the vector fields of $SU(3)_C$, $SU(2)_L$, and $U(1)_Y$ respectively, and can be defined as

$$G^{\alpha}_{\mu\nu} = \partial_\mu\, G^{\alpha}_{\nu} - \partial_\nu\, G^{\alpha}_{\mu} - g_s\, f^{\alpha\beta\gamma}\, G^{\beta}_{\mu}\, G^{\gamma}_{\nu}, \tag{1.5}$$

$$W^{k}_{\mu\nu} = \partial_\mu\, W^{k}_{\nu} - \partial_\nu\, W^{k}_{\mu} - g\epsilon^{ijk}\, W^{i}_{\mu}\, W^{j}_{\nu}, \tag{1.6}$$

$$B_{\mu\nu} = \partial_\mu\, B_{\nu} - \partial_\nu\, B_{\mu}. \tag{1.7}$$

Where, $f^{\alpha\beta\gamma}$ represents the total antisymmetric structure constants for $SU(3)_c$ where α, β, and γ are color indices. Similarly, ϵ^{ijk} represents the total antisymmetric structure constants for $SU(2)_L$ with i, j and k being the generation index. The presence of the quadratic term encodes self-interaction of the non-abelian gauge fields. This gives rise to 3-point interaction like $W^+W^-\gamma$, W^+W^-Z and 4-point interaction like $W^+W^-\gamma\gamma$, W^+W^-ZZ, $W^+W^-\gamma Z$, $W^+W^-W^+W^-$ for the $SU(2)_L$ gauge group.

1.1.3 Electroweak symmetry breaking and Higgs mechanism

To explain the experimentally observed non-zero mass of gauge bosons $(W^\pm, Z)$ and fermions, one needs to add a complex $SU(2)$ scalar doublet,

$$\Phi = \begin{pmatrix} \phi^+ \\ \phi^0 \end{pmatrix}, \tag{1.8}$$

where ϕ^+ and ϕ^0 are the complex scalars. The Lagrangian involving the Φ can be written as

$$\mathcal{L}_{Scalar} = (D_\mu \Phi)^\dagger\, (D^\mu \Phi) - V(\Phi). \tag{1.9}$$

In the gauge invariant scalar potential *(Higgs potential)* $V(\Phi)$ takes the form

$$V(\Phi) = -\mu^2\Phi^\dagger\Phi + \lambda(\Phi^\dagger\Phi)^2. \tag{1.10}$$

The Higgs potential develops a non-zero vacuum expectation value for $\mu^2 > 0$,

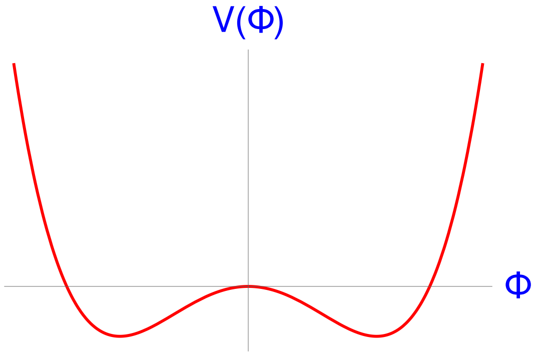

Figure 1.1: The potential $V(\Phi) = -\mu^2\Phi^\dagger\Phi + \lambda(\Phi^\dagger\Phi)^2$ for $\mu^2 > 0$ and $\lambda > 0$.

$\lambda > 0$ as shown in Fig. 1.1. The minimum of $V(\Phi)$ corresponds to

$$\langle\Phi\rangle = \frac{1}{\sqrt{2}}\begin{pmatrix} 0 \\ v \end{pmatrix}, \tag{1.11}$$

where $\langle\Phi\rangle$ is called the *vacuum expectation value (vev)* of Φ with $v = \mu/\sqrt{\lambda}$. The vacuum is no longer invariant under $SU(2)_L \otimes U(1)_Y$ transformations. This is known as *spontaneous symmetry breaking*. Now, in the unitary gauge

$$\Phi = \frac{1}{\sqrt{2}}\begin{pmatrix} 0 \\ v + h(x) \end{pmatrix}, \tag{1.12}$$

where $h(x)$ is the small perturbation around the minimum of the scalar potential. The Higgs mass can be obtained by substituting Eq. 1.12 in the scalar potential given in Eq. 1.10 and can be written as

$$m_h = v\sqrt{2\lambda}. \tag{1.13}$$

The recent discovery of the Higgs with $m_h \sim 125$ GeV fixes the self-interaction strength of the Higgs boson as $\lambda \sim 0.13$ for $v = 246$ GeV.

1.1.4 Generation of the gauge boson masses

The masses of the gauge bosons $(W^{\pm}, Z)$ can be obtained by substituting the *vev* form Eq. 1.12 in the kinetic term of the scalar potential.

$$|D_\mu\phi|^2 = \frac{1}{2}(\partial_\mu h^2) + \frac{g^2v^2}{4}W^+W^- + \frac{v^2}{8}(gW^3_\mu - g'B_\mu)^2 \tag{1.14}$$

. Since $W^{\pm} = \frac{1}{\sqrt{2}}\left(W^1_\mu \mp i\, W^2_\mu\right)$, the mass of the charged gauge boson is given by

$$m_W^2 = \frac{1}{4}\, v^2\, g^2. \tag{1.15}$$

The mass term for the neutral vector bosons can be obtain from the following relations

$$Z_\mu = \cos\theta_w W^3_\mu - \sin\theta_w B_\mu, \tag{1.16}$$

$$A_\mu = \cos\theta_w W^3_\mu + \sin\theta_w B_\mu, \tag{1.17}$$

where θ_w is the weak mixing angle (also known as 'Weinberg angle') and is defined as,

$$\tan\theta_w = \frac{g'}{g}, \qquad \cos\theta_w = \frac{m_W}{m_Z}. \tag{1.18}$$

The mass of the neutral gauge bosons are,

$$\begin{aligned} m_Z^2 &= \frac{1}{4}\, v^2\, (g^2 + g'^2) \\ m_A^2 &= 0. \end{aligned}$$

The gauge bosons become massive after the corresponding generator is broken by the vacuum but photon remains massless respecting the spontaneous breaking of the gauge symmetry. The interaction between the Higgs boson and the gauge bosons is given by the kinetic term in Eq. 1.9 as,

$$D_\mu \equiv \partial_\mu + i\, g_2\, \frac{\sigma^a}{2}\, W^a_\mu + i\, g_1\, \frac{\mathbb{I}}{2}\, B_\mu. \tag{1.19}$$

The relative strength of neutral and charged current weak interaction is determined by the parameter ρ, which is defined as

$$\rho = \frac{m_W^2}{m_Z^2 \cos^2\theta_w}. \tag{1.20}$$

Hence, it follows that $\rho = 1$ at tree level SM.

1.1.5 Yukawa interaction of fermions

Chiral structure of weak interactions prohibits the bare fermion masses within the Standard Model. The fermions masses can be obtained from the Higgs boson through the Yukawa interaction, and can be written as

$$-\mathcal{L}_{\text{Yukawa}} = y_u\,\overline{q_L}\,u_R\,\Phi + y_d\,\overline{q_L}\,d_R\,\tilde{\Phi} + y_e\,\overline{l_L}\,e_R\,\Phi + h.c., \tag{1.21}$$

where $\tilde{\Phi} = i\sigma_2\Phi^*$. The parameters y_u, y_d and y_e are the Yukawa matrices which represent the respective Yukawa couplings. Hence, the masses of the fermions are proportional to their coupling to the Higgs field and given by $m_f = \frac{1}{\sqrt{2}}y_f v$, here, $(f = u, d, e)$. All the above masses are reported at the tree-level.

1.2 New Physics Beyond the SM : Motivations

The SM has been a very successful model and the LHC is continuing its testing at the TeV scale. Still, there are few questions which can not be answered within the SM. Some of these issues are discussed in this section.

1.2.1 Neutrino Masses

The phenomenon of *neutrino oscillation* has been established by many experimental observations which imply that at least two active neutrinos are massive and they mix with each other. The flavour mixing given by the Pontecorvo–Maki–Nakagawa–Sakata (PMNS) matrix. The gauge-invariant Dirac mass is not possible within the SM framework in the absence of right-handed neutrino ν_R. There are several models which can generate the neutrino mass as an extension to the SM. The simplest extension can be done by considering a lepton number violating effective dimension five operator $\frac{1}{\Lambda_M}\bar{L}\phi\phi L^c$, which gives a Majorana mass to neutrino after the electro-weak symmetry breaking. Here, Λ_M is the scale of the new theory. There are different ways to generate light neutrino mass, for example in Type I seesaw mechanism one needs to add a gauge singlet right-handed neutrino. In Type II seesaw mechanism neutrino mass can be generated using a scalar triplet while in Type III seesaw the same has been done by using fermion triplets. In the other variant of the seesaw mechanism, neutrino mass can be generated by small lepton-number-violating parameters which is called the inverse seesaw mechanism. In this case, the right-handed neutrinos are pseudo-Dirac type and have large enough Dirac Yukawa coupling to produce at the LHC. We study this scenario in chapter 3, where we probe the difficult region of the model at the LHC utilizing the jet substructure techniques.

1.2.2 Dark Matter

Several astrophysical observations in the past few decades have dictated that there is more matter in the universe than the luminous baryonic matter. This matter is called the Dark Matter (DM). The first such observation was made by the Dutch astronomer Jan Oort in 1932. He calculated the velocities of the stars from Doppler Shift and observed stellar motions in the galactic neighbourhood. It was found that the galaxies should have three times more mass to prevent the star from escaping. The very important next observation comes from the galactic rotation curve made by the Vera Rubin with her collaborators. The galactic rotation cure is almost flat for spiral galaxies in contradiction to Newton's law of gravity where rotation velocity should decrease as the distance increase from the centre of the galaxy. Later from the measurement of the gravitation lensing of the bullet cluster, it was found that the significant amount of mass resides in non-luminous region. Which also indicates the presence of non-luminous massive matter. The Planck 2018 collaboration provides the constraint on the global dark matter *relic density* as,

$$\Omega_{\mathrm{DM}}h^2 = 0.1187 \pm 0.0017, \tag{1.22}$$

from Cosmic Microwave Background measurement, where the observed Hubble constant is $\mathcal{H}_0 = 100\, h\, km\, s^{-1}\, Mpc^{-1}$. The DM candidate should be electrically neutral, weakly interacting and massive. From the CMB structure, it is known that the DM can not be baryonic. Other than that the nature of the DM and its interaction with the SM particles are unknown. The SM of particle physics does not have a suitable candidate for the DM candidate and certainly, an extension of the SM is required to have answers within the framework of particle physics for these observations.

To determine the properties of DM and its role in the structural formation DM detection play an important role. Many experiments are searching for dark matter like Weakly Interacting Massive Particles (WIMP) using different detection techniques. DM detection techniques can be classified primarily into direct detection, indirect detection and collider searches. In the direct detection experiment, the energy deposited in a detector is measured due to the recoil of the nuclei resulting from the elastic scattering with the WIMP. LUX, the XENON experiment, The Particle and Astrophysical Xenon Detector (PandaX), COSINE, DAMA etc are some of the direct detection experiments. The principle of indirect detection is based on the detection of particles produced due to annihilation or decay of the dark matter, which may also include the gamma rays, positrons and neutrinos. In collider search for DM, one look for the decay to new BSM particles into DM along with some SM visible particle at the detector. The usual search channel for DM is through detecting mono-x, where x can be QCD jet, photon or heavy gauge boson, Higgs etc. along with the missing transverse energy at the LHC. In Chapter 4, we explore a simple extension of the SM, the inert doublet model, which can provide the suitable DM candidate along with satisfying all the theoretical as well as experimental constraints. In Chapter 5, we also study the compressed SUSY spectrum in GMSB scenario where the Gravitino can be a suitable candidate for the dark matter.

1.2.3 Additional Motivation to look for BSM

Apart from the aforementioned issued, there are several other indicators of physics beyond the SM. One of them is the *hierarchy problem.* In the SM the mass of the fermions, and gauge bosons are are protected by the chiral symmetry and the gauge symmetry respectively. Hence, any correction to these masses is proportional to the mass of the respective fermion or the gauge boson themselves. However, the mass of the Higgs is not protected by any symmetry and tree-level Higgs mass receives huge radiative correction which is proportional to the highest scale of the theory. Hence if SM is the valid theory till the Planck scale then the correction to the Higgs mass is proportional to the Planck mass ($M_{Pl} \sim 10^{19}$GeV). This is unnatural and requires tremendous fine tunning for an experimentally observed Higgs boson with mass around 125 GeV. Different theoretical model such as Supersymmetry (SUSY), Extradimention and little Higgs are proposed to solve the hierarchy problem. For example, in unbroken SUSY scenario, all the bosons have fermion counterparts and the quadratic divergences exactly cancel out since the fermion loops acquire a negative sign.

Another issue which requires physics beyond the SM is the matter anti-matter asymmetry. As the particle and anti-particle differ by only electric charge, these will always pair produce and annihilate one other. This process leaves only pure energy in the Universe. However, at present, the matter is predominantly more than anti-matter. This asymmetry is known as *baryonic asymmetry* and can be quantified by the asymmetry parameter η_B

$$\eta_B = \frac{n_B - n_{\bar{B}}}{n_\gamma}, \tag{1.23}$$

where n_B, $n_{\bar{B}}$ and n_γ are the number density of matter, anti-matter and photon respectively. Sakharov proposed [9] three conditions which are required to obey by the theory to explain the baryon asymmetry. These are Baryon number violation, C and CP violation and departure from the equilibrium. The allowed CP violation in the quark sector of the SM is not enough to get the required asymmetry parameter.

The SM also does not justify the values of free parameters in the theory. The SM in total has 18 free parameters taking into account the quark masses, lepton masses, value of gauge coupling constants, quark mixing angles, the CP phase in the CKM matrix, the QCD θ term and the Higgs mass. Also, the flavour mixing of quark can not be explained with the SM.

In the SM there is no justification for the pattern of groups and representations, which is arbitrary and complicated. Also, it fails to unify all the four fundamental forces of nature including *Gravity*. All these issues indicate for physics beyond the SM and and the underlying motivation of the LHC program at CERN is to look for the BSM physics. Now we will briefly describe the LHC experiment and some aspects of its detectors useful to describe the phenological study in following chapters.

1.3 The Large Hadron Collider

The Large Hadron Collider (LHC) is the highest elevated energy human-made accelerator ever built which is located at CERN, Geneva [10]. It is a proton-proton collider with a tunnel circumference 27 Km which is situated 100 meters beneath the France-Switzerland border. LHC completed its Run I (2009 – 2013), after collecting 5 fb^{-1} and 25 fb^{-1} data with the centre mass of energy 7 and 8 TeV respectively. Recently It completed Run II (2015-2018) by gathering $150 fb^{-1}$ total dataset while running at 13 TeV. As LHC continues to probe the exiting physics the next run is planned to start in 2021. Finally with high-luminosity (HL-LHC) upgrade, 14 TeV run is projected to acquire data for an integrated luminosity as large as 3000 fb^{-1} in next two decades. The ATLAS [11] and the CMS [12] are two dedicate detectors to study the hadron collider physics at LHC. Apart from a proton-proton collision, LHC is also used to study the heavy-ion collisions to understand the structure of the quark-gluon plasma. ALICE [13] detector is used to study the heavy-ion collisions. LHCb [14] is dedicated to study the heavy flavour physics with b and c quark system for precision measurements.

1.3.1 Important components of a detector

It will be useful to note down some brief experimental aspect of LHC, as, in this thesis, we will be interested to explore new physics signature involving leptons, jets and missing transverse energy. ATLAS and CMS are two multi-purpose detectors at the LHC for hadron-hadron collisions. Both of these detectors work on a similar principle with changes in their design. An illustrative picture of the ATLAS detector is shown in Fig. 1.2. These are highly complex cylindrical multi-layers detectors. We will discuss the main component of the detector briefly.

1. **Tracker** is the innermost layer of the detector to determine the trajectories of the charged particles. The tracker determines the electromagnetic energy loss of the track. A very high magnetic field is used (4 Tesla for CMS and 2 Tesla for ATLAS) to obtain the momenta of the charged particles. The curvature of the trajectory can be calculated by $\frac{QB}{p}$, where B is the external magnetic field, Q is the electric charge of the particle and p is the particle's momentum. The pseudorapidity coverage of tracker is $|\eta| < 2.4$.

2. **Electromagnetic Calorimeter** is designed to measure the energy of photon and electron with high accuracy. Photon can be discriminated form charge particle in ECAL if the corresponding track is missing in the inner tracker. The resolution of ECAL central region is (0.025 X 0.025) approximately in $\eta - \phi$ plane. The ECAL pseudorapidity coverage is $|\eta| < 3$.

3. **Hadronic Calorimeter** measures the energy deposited by the hadrons. The HCAL resolution is low compared to ECAL, in the central region, it is (0.1 X 0.1) approximately in $\eta - \phi$ plane. The HCAL pseudorapidity coverage is $|\eta| < 5$ where the Hadronic Forward (HF) detector is placed for the higher pseudorapidity range $3 < |\eta| < 5$.

4. **Muon Chamber** is the outermost layer of the detector as high energy muons have a longer lifetime and also interacts weakly with the detector material. Muons leave the track in the inner tracer and then may undergo small energy loss in the calorimeter before reaching the outer tracker.

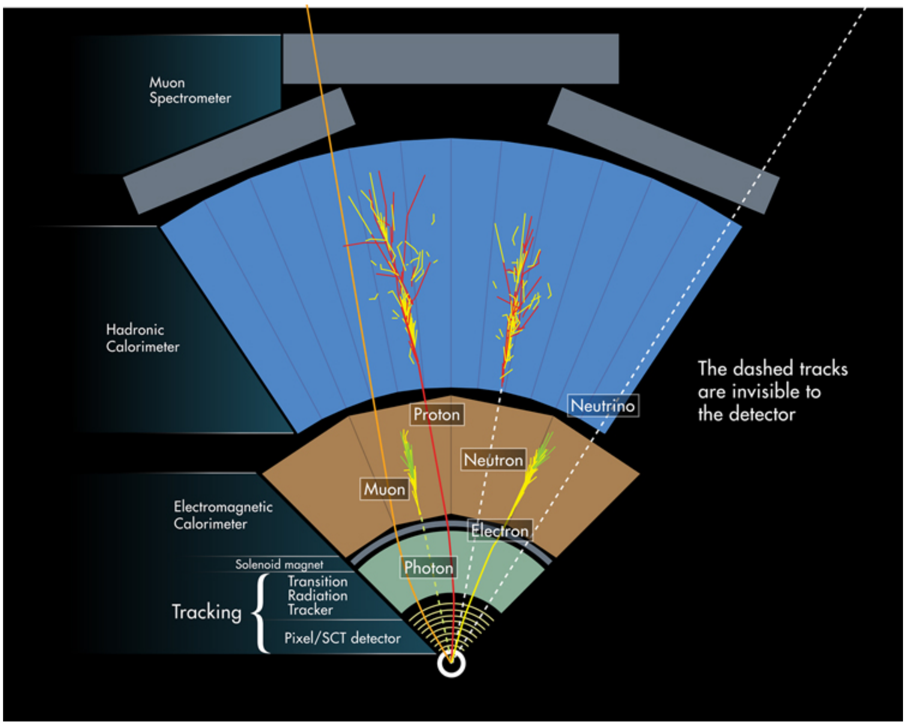

Figure 1.2: Schematic depiction of ATLAS detector. The interaction of the different particle with the different component of the detector is illustrated.Taken from [15].

1.3.2 Signature of Particles at LHC

Apart from e, μ, γ the other interesting signature of particle can be seen at the LHC as,

- Jet: As the quark and gluon can not be seen directly due to QCD confinement, we measure a spay of collimated hadrons called a jet. Jet can be originated either from the hadronic decay of heavy particle ($W/Z/h/t$) or from the fragmentation of single quark or gluon. The total energy of ECAL and HCAL plan ($\eta - \phi$ plane) can be taken as input to make jets. As in this thesis, we mostly deal with hadronic final state more detail on this is given in Chapter 2.

- Displaced vertex: Charge particles with lifetime $\tau \sim 10^{12}$ may travel some distance before decaying to charge particle. If the decay happens before the inner tracker ends then this signature can be seen as displaced vertex at the detector.

- Long-Lived Particle(LLP): If the lifetime of a charged particle is enough to reach the muon spectrometer then it gives rise to a new signature of LLP at the LHC. If the new particle is heavy then $\beta = \frac{v}{c}$ can play a crucial role to distinguish LLP from the muon.

- Missing transverse energy: Particles which do not have strong or electromagnetic interaction can leave the detector without leaving any trace at any of the components like neutrinos. Similarly, any of the proposed dark matter candidates in WIPM paradigm, such as a lightest supersymmetric particle in R-parity conserving SUSY would also remain undetected. The amount of missing transverse momenta in an event can be calculated by the imbalance of the visible momenta in transverse plain with respect to the beam direction,
$$\vec{\not{P}}_T = -\sum \vec{P}_T(visible). \tag{1.24}$$

1.3.3 Important kinematic variables used at a hadron collider

In LHC coordinate system, the momentum component of a particle can be described by $(p_T, y, \phi\ )$, where p_T is the transverse momentum of the particle given by $p_T = p\sin\theta$. Here θ being the polar angle and ϕ is the azimuthal angle about the z axis. The rapidity (y) of a particle is given by

$$y = \frac{1}{2} ln\frac{E + P_z}{E - P_z}. \tag{1.25}$$

The rapidity of a particle in a boosted frame with respect to the lab frame is given by

$$y' = y - y_0, \tag{1.26}$$

where, $y_0 = \frac{1}{2} ln\dfrac{1+\beta_0}{1-\beta_0}$ and β_0 is the relative velocity of the particle. Hence rapidity difference $\Delta y = y_2 - y_1 = y_2' - y_1'$ is invariant under longitudinal boost.

In the limit, $P_T \gg m$, and we get,

$$y \to \frac{1}{2} ln \frac{1+\cos\theta}{1-\cos\theta} \equiv \eta, \tag{1.27}$$

where, η is called the pseudo-rapidity. It has one-to-one correspondence with the polar angle θ for $-\infty < \eta < \infty$. To summarise, in the LHC co-ordinate system a particle's four-momentum can be written in terms of (p_T, y, ϕ) with

$$P^\mu = (E_T \cosh y, P_T \cos\phi, P_T \sin\phi, E_T \sinh y), \tag{1.28}$$

where $E_T = \sqrt{P_T^2 + m^2}$.

Another important variable which is useful for defining the angular separation between two particles at the detector is measured via

$$\Delta R = \sqrt{(\Delta\eta)^2 + (\Delta\phi)^2} \tag{1.29}$$

We will be using these variables throughout our studies in this thesis. In this thesis, we will look into a few possible extensions of the SM to answer some of the issues with SM discussed in this chapter. This thesis gives new and detailed study to search for BSM at the LHC in the coming years. The methodology and analysis technique described in the thesis can be applied to other BSM models also due to its general nature.

1.4 Organization of the Thesis

The thesis will be organised in the following way:

- Chapter 1 provides a short description of the SM and its shortcomings. We also discuss why it is important to look for beyond the SM scenarios.

- Chapter 2 contains the methodology used to address different collider search. A brief review of jet algorithms and jet substructure is given. We also discuss the boosted decision tree algorithm used in different analysis.

- Chapter 3: Here we discuss the inverse seesaw model where the small neutrino mass can be generated from a naturally small lepton number violating parameter. We have proposed a new final state (opposite sign lepton associated with at fat jet) to restrict the parameter space of the model at the HL-LHC.

- Chapter 4: We discuss the Inert doublet model which is the simplest extension of the SM to accumulate a DM candidate. We explore the hierarchical mass spectrum of the Inert Doublet Model where relatively light dark matter along with much heavier scalar states can fully satisfy the constraints on the relic abundance and also fulfill other theoretical as well as collider and astrophysical bounds.

- Chapter 5: A study is performed to search for the compressed spectra of SUSY in the range of 2-3 TeV. We also design new kinematic observables to distinguish the compressed and uncompressed spectra.

- Chapter 6: We look for CP-violating effects in the Higgs sector as an alternative to searching for BSM physics at the LHC. We study the decay mode $H \to \tau^+\tau^-$, where $\tau^\pm$ further decays hadronic. Several CP odd observables are proposed which are sensitive to the CP-violating phase. We additionally present a novel method to reconstruct τ momentum at the LHC.

- Chapter 7 concludes with a summary of this thesis and the future prospect of the work done.

Chapter 2

Methodology

The key task to search for physics beyond the SM is to look for the previously unexplored parameter space at the LHC. In many BSM scenarios, new heavy particles mostly decay into SM gauge bosons like $W/Z/H$ or the top quarks. Hence, it becomes important to search for these models in a variety of kinematic configurations. Unfortunately, hadronic final states remain remarkably difficult to probe because of overwhelming QCD background along with associated underlying events, pile-up or multi-parton interaction at the LHC, which is a hadronic collider. Therefore we investigate the internal structure of jets to uncover this window and utilise the jet-substructure observables to thoroughly scrutinise the TeV scale BSM theories at the LHC. Moreover, we utilise the multivariate analysis technique to optimise the collider search.

In this chapter, we briefly discuss the jet algorithms and jet substructure for the boosted topology which we have used in this thesis to constraints different BSM scenarios. We also describe briefly about collider analysis using the multivariate technique.

2.1 Jets and Jets algorithms

In high energy collision, quark and gluons (partons) can not be directly observed in their own. Rather we see the outcome of the fragmentation and hadronisation of high energy partons as a collimated spray of hadrons, called a *jet*. This happens

due to the confinement principle of QCD. A well-defined set of the rules are then required to combine these hadrons into a jet. These set of rules are known as jet-algorithms. Sterman and Weinberg give the first set of rule in 1977 to define a jet for e^+e^- collider [16]. Later Jade collaboration developed the JADE algorithm [17, 18], The latter progressively created variant of JADE algorithm is now known as k_T algorithm [19].
There are some basic requirements that a jet algorithm should satisfy. A jet algorithm should be easy to implement experimentally as well as theoretically. Also, It should be defined at all order of perturbation theory and have a finite cross-section. The cross-section should not be much affected due to hadronization.

Jet algorithms can be broadly classified into two categories, cone algorithms and sequential algorithms.

- **Cone jet alorithms** are based on the idea of the flow of energy in an event. In these algorithms, one adds the 4-momentum of the particles in a cone for a given cone centre (y_j, ϕ_j) and radius parameter(R). These cones are called stable cone if the added momentum of the particles points towards the direction of the centre of the cone. The stable cones suffer from overlapping by other cones and can only be called a jet after running a split merger procedure, in which mostly overlapping stable cones are either merge or split according to their overlapping fraction. JetClu, MidPoint, ATLAS cone, CMS cone, Sis cone are some examples of cone algorithm.

- **Sequential jet algorithms** are motivated from the idea of successive parton branchings from perturbative QCD. All the sequential jet algorithm are collinear-infrared safe, which implies that the addition of a new soft or collinear particle does not affect the jet. These algorithms start with a list of particle and then recombine them sequentially one by one. Some of the examples of sequential jet algorithms are JADE, k_T, Anti-k_T and Cambridge-Achen jet algorithm.

We will now discuss the sequential jet algorithms.

2.1.1 The generalised k_T family

The generalised form of sequential algorithm is developed for the hadron colliders. These algorithms use dimensionful distance measure which is formulated in terms of variables that are invariant under longitudinal boosts along the jet axis. The steps to make a jet from a list of particle or constituents are as follows:

1. For each pair of particles i, j one has to calculate the two distance parameters is given by,

$$d_{ij} = min(k_{Ti}^{2p}, k_{Tj}^{2p})\frac{R_{ij}^2}{R^2}, \qquad d_{iB} = k_{Ti}^{2p}, \tag{2.1}$$

   where $R_{ij}^2 = (y_i - y_j)^2 + (\phi_i - \phi_j)^2$ is the angular separation between two constituents. At small angle, $R_{ij}^2 \propto \theta_{ij}^2$ and R plays a role of a cone radius parameter.

2. Now, find the minimum d_{min} of all the d_{ij} and d_{iB}. If d_{min} is a d_{ij} then merge particles i and j into a single particle.

3. If it is a d_{iB} then ith particle is declared to be a final jet and then we remove it from the list.

4. Again, we have to repeat the procedure from step 1 until no particles are left in the list.

- k_T **algorithm**: The formulation of k_T algorithm is motivated by the fact that softer radiations are important in perturbative QCD [20]. Hence, using $p = +1$ in Eq. 2.1, the algorithm begins clustering the softer particle first. This algorithm is extensively sensitive to extra radiation coming from Underlying Events or pile-up.

- $Anti - k_T$ **algorithm**: Here we use $p = -1$ in Eq. 2.1. Consequently, this algorithm starts with combining the hardest particle first which mimics the idea Parton shower [21]. In this way, $Anti - k_T$ jets are not much affected by softer radiation and are mostly circular in $y - \phi$ plane. This algorithm is most used by the LHC experimentalists.

- **Cambridge-Aachen algorithm (CA)**: If we set $p = 0$ in Eq. 2.1, then the algorithm depends only on the geometric parameter with $d_{ij} = \frac{R_{ij}^2}{R^2}, d_{iB} = 1$ and jet does not suffer from softer radiation like in the case of k_T algorithm [22]. For more details on this topic see review arcticle in Ref. [23].

2.2 Boosted jet topology

As we probe higher energy, the events at the LHC are significantly occupied with the heavy boosted particles. Boosted regime implies when the heavy particles (like $H/Z/W^{\pm}/t$) have sufficient boost such that their hadronic decay products are collimated and can be combined in a single large-radius (R) jet or typically characterised as fat jet. Study of these hadronic final state becomes difficult as the QCD jet can acquire a large mass due to non-perturbative effect at such large transverse momentum P_T and large R. It then becomes a strenuous task to distinguish the heavy particle from huge QCD jet background at the LHC. The main key to distinguish the signal type $(H/Z/W^{\pm}/t)$ jets from the background type (QCD) jet emerges from the idea of different radiation pattern inside these two kinds jets. The QCD branchings have asymmetric sharing of energy while the signal jet has the symmetric sharing of energy due to its decay topology. This concept laid the foundation of the *jet substructure* techniques. Many jet substructure observables are motivated by this idea. Using these observables ones can look for the substructure of boosted $H/Z/W^{\pm}/t$ jets and distinguish from the QCD jets. These fat jets can have two-prong or three-prong substructures depending on the parent particle while QCD jets would typically show one prong structure.

Now we will discuss few fat jet properties which are very important for phenomenological applications at the LHC.

2.3 Jet Mass and Groomers

Here, we start with a discussion of an important variable, called the jet invariant mass.

2.3.1 Jet Mass

At high energy single quark/gluon mass appear from the parton shower. If we calculate the jet mass for a quark emitting a gluon from the viewpoint of perturbative QCD that jet properties dominate by its first emission. Then it can be approximately calculated as

$$\langle m^2 \rangle \approx \frac{\alpha_s}{\pi}\frac{3}{8}C_F P_T^2 R^2 \tag{2.2}$$

which increases which increasing radius parameter R. Hence for a high P_T and large-radius QCD jet can have a long tail in jet mass distribution (for review see Ref. [24]). For the detector level simulations the jet mass can be calculated as $M_J = (\sum_{i\in J} P_i)^2$ where P_i are the four-vector of energy hits in the calorimeter. The distributions of jet mass is shown in Fig. 2.1.The peak in QCD distribution around 20 GeV can be roughly estimated by Eq. 2.2. For the sample of $W^\pm$ distribution, it peaks around the mass of the $W^\pm$ boson. A small peak around 20 GeV occurs when one of the quark fall outside the jet radius for W mass distribution.

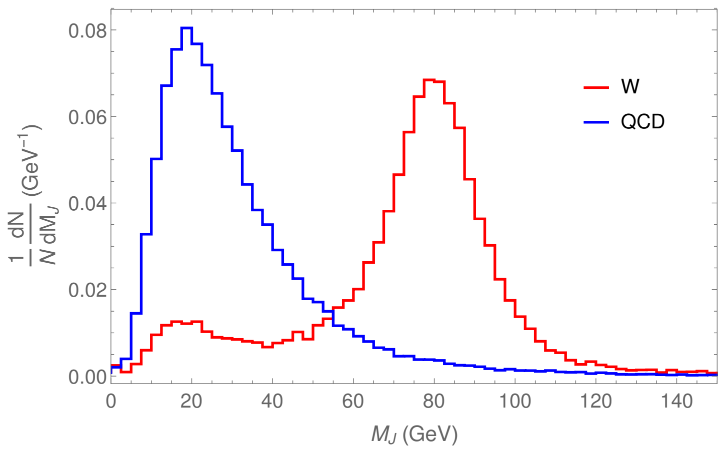

Figure 2.1: Normalised distribution of jet mass for $W^\pm$ (red) and QCD (blue) jet.

The discrimination power of M_J reduces if extra contribution comes from the parton which does not originate from the decay. This results in broadening of the peak in the M_J distributions. To remove these softer and wide-angle radiations, different jet grooming techniques are proposed such as - trimming, pruning and filtering [25–28]. We now discuss these methods.

2.3.2 Grooming techniques

Study of the large-radius jet at the LHC becomes difficult in the presence of energy deposited inside the fat jet due to underlying event, pile-up or multi-parton interaction. These softer radiations reduce the efficiency of jet observable. Many grooming techniques have been developed to clean the wide-angle and soft radiation which are essential not part of the fragmentation of the decay product of heavy particle. We discuss some of the grooming techniques below.

1. Trimming: In this procedure [25] of grooming, we start by reclustering the constituents of the fat jet into subjet of radius $R_{sub} < R$ where R is the radius of the fat jet. The usual choice to recluster the subjet is k_T or Cambridge/Achen jet algorithm. Now, the subjet will be kept as a part of fat jet if $P_t^{sub} > z_{cut} P_t^{fatjet}$. Here z_{cut} is the parameter of the algorithm. If the condition is not satisfied then the subjet is discarded.

2. Pruning: At each step of recombination, one calculates the two variable z and ΔR_{ij}, where momentum fraction z is defined as $z = min(P_{Ti}, P_{Tj})/P_{T_{i+j}}$ and ΔR_{ij} is the angular separation between two proto-jets. If $z < z_{cut}$ and $\Delta R_{ij} > R_{fact}$ then i-th and j-th proto-jets are not recombined and the softer one is discarded. Here, z_{cut} and R_{fact} are parameters of pruning algorithm. We have taken the default values of $R_{fact} = 0.5$ and $z_{cut} = 0.1$ as suggested in Ref. [26, 27].

3. Filtering: Filtering was first proposed with the technique of mass drop tagger in Ref. [28] to remove the underlying events. In filtering, the constituents of the fatjet are reclustered into subjets of smaller radius parameter i.e. $R_{filt} < R$. Then the hardest n subjets are chosen and other subjets are discarded. The choice to keep the third subjet is motivated to keep the hard gluon emission from the quark.

2.3.3 Jet Shape Observable/ Prong finder

To study the different radiation pattern inside a jet, functions involving the constituents of a jet are designed. These functions are known as *Jet shape observable*. N-subjettiness ratio and Energy Correlation Functions are two of the very first jet shape variables proposed in the literature. We will briefly describe these observable in this section.

N-subjettiness ratio:

N-*subjettiness* is a jet shape variable which determines the inclusive jet shape by assuming N subjets in it. The idea of N-subjettiness is motivated form the variable N-*jettiness*. It is defined as the angular separation of the constituents of a fat jet with the nearest subjet axis weighted by the P_T of the constituents. This can be calculated as [29, 30] ,

$$\tau_N^{(\beta)} = \frac{1}{\mathcal{N}_0} \sum_i p_{i,T} \min \left\{ \Delta R^{\beta}_{i\alpha_1}, \Delta R^{\beta}_{i\alpha_2}, \cdots, \Delta R^{\beta}_{i\alpha_N} \right\}. \tag{2.3}$$

Here, i runs over the constituent particles inside the jet and $p_{i,T}$ is the respective transverse momentum. The normalization factor is defined as $\mathcal{N}_0 = \sum_i p_{i,T} R$ for a jet of radius R. A jet with N subjets in it have larger value for $\tau_{<N}$ than $\tau_{\geq N}$, Hence the ration $\dfrac{\tau_N}{\tau_{N-1}}$ perform better as a discriminatnt. We show normalised distribution of N-subjettiness ratio for $W^{\pm}$ and QCD jet in Fig. 2.2, where distribution for $W^{\pm}$ peaks close to zero while for QCD it peaks for higher value of τ_{21}. All the jet observables distribution shown in this chapter are for a fat jet clustered using Cambridge-Achen (CA) [22] algorithm with radius parameter $R = 0.8$ and P_T greater than 200 GeV. Fatjets are reconstructed using the `FastJet` [31].

There are many methods to choose the axes choice like k_T axes, WTA k_T axes, generalised- k_T axes, minimal axes, one-pass minimizations axes.

Energy Correlation Functions (ECF):

As the field of jet substructure gain importance in searching new physics, several new observable are proposed in the past few years. In this view, a series of N -point energy correlation functions are developed to classify jets with n hard prongs. In

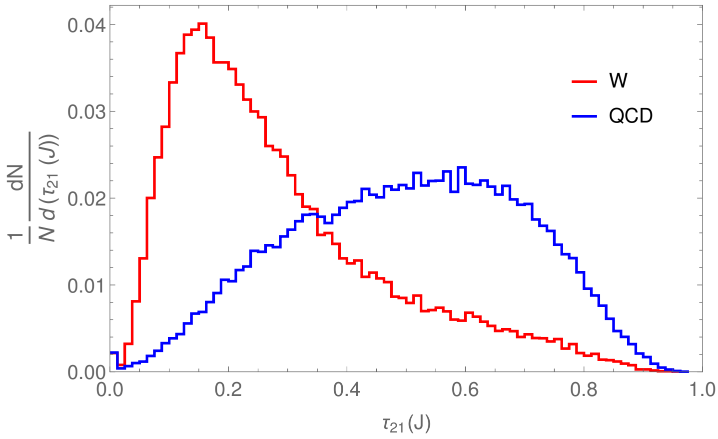

Figure 2.2: Normalised distribution of N-subjettiness ratio for $W^{\pm}$ (red) and QCD (blue) jet.

our study, we use 2-prong discriminant energy correlation functions [32]

$$C_2^{(\beta)} = \frac{e_3^{(\beta)}}{(e_2^{(\beta)})^2} \tag{2.4}$$

where, $e_2^{(\beta)} = \sum_{1\le i<j\le n_J} z_i z_j \theta_{ij}^{\beta}$ and $e_3^{(\beta)} = \sum_{1\le i<j<k\le n_J} z_i z_j z_k \theta_{ij}^{\beta}\theta_{ik}^{\beta}\theta_{jk}^{\beta}$ are 2-point and 3-point energy correlation functions respectively. The β represents the exponent. Here z is the energy fraction or transverse momentum taken by i^{th} particle, and θ is angular variable between i^{th} and j^{th} particle. The distributions of C_2 is shown in Fig. 2.3.

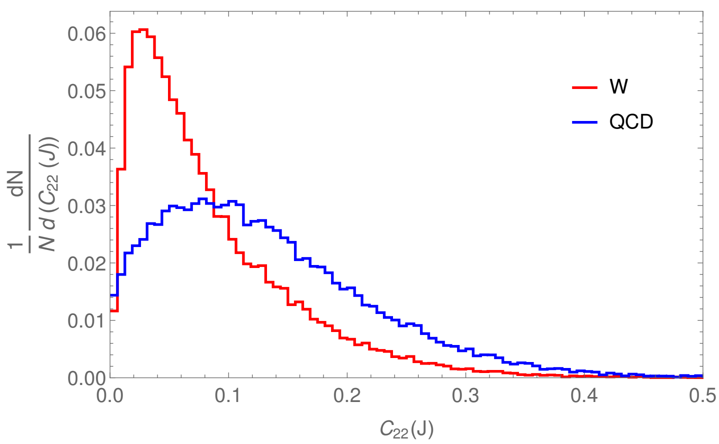

Figure 2.3: Normalised distribution of ECF C_2^2 for $W^{\pm}$ (red) and QCD (blue) jet.

The main advantage of ECF over N-subjettiness is that it does not require minimization procedure over the all possible subjet axes. In other variants of ECF to find $n-$ prong structure like N_i series and M_i series are available in litrature (see more in Ref [33]). Whereas U_i series are used for quark/gluon discrimination.

We shall use all the above definitions throughout our studies in this thesis (for more details see recently published book on the above topics in Ref. [34]). In the next section we will discuss the collider analyis using the boosted decision tree.

2.4 Multivariate Analysis (MVA)

We adopt the boosted decision tree [35] methods to optimise the collider analysis. We will briefly describe its algorithm here. A decision tree can be seen as a binary tree-structured classifier. After selecting the highest important variables, the tree is then divided into branches with the decisions of left/right (yes/no). This step is repeated until a stop criterion is fulfilled. In this way, the phase space is divided into many region (leaf) that can be labelled as either 'signal-like' leaf or 'background-like' leaf. The decision tree (or multivariate) analysis outperforms the cut-based analysis since a cut-based analysis can select only one hypercube as the signal region of phase space, whereas, the decision tree can split the phase space into a large number of hypercubes. Hence, in this approach, a non-linear boundary is created in hyperspaces to segregate the signal and background.

Now we define the parameters used in the algorithms. Suppose each event is weighted with a weight of w_i. Now the criterion for splitting the branch can be defined by its purity, which is given by,

$$P = \frac{\sum_S w_S}{\sum_S w_S + \sum_S w_B}, \tag{2.5}$$

where $\sum_S$ represents the sum over the signal events whereas $\sum_B$ represents the sum over background events in a particular branch. For a pure signal or background $P(1-P) = 0$. Hence we can choose the splitting criteria of a branch by minimizing the following,

$$Gini = (\sum_{i=1}^{n} w_i)(1 - P) \tag{2.6}$$

where n is the number of events at the branch. We stop the splitting of the branch by setting a parameter `MinNodeSize`. Here `MinNodeSize` means the minimum percentage of training events required in a leaf node, which is set in algorithm while training the sample.

2.4.1 Boosted decision tree

Now to improve further the decision tree algorithm the following method of boosting is used. We start with previously define unweighted events and make the decision tree. If some events are misclassified (signal event falls on background leaf) then we increase the weight of the event (boosting). Many trees are build in this way with different weights which form a forest. Boosting helps to stabilise the response of the decision tree against the fluctuation in the training sample. It also enhances the performance compare to a single decision tree. AdaBoost and ϵ- Boost are some famous boosting techniques.

Now we will discuss how to use in this algorithm in collider analysis. First, we calculate the linear correlations among the variables and then the importance of each variable.

Linear corelation of variables

We calculate the linear correlation ρ between two variable X and Y using the following equation

$$\rho(X, Y) = \frac{E(XY) - E(X)E(Y)}{\sigma(X)\sigma(Y)}, \tag{2.7}$$

where $E(X), E(Y)$, and $E(XY)$ are the expectation value of the variable X, Y, and XY respectively. Here, $\sigma(X)$ $\sigma(Y)$ represents the standard deviation of variable X and Y respectively. Linear correlation among the variables plays a crucial rule to determine the information carried by the variable is unique or not. Most of the variables used in this study should be highly uncorrelated with each other. Here positive and negative signs of the coefficients signify correlation and anti-correlation with the other variables. Linear correlation among the variables which are discussed in this chapter is shown in Fig. 2.4.

Importance of variables

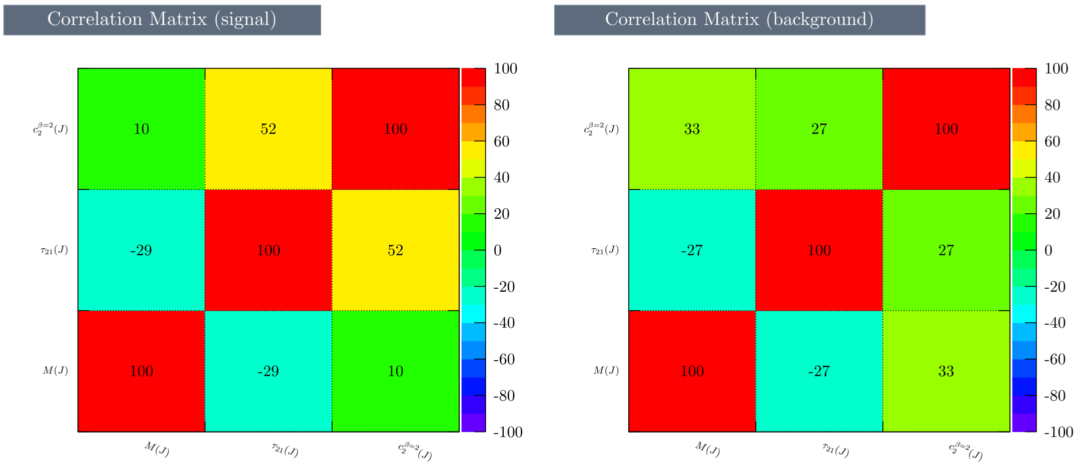

Figure 2.4: The linear correlations coefficients (in %) for (a) signal and (b) background among different kinematical variables discussed in this chapter.

We further calculate the method unspecific ranking (relative importance) for each observable according to their separation in Fig. 2.5. The separation in terms of an observable λ is defined as [36]

$$\Delta_{(\lambda)} = \int \frac{(\hat{y}_s(\lambda) - \hat{y}_b(\lambda))^2}{\hat{y}_s(\lambda) + \hat{y}_b(\lambda)} d\lambda \tag{2.8}$$

where $\hat{y}_s$ and $\hat{y}_b$ are the probability distribution functions for signal and background for a given observable λ respectively. The limits of integration correspond to the allowed range of λ. Here $\Delta_{(\lambda)}$ quantify discrimination performance of the observable λ. The separation $\Delta_{(\lambda)}$ ranges from 0 to 1. If $\Delta_{(\lambda)} = 0(0\%)$ implies $\hat{y}_s(\lambda) = \hat{y}_s(\lambda)$, which means zero discrimination power of observable λ and $\Delta_{(\lambda)} = 1(100\%)$ corresponds to perfect discrimination power for a complete overlapping and non-overlapping probability distribution functions respectively. Importance of the variables discussed in this chapter is shown in Fig. 2.5.

After calculating the importance of variables, we divide the data set in two equal parts. One part of the data sample is used to train the BDT algorithm and the other part is used for the validation. The parameters used in the BDT

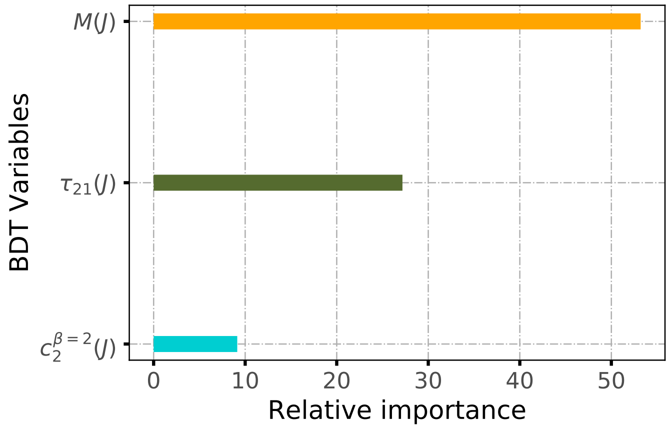

Figure 2.5: Relative importance of the kinematic variables which will be used in the BDT algorithm.

algorithm are shown in Tab. 2.1 below: Note the value of the parameter shown in

NTrees	400	Number of trees in the forest
MaxDepth	2	Max depth of the decision tree allowed
MinNodeSize	5.6%	Minimum percentage of training events required in a leaf node
BoostType	AdaBoost	Boosting type for the trees in the forest
AdaBoostBeta	0.5	Learning rate for AdaBoost algorithm
nCuts	20	Number of grid points in variable range used in finding optimal cut in node splitting

Table 2.1: Configuration options reference for BDT architecture. These hyperparameters shall be tune according to the data properties.

the table is for example. These hyperparameters have to be optimised with the training. After the training is done, we calculate the Kolmogorov-Smirnov (KS) probability for training and testing sample to test that the network is not overtrained. KS probability quantifies a distance between the cumulative distribution function of the training and validation dataset. If the testing data fit well to the training data and the validation then the network is not overtrained. After the training is done, we apply the cut on BDT response and obtain the corresponding number of signal $\mathcal{N}_S$ and background $\mathcal{N}_B$. Finally we calculate the statistical significance to estimate the corresponding exclusion limits and discovery potential constraining the new physics model parameter space. We perform the collider study using a multivariate analysis (MVA) employing the Boosted Decision Tree

(BDT) algorithm in Chapter 4 and Chapter 5 and provide a comparison with the traditional cut base analysis.

Chapter 3

Probing Inverse Seesaw Model

To satisfy the neutrino oscillation data, a simple extension of the SM in the form of the seesaw mechanism suffices to a large extent [37–43]. In these frameworks, SM-singlet heavy Majorana Right handed Neutrinos (RHNs) are introduced, which through a dimension five operator [44] subsequently lead to tiny Majorana neutrino masses. There is another version of the seesaw mechanism [45–49] wherein the small neutrino mass can be obtained from a naturally small [50] lepton number violating parameter, rather than being suppressed by a heavy RHN mass. This is known as inverse seesaw model, in this case, the RHN is of a pseudo-Dirac type, and their Dirac Yukawa coupling can be large enough to produce RHNs at the LHC. We study [51] dilepton associated with a fat jet ($l^{\pm}l^{\mp}J$) final state at the LHC which is the unique signature of pseudo-Dirac type RHNs. This study provides the most stringent bound on the mixing parameter and the mass of RHNs.

This chapter is organised in the following way – in Sec. 3.1 we discuss the prototypical model of interest for the searches at the LHC. In Sec. 3.2 we then proceed to our analysis, present details of our simulation, benchmark points and the final results. Finally, in Sec. 3.3 we summarise our results and conclude.

3.1 Inverse Seesaw scenario

In the inverse seesaw [45, 46] the small neutrino mass is obtained by tiny lepton-number-violating parameters, rather than the suppression by the heavy neutrino mass scale as in the ordinary seesaw mechanism. In the inverse seesaw scenario, the heavy neutrinos are pseudo-Dirac particles and their Dirac Yukawa couplings with the SM lepton doublets and the Higgs doublet can be even order one, while reproducing the small neutrino masses. Thus, the heavy neutrinos in the inverse seesaw scenario can be produced at the high energy colliders through the sizable mixing with the SM neutrinos.

Since any number of singlets can be added to a gauge theory without introducing anomalies, one could exploit this freedom to find a natural alternative low-scale realization of the seesaw mechanism. In the low scale seesaw (studied in [52]), the SM is extended by n_1 SM singlet RHNs N_R and n_2 sterile neutrinos S. For simplicity we consider a basis where the charged leptons are identified with their mass eigenstates. Hence before the electroweak symmetry breaking (EWSB) we write the general interaction Lagrangian as

$$\begin{aligned} -\mathcal{L}_{int} &= Y_1\overline{\ell_L}HN_R + Y_2\overline{\ell_L}HS + M_N\overline{N_R^c}S + \frac{1}{2}\mu\overline{S^c}S + \\ &+ \frac{1}{2}M_R\overline{N_R^c}N_R + h.c. \end{aligned} \tag{3.1}$$

where ℓ_L and H are the SM lepton and Higgs doublets, respectively. Y_1 and Y_2 are the Yukawa coupling matrices of dimensions $3 \times n_1$ and $3 \times n_2$ respectively. M_R and μ are Majorana mass matrices for N_R and S of dimensions $n_1 \times n_1$ and $n_2 \times n_2$, respectively. Due to the presence of μ and M_R mass parameters the lepton number is broken. After the EWSB breaking, from Eq. 3.1 we get,

$$\begin{aligned} -\mathcal{L}_{mass} &= M_D\overline{\nu_L}N_R + M\overline{\nu_L}S + M_N\overline{N_R^c}S + \frac{1}{2}\mu\overline{S^c}S \\ &+ \frac{1}{2}M_R\overline{N_R^c}N_R + h.c. \end{aligned} \tag{3.2}$$

where $M_D = Y_1\frac{v}{\sqrt{2}}$, $M = Y_2\frac{v}{\sqrt{2}}$ and $\langle H\rangle = \frac{v}{\sqrt{2}}$. Hence the neutral fermion mass matrix can be written as

$$-\mathcal{L}_{mass} = \frac{1}{2}\begin{pmatrix}\overline{\nu_L} & \overline{N_R^c} & \overline{S^c}\end{pmatrix}\begin{pmatrix}0 & M_D & M \\ M_D^T & M_R & M_N \\ M^T & M_N^T & \mu\end{pmatrix}\begin{pmatrix}\nu_L^c \\ N_R \\ S\end{pmatrix}. \tag{3.3}$$

From Eq. 3.3 we can get a variety of the seesaw scenarios by setting respective terms to be zero*. The simplest scenario is the inverse seesaw model which has been studied in [53, 54] by fitting the neutrino oscillation data considering M and M_R to be zero. The sub-matrices M_N and μ do not arrive from the $SU(2)_L$ symmetry breaking and μ is the lepton number violating mass term. Hence they follow the hierarchy $M_N \gg M_D \gg \mu$. The value of μ can be small by 't Hooft's naturalness criteria [50] since the expected degree of lepton number violation becomes naturally small. In this work we consider a minimal scenario where two generations of the RHNs are involved which can satisfy the neutrino oscillation data. The effective light neutrino mass matrix can be written under the seesaw approximation as

$$M_\nu \sim M_D\,(M_N^T)^{-1}\,\mu\,M_N^{-1}\,M_D^T, \tag{3.4}$$

whereas in the heavy sector we will have the three pairs of degenerate pseudo-Dirac neutrinos of masses of order $M_N \mp \mu$. The smallness of M_ν^{light} is naturally obtained from both of the smallness of μ and $\frac{M_D}{M_N}$. Hence $M_\nu^{\text{light}} \sim \mathcal{O}(0.1)$ eV can be obtained from $\frac{M_D}{M_N} \sim 0.01$ and $\mu \sim \mathcal{O}(100)$ eV. Thus the seesaw scale can be lowered considering $Y_1 \sim \mathcal{O}(0.1)$ which implies $M_D \sim 10$ GeV and $M_N \sim 1$ TeV. The inverse seesaw scenario has been discussed under the general parametrization in [55] using Casas-Ibarra conjecture for general Y_D.

In order to make our discussions simple we assume degenerate RHNs, with $M = M_N \times \mathbb{1}$. Here, $\mathbb{1}$ is the unit matrix as before and M_N is the RHN mass eigenvalue. With these assumptions, the neutrino mass matrix may be simplified

*Simply assigning the lepton numbers for the SM singlet RHNs N_R and S as $+1$ and -1, respectively a purely inverse seesaw scenario can be achieved where the (13), (22) and (31) elements of the Eq. 3.3 will not arise.

as

$$M_\nu = \frac{1}{M_N^2}\, M_D\, \mu\, M_D^T\,. \tag{3.5}$$

Consider a typical flavour structure of the model where M_D and M_N are proportional to the unit matrix such as $M_D \to M_D \times \mathbb{1}$ and $M_N \to M_N \times \mathbb{1}$ respectively. Thus, the flavour structure is now fully encoded in the 3×3 matrix μ. We refer to this scenario as Flavor Diagonal (FD). It has been shown that the FD case in the inverse seesaw mechanism can satisfy neutrino oscillation data [55]. Another flavour structure possible in the inverse seesaw scenario is where M_D carries flavour structure while $\mu \to \mu \times \mathbb{1}$ and $M \to M_N \times \mathbb{1}$. This is called the Flavor Non-Diagonal (FND) scenario. This has been studied for different signals in [55, 56], under general parametrization [57].

Assuming $M_D M_N^{-1} \ll 1$, we can express the flavour eigenstates (ν) of the light Majorana neutrinos in terms of the mass eigenstates of the light (ν_m) and heavy (N_m) Majorana neutrinos such as

$$\nu \simeq \mathcal{N}\nu_m + \mathcal{R}N_m. \tag{3.6}$$

Here,

$$\mathcal{R} = M_D M_N^{-1}, \;\; \mathcal{N} = \left(1 - \frac{1}{2}\epsilon\right) U_{\rm PMNS}, \quad \epsilon = \mathcal{R}^*\mathcal{R}^T, \tag{3.7}$$

and U_{PMNS} is the usual neutrino mixing matrix which diagonalise the mass matrix m_ν,

$$U_{PMNS}^T\, m_\nu\, U_{PMNS} = \mathrm{diag}(m_1, m_2, m_3). \tag{3.8}$$

In the presence of ϵ, the mixing matrix $\mathcal{N}$ is not unitary. The charged current (CC) and neutral current (NC) interactions may be expressed in terms of the mass eigenstates of the RHNs as

$$\mathcal{L}_{CC} \supset -\frac{g}{\sqrt{2}}\, W_\mu\, \bar{e}\, \gamma^\mu\, P_L\, \mathcal{R}\, N_m + \text{h.c.}\,, \tag{3.9}$$

where e denotes the three generations of charged leptons, and $P_L = \frac{1}{2}(1-\gamma_5)$ is the projection operator. Similarly, in terms of the mass eigenstates the neutral current interaction may be written as,

$$\mathcal{L}_{NC} \supset -\frac{g}{2C_w} Z_\mu \Big[\overline{N}_m \gamma^\mu P_L(\mathcal{R}^\dagger \mathcal{R}) N_m + \overline{\nu_m}\gamma^\mu P_L(\mathcal{N}^\dagger \mathcal{R}) N_m + \text{h.c.}\Big] \,, \tag{3.10}$$

where, $C_w = \cos\theta_w$ with θ_w being the weak mixing angle. We notice from Eqs. (3.9) and (3.10) that the production cross section of the RHN in association with a SM charged lepton (or SM light neutrino) is proportional to light-heavy mixing $|V_{\ell N}|^2$.

In our analysis, we will consider two degenerate pseudo-Dirac type RHNs separately being coupled to the SM charged leptons e and μ respectively. Hence in our analysis we consider $M_N = M_N \times \mathbb{1}_{2\times 2}$. In this model framework we will also separately study the case when a RHN is coupled with μ, which we name as the single flavour case. The two flavour case, without considering flavour detection efficiencies, will roughly double the number of signal events relative to the single flavour case.

The elements of the $\mathcal{N}$ and $\mathcal{R}$ matrices in the Eqs. 3.6- 3.8 can be constrained by the experimental results. To do this we adopt the current neutrino oscillation data: $\sin^2 2\theta_{13} = 0.092$ [58], along with the other oscillation data [59]: $\sin^2 2\theta_{12} = 0.87$, $\sin^2 2\theta_{23} = 1.0$, $\Delta m^2_{12} = m^2_2 - m^2_1 = 7.6\times 10^{-5}$ eV^2, $\Delta m^2_{23} = |m^2_3 - m^2_2| = 2.4\times 10^{-3}$ eV^2. The neutrino mixing matrix is given by

$$U_{\text{PMNS}} = \begin{pmatrix} C_{12}C_{13} & S_{12}C_{13} & S_{13}e^{i\delta} \\ -S_{12}C_{23} - C_{12}S_{23}S_{13}e^{i\delta} & C_{12}C_{23} - S_{12}S_{23}S_{13}e^{i\delta} & S_{23}C_{13} \\ S_{12}C_{23} - C_{12}C_{23}S_{13}e^{i\delta} & -C_{12}S_{23} - S_{12}C_{23}S_{13}e^{i\delta} & C_{23}C_{13} \end{pmatrix} \mathcal{P} \tag{3.11}$$

where $C_{ij} = \cos\theta_{ij}$, $S_{ij} = \sin\theta_{ij}$ and the Majorana phase matrix as $\mathcal{P} = \text{diag}(1, e^{i\rho}, 1)$. We consider the Dirac CP-phase (δ) and the Majorana phase (ρ) as free parameters.

The elements of the mixing matrix $\mathcal{N}$ are severely constrained by the neutrino oscillation data, the precision measurements of weak gauge boson decays and the lepton-flavour-violating (LFV) decays of charged leptons [60–64]. Using the most recent data for the LFV experiments [65–68] we have

$$|\mathcal{N}\mathcal{N}^\dagger| = \begin{pmatrix} 0.994 \pm 0.00625 & < 1.288 \times 10^{-5} & < 8.76356 \times 10^{-3} \\ < 1.288 \times 10^{-5} & 0.995 \pm 0.00625 & < 1.046 \times 10^{-2} \\ < 8.76356 \times 10^{-3} & < 1.046 \times 10^{-2} & 0.995 \pm 0.00625 \end{pmatrix}. \quad (3.12)$$

The diagonal elements of the Eq. 3.12 are from the precision measurements of decays of the weak gauge boson where the SM predictions are 1. The off-diagonal elements are the upper bounds from the LFV decays, e.g., the bounds on the (12) and (21) elements come from the $\mu \to e\gamma$, (23) and (32) elements come from the $\tau \to \mu\gamma$ and (13) and (31) elements come from the $\tau \to e\gamma$ processes respectively. Hence we can estimate ϵ using $\mathcal{N}\mathcal{N}^\dagger \simeq \mathbf{1} - \epsilon$. The stringent bound is coming from the (12) element which is obtained from the $\mu \to e\gamma$ process.

In the minimal scenario, one eigenstate can be predicted as massless. For the light neutrino mass spectrum, we consider both the normal hierarchy (NH) and the inverted hierarchy (IH). In the NH case, the diagonal mass matrix is given by

$$D_{\rm NH} = {\rm diag}\left(0, \sqrt{\Delta m_{12}^2}, \sqrt{\Delta m_{12}^2 + \Delta m_{23}^2}\right), \quad (3.13)$$

while in the IH case

$$D_{\rm IH} = {\rm diag}\left(\sqrt{\Delta m_{23}^2 - \Delta m_{12}^2}, \sqrt{\Delta m_{23}^2}, 0\right). \quad (3.14)$$

For the FND case, we describe ϵ as

$$\epsilon = \frac{1}{M^2} M_D M_D^T = \frac{1}{\mu} U_{PMNS} D_{NH/IH} U_{PMNS}^T, \quad (3.15)$$

and determine the minimum μ value (μ_{min}) so as to give $\epsilon_{12} = 1.288 \times 10^{-5}$ we use the oscillation data. We have found $\mu_{min} = 611.4$ keV and 383.2 keV for the NH and IH cases, respectively. Here we have used the fact that all parameters are real according to our assumption. In this way, we can completely determine the mixing matrices $\mathcal{R}$ and $\mathcal{N}$ considering $\mu = \mu_{\rm min}$, which optimises the production cross sections of the heavy neutrinos at the LHC. We also consider a general parameterization for the neutrino Dirac mass matrix for the FND case. From the inverse seesaw formula,

$$\begin{aligned} m_\nu &= \mu\,\mathcal{R}\,\mathcal{R}^T \\ &= \frac{\mu}{M^2} M_D M_D^T \\ &= U^*_{PMNS}\, D_{NH/IH}\, U^\dagger_{PMNS}, \end{aligned} \tag{3.16}$$

we can generally parameterise $\mathcal{R}$ as

$$\mathcal{R}(\delta,\rho,X,Y) = \frac{1}{\sqrt{\mu}} U^*_{PMNS}\, \sqrt{D_{NH/IH}}\, O, \tag{3.17}$$

where O is a general orthogonal matrix expressed as

$$\begin{aligned} O &= \begin{pmatrix} \cos\alpha & \sin\alpha \\ -\sin\alpha & \cos\alpha \end{pmatrix} \\ &= \begin{pmatrix} \cosh Y & i\sinh Y \\ -i\sinh Y & \cosh Y \end{pmatrix} \begin{pmatrix} \cos X & \sin X \\ -\sin X & \cosh X \end{pmatrix}, \end{aligned} \tag{3.18}$$

with a complex number $\alpha = X + iY$. Thus in this general parameterization we express

$$\begin{aligned} &\epsilon(\delta,\rho,Y) = \mathcal{R}^*\mathcal{R}^T \\ &= \frac{1}{\mu} U_{PMNS}\sqrt{D_{NH/IH}} O^* O^T \sqrt{D_{NH/IH}}^T U^\dagger_{PMNS}. \end{aligned} \tag{3.19}$$

Note that

$$O^* O^T = \begin{pmatrix} \cosh^2 Y + \sinh^2 Y & -2i\cosh Y \sinh Y \\ 2i\cosh Y\sinh Y & \cosh^2 Y + \sinh^2 Y \end{pmatrix} \tag{3.20}$$

is independent of X, and hence the ϵ-matrix is a function of δ, ρ and Y[†].

[†]In this context we point out that we have used the parametrization prescribed in [61] for $\mathcal{N}$, a different parametrization in [69] uses $\mathcal{N} \sim 1-\epsilon$ which over constrains the parameter space by a factor of 2 when calculating $\mathcal{N}\mathcal{N}^\dagger \sim 1-2\epsilon$, which is $1-\epsilon$ in our case.

3.2 Collider Analysis and Results

We are interested in a very specific decay topology arising from the production and decay of heavy sterile neutrinos. The schematic of the prototypical parton level process, at the leading order, is shown in Fig. 3.1.

$$q\,\bar{q}' \rightarrow W^{\pm *} \rightarrow \mu^{\pm} N,\; N \rightarrow \mu^{\mp} W^{\pm},\; W^{\pm} \rightarrow J \tag{3.21}$$

We focus on opposite-sign (OS) muon pair final states, in association with a reconstructed fat jet, at $\sqrt{s} = 13$ TeV LHC. For simplicity, we demonstrate explicitly our analysis assuming a simple, single flavour scenario where the light-heavy mixing is non-zero only for the muon flavour. This is also motivated by the fact that muons provide a clear detection at the LHC with high efficiency and hence is of primary interest. We will however also include the electron channel while discerning the final exclusion results[‡]. As motivated earlier, the OSDL

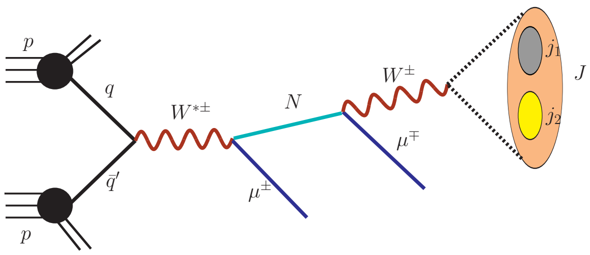

Figure 3.1: Representative parton level diagram for production of heavy neutrino at hadron colliders through off-shell W boson and its decay into an opposite sign muon and W boson. This boosted W originated from a heavier exotic decay results into a fat jet after decaying hadronically.

signature is prone to much larger SM backgrounds – coming from $t\bar{t}$, mono-boson, di-boson and tri-boson productions. This makes the analysis challenging and interesting. Here we will argue and demonstrate that the additional W-like fat jet can be identified effectively by looking at different jet substructure parameters and that this consequently will lead to clear OSDL signatures, emerging over and

[‡]In this article we have studied the $eejj$ and $\mu\mu jj$ signals. We have also used the general parametrization for the detailed analysis. Later we found an article dealing with the OSDL signature with different flavours of the leptons, such as $e\mu jj$ signal [70], studying the lepton flavour violating scenario at the collider.

above the humongous backgrounds.

We generate events using `Madgraph5` (v2.5.4) [71, 72] followed by `Pythia` (v8) [73] for showering and hadronization. To remove the double counting of the shower jets and the matrix element jets, we performed MLM matching [74, 75]. Matched background is generated using the default kt-MLM algorithm with `Xqcut` = 30 GeV and the corresponding jet matching parameter (QCUT) is 1.5 times the `Xqcut` [76]. The parameters p_t^j and ΔR_{jj} are set to zero for `kt-MLM` matching. Subsequent to this, the detector simulation is implemented using `Delphes-v3.4.1` [77]. We use `Fastjet`-v3.3.2 [31] to identify fat jets using the Cambridge-Aachen algorithm [22]. The signal process, generated through the production of intermediate to heavy mass Dirac neutrinos and their boosted decay, is expected to have minor correction from such jet matching. We however included them for completeness to obtain our results. We adopt an `Xqcut` = 70 GeV, or above, for the different mass scenarios we consider. Jet parameters corresponding to $R = 0.8$ and $p_T^{min} = 10$ GeV are adopted.

Opposite-sign di-leptons can arise from different production channels with gauge boson decays. Leptonic decays from $t\bar{t}$ can also give a substantial contribution. Our signal characteristic of a W-like fat jet can be faked by all such channels in association with additional QCD jets. Hence, to be consistent and thorough, all background production channels were produced with additional partons; with proper matching to showers. Moreover, associated $W^{\pm}$ bosons decaying hadronically may also generate irreducible backgrounds. We considered all the relevant dominant SM backgrounds which can mimic the OS di-muon and fat jet signal.

Significantly large contribution can come from Z + jets when the Z boson decays leptonically. This is a large background and can be effectively controlled by applying much stronger cuts on the invariant mass of opposite-sign di-leptons (M_{ll}). QCD jets in these process can be controlled in addition through jet substructure. A significant background is also expected from $t\bar{t}+$ jets, where top decays leptonically. Veto on b-jets and proper implementation of fat jet variables can again control this background. The efficiency of b-tagging is approximately

70% while misidentification of a light parton jet as a b-tagged jet is 1.5% [78]. Additional modes that may contribute include VV + jets and VVV + jets, where either of the vector bosons ($V = W^{\pm}, Z$) decay leptonically to generate di-lepton pairs. Note that a number of these backgrounds subsequently produce missing neutrino(s) and/or missing charged leptons that can substantially add to the missing transverse momentum. In the signal process of interest whereas this is not the case, since we are considering hadronic decays of the $W^{\pm}$. The only dominant source of missing energy in the signal arises from possible jet energy mis-measurements. We use next-to-next-leading order estimate in QCD perturbation theory for the production cross section for Z boson as 2089 pb [79] and $W^{\pm}Z = 51.11$ pb [80]. Furthermore, W^+W^- and W^+W^-Z the production cross section is computed at NLO to be 112.64 pb [81] and 103.4 fb [82] respectively. For $t\bar{t}$ we use production cross section as 835.61 pb computed at N^3LO [83].The next-to-leading order QCD correction for heavy neutrino production and scale uncertainties are studied in [84], see also [85]. For signals, we use the NLO cross section as in [84] for different benchmark mass. Before moving for our analysis we list our basic selection criteria as following.

Primary selection criteria - To identify the leptons as well as the fat jet, we implement the following baseline selection **(C1)** of the events.

- Two opposite sign muons are selected with $p_T > 10$ GeV within the detector rapidity range $|\eta_\mu| < 2.4$, assuming a muon detection efficiency of 95%. We veto the event if any additional reconstructed lepton with $p_T > 10$ GeV is present.
- We demand at least one fat jet, reconstructed adopting the CA algorithm with radius parameter $R = 0.8$ and $|\eta^J| < 2.4$. We select events with the hardest reconstructed fat jet (J_0) having minimum transverse momentum $p_T^{J_0} > 100$ GeV.

Let us now discuss the main kinematic characteristics that may be important in differentiating signal events from the various large backgrounds. Several such features were already identified during the description of the background

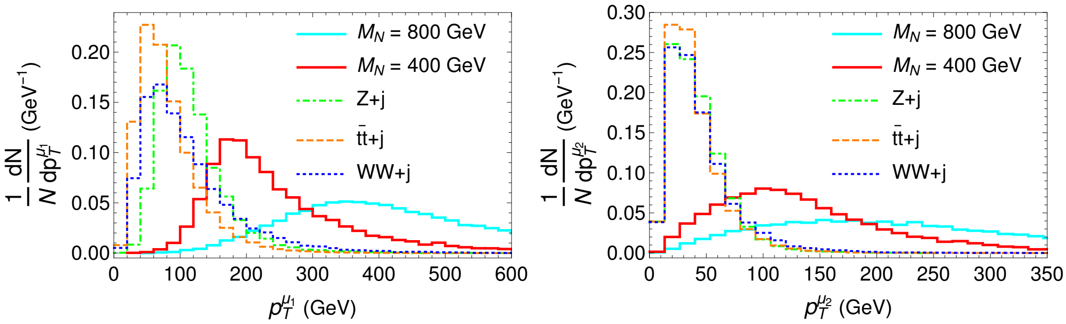

Figure 3.2: Normalised distributions of transverse momentum p_T of leading muon (left) and sub-leading muon (right). These distributions are after the *baseline selection cuts* The distribution of heavy neutrino benchmark points with $M_N = 400$ and 800 GeV is shown along with three dominating background processes.

processes and they were suggestive in their effectiveness in controlling specific background channels. Before moving further, we identify our signal benchmark points – labelled in terms of the sterile neutrino mass M_N and mixing angle $|V_{\mu N}|^2$, they are $M_N = 400$ GeV, 800 GeV and $|V_{\mu N}|^2 = 0.01$. Kinematic distributions are independent of the mixing angle and they are presented as normalised distributions, with differences between signal benchmark points and background processes highlighted. Two extreme mass points are chosen to establish the significantly different kinematic characteristics, which could be leveraged to identify the optimised selection cuts for various masses.

As the two leptons in the signal process are produced at two different stages of decay, they carry distinctly different transverse momentum profiles. The second lepton originating from the heavy neutrino decay is expected to be significantly boosted, since the relevant M_N are large. The hardest lepton in the signal event is hence generally expected from this stage and is expected to peak around $(M_N^2 - M_W^2)/(2M_N)$. This may be noted in Fig. 3.2 (left). All the SM backgrounds display milder hard-lepton transverse momentum profiles in comparison. Distributions for next leading muons is also presented in Fig. 3.2 (right). All these differential distributions are normalised and are shown after applying the above mentioned baseline selection criteria.

Now, let us consider the typical missing transverse momenta distributions for

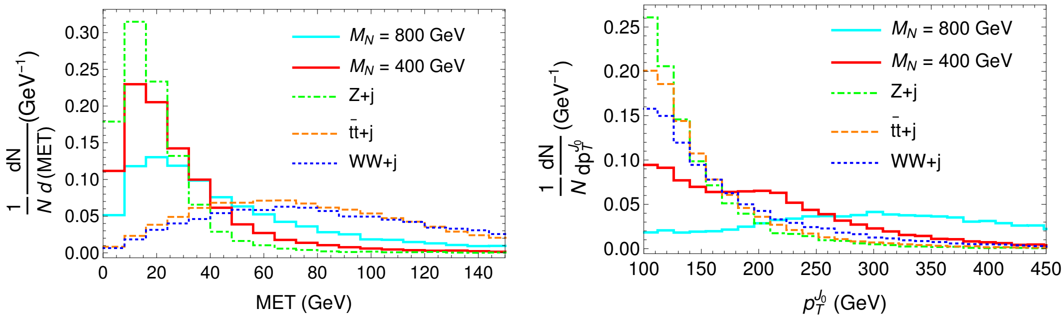

Figure 3.3: Normalised distributions of missing transverse energy (MET) (left) and the transverse momentum of the leading fat jet $p_T^{J_0}$ (right). These distributions are after the *baseline selection cuts*. The distribution of heavy neutrino benchmark points with $M_N = 400$ and 800 GeV is shown along with three dominating background processes.

signal and backgrounds. In Fig. 3.3 (left) we show the missing transverse momentum (MET) distributions for the two benchmark signals and various backgrounds. MET is calculated from the transverse momentum imbalance of all the isolated objects such as leptons, photons and jets, as well as any unclustered deposits. MET for our signal process is expected to be relatively small, affected only by mismeasurements in clustering and jet reconstructions; no missing particles are involved per se. On the contrary, a large fraction of the background processes come with leptons from $W^\pm$ decays which are always associated with corresponding neutrinos. These thereby produce substantial MET contribution over and above contributions from jet mismeasurements. This trend is discernible in the plots.

The next three distributions we discuss primarily define the characteristics of the highest transverse momentum fat jet (J_0), which we rely upon heavily to mitigate backgrounds further. We will primarily utilise fat jet transverse momentum ($p_T^{J_0}$), jet mass (M^{J_0}) and N-subjettiness ($\tau_{21}^{J_0}$) for signal background discrimination and tagging.

Boosted fat jet topologies and their associated jet substructures have proven crucial in various supersymmetric and non-supersymmetric LHC searches [86]. In the $l^\pm l^\mp J$ topology of present interest, the fat jet evolves from the boosted, hadronically decaying $W^\pm$; the right handed sterile neutrinos N_R are heavier than $W^\pm$ giving the latter large boosts. In the analysis, the importance of jet substructure therefore primarily manifests as a means to efficiently tag boosted, hadronically decaying $W^{\pm}$. As mentioned, we will utilise two well-known jet substructure variables towards this requirement – N-subjettiness [29, 30] and jet-mass.

The fat jet appearing from $W^{\pm} \to q\bar{q}'$ potentially retains some information of its two-prong structure. We would like to leverage this aspect to help tag it. N-subjettiness [29, 30] is defined as

$$\tau_N^{(\beta)} = \frac{1}{\mathcal{N}_0} \sum_i p_{i,T} \min \left\{ \Delta R_{i1}^{\beta}, \Delta R_{i2}^{\beta}, \cdots, \Delta R_{iN}^{\beta} \right\}. \tag{3.22}$$

Here, $\mathcal{N}_0 = \sum_i p_{i,T} R_0$ for a jet radius R_0, with i running over the constituent particles, and $p_{i,T}$ is the respective transverse momentum. We compute N-subjettiness with the thrust measure $\beta = 2$. The $\eta - \phi$ distance between a candidate α-subjet and constituent particle i is defined as $\Delta R_{i\alpha} = \sqrt{(\Delta\eta)_{i\alpha}^2 + (\Delta\phi)_{i\alpha}^2}$. N-subjettiness tries to quantify how much the original jet seems to be composed of N daughter subjets. A small value of τ_N suggests that the original jet may consist of N or fewer subjets. It has been demonstrated that a good discriminant to tag an N-subjet object is to consider ratios of adjacent N-subjettiness values [29, 30]. For W-tagging, since the $W^{\pm}$ yields two subjets that are collimated, the variable of interest would therefore be $\tau_{21} = \tau_2/\tau_1$. The mass of the fat jet (M_J), is another discriminant that may be leveraged to identify the jet as originating from a hadronically decaying $W^{\pm}$. The fat jet four momenta is the vector sum of all the constituent four momenta, in the E-scheme. From this reconstructed fat jet four momenta (P_T^J) the invariant fat jet mass (M_J^2) may be computed.

`Delphes 3.3.2` [77] hadron calorimeter outputs are clustered using `FastJet 3.1.3` [31, 87] to reconstruct the candidate fat jet. The N-subjettiness extension, available through `FastJet-contrib`, is used to compute τ_{21}. For tagging the hadronically decaying $W^{\pm}$ we adopt parameter choices from a CMS analysis [88], as a starting point. We choose Cambridge-Achen [22, 89] for the recombination algorithm, with a jet-cone radius $R = 0.8$. Further refinements for W-tagging are then made by requiring specific cuts on τ_{21} and M_J.

The P_T of the boosted $W^{\pm}$ scales as $P_T^W \sim (M_N^2 - M_W^2)/(2M_N)$. Fig. 3.3

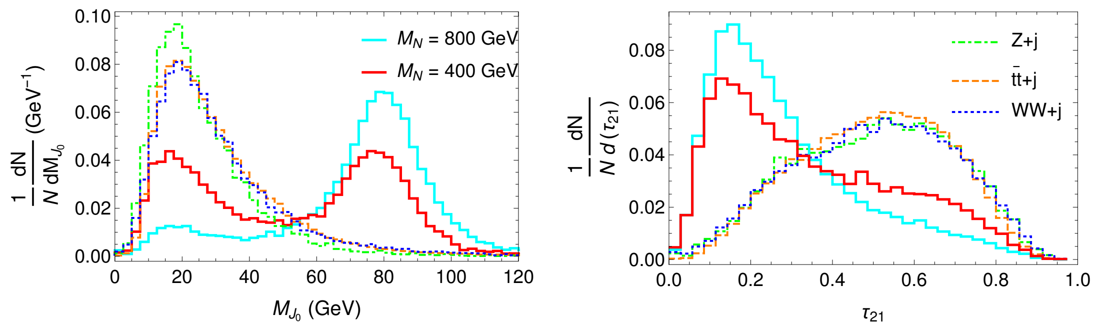

Figure 3.4: Normalised distributions of invariant mass M^{J_0} (left) and N-subjettiness ratio $\tau_{21}^{J_0}$ (right) of the leading fat jet. The selection criteria are same as Fig. 3.2. The distribution of heavy neutrino benchmark points with $M_N = 400$ and 800 GeV is shown along with three dominating background processes.

(right) presents the distributions for fat jet transverse momenta $P_T^{J_0}$. With the minimum transverse momentum of 100 GeV already implemented during primary selection, one notices the spread and second peak (towards higher values) for the signal distributions suggestive of its origin from the decay of the heavy N. This second peak in comparison to one at the lower value becomes more and more prominent as expected for larger M_N. The P_T of candidate fat jets from all background processes monotonously fall. Evidently, larger values for the transverse momentum cut helps us in selecting relatively more signal-like fat jets, in comparison to background events. This may probably be at the cost of some signal events but would nevertheless also help mitigate backgrounds, and potentially result in a net significance gain.

The two plots in Fig. 3.4 highlight the internal characteristics of the identified fat jets, in the form of the invariant jet mass M^{J_0} (left) and the N-subjettiness $\tau_{21}^{J_0}$ (right). These jet substructure variables help correctly tag the candidate fat jet as W-like or not. Construction of these variables are as defined earlier in this section and they provide a powerful tool to discriminate the QCD jet contaminations.

Signal distributions for M^{J_0} clearly peak at M_W reflecting their origin as W-like jets. For low M_N, the $W^{\pm}$ boosts are smaller and with the $P_T > 100\,\text{GeV}$ cut and $R = 0.8$ jet radius some of the $W^{\pm}$ hadronic decay products are not captured inside the cone. This is evident as a secondary, spurious peak at a lower mass value in the plots. However, for heavier M_N or with a choice of a larger transverse momentum cut, only the peak around 80 GeV survives. We retain the P_T cut at

100 GeV, as this gives an overall higher signal significance across the M_N mass ranges under consideration. The most SM backgrounds peak at low M^{J_0}, except those where fat jets are indeed W-like *e.g.* backgrounds from $Z^l W^h$ + jets or $Z^l W^l W^h$ (superscript l/h for leptonic/hadronic decay modes). These particular backgrounds are not shown in the plots for readability and for the reason that their final contributions in the present channel will be minuscule after applying all selection criteria.

The N-subjettiness ratio $\tau_{21} = \tau_2/\tau_1$ is the other jet substructure quantity of interest. It quantifies the two-pronged nature of the fat jet arising from boosted-$W^{\pm}$ hadronic decays and discriminates it from the structureless jets coming from QCD. The distribution of τ_{21} for signal and backgrounds is shown in Fig. 3.4 (right). By construction $\tau_{21}^{J_0}$ for W-like fat jets is expected to peak at low values. The separation between the hadronic decay products of $W^{\pm}$ scale as M_W/P_T^W. It is observed that the W-like fat jets from the signal benchmark points peak around 0.15, whereas most backgrounds with QCD jets peak at much higher values, around 0.6.

With a detailed understanding of the above kinematic and jet substructure variable distributions we are now in a position to make appropriate choices for the final selection criteria. Choice for the final event selection criteria are optimised towards the lower mass regions with the benchmark point at $M_N = 400$ GeV. This is chosen for simplicity of demonstration and the fact that one gets a large cross-section here with a reasonable efficiency from jet characteristics. It nevertheless also provide good signal significance across the full mass range of interest. Various kinematic variables along with fat jet observables are constrained in the following way :

- **C2** The highest p_T muon is selected with $p_T > 100$ GeV and the next p_T ordered muon is selected with $p_T > 60$ GeV. These relatively harder selection criteria are effective in mitigating most of the backgrounds, as motivated from Fig. 3.2. The large $t\bar{t}$ background is reduced without affecting the signal substantially.

- **C3** To control the huge backgrounds coming from leptonic decays of Z

bosons, we veto events if the opposite-sign di-muon invariant mass ($M_{\mu^+\mu^-}$) is less than 200 GeV. The harder cut on $M_{\mu^+\mu^-}$ also reduces parts of the $t\bar{t}$ background further.

- **C4** We apply b-veto to reduce the $t\bar{t}$ background without affecting signal acceptance.

- **C5** As mentioned earlier, it is evident that our signal does not have any missing particle per se, hence should have relatively low MET. The final $\not{p}_T$ would of course get contributions from measurements and uncertainties. Taking into account the unclustered towers, we consider only events with a maximum MET of 60 GeV.

- **C6** Events with the leading fat jet (J_0) having transverse momentum $p_T^{J_0} >$ 150 GeV are selected. This is done in order to increase the purity of the boosted jets further.

- **C7** For signal events, the fat jet is reconstructed from the boosted W boson. Hence, we demand for the corresponding mass, $M^{J0} > 50$ GeV.

- **C8** We choose events with N-subjettiness $\tau_{21}^{J_0} < 0.4$.

- **C9** After identifying $t\bar{t}$ as a major source of irreducible background, one needs to engage some new event constraining variables, beyond just the jet variables. If b-jets, as well as the opposite sign di-leptons are identified, the transverse mass variable M_{T2} [90–92] works exceptionally well—providing a distribution with an upper limit at the top mass. In our present study only one fat jet is identified which can originate from either of the b-jets. In such a scenario, an asymmetric M_{T2}, considering the $b\mu^+\mu^-$ subsystem [93, 94] may be shown to follow the same inequality as before; and thus useful in disentangling the signal, where all decay products are produced from a single prong. We choose $M_{T2}^{(\mu_1\mu_2J_0)} \geq 250$ GeV to reduce $t\bar{t}$ background by a significant amount.

We present the analysis and describe the results explicitly for a few example benchmark signal points – M_N = 300 GeV and 400 GeV – for single flavour

Table 3.1: Expected number of events in $\mu^+\mu^- + J$ channel after implementation of the corresponding event selection criteria for an integrated luminosity of 3000 fb^{-1} at the 13 TeV LHC. We choose the value of mixing angle $|V_{\mu N}|^2$ to be 0.01. The signal events are shown for Dirac neutrino mass $M_N = 300$ and 400 GeV in the case of single flavour.

Cuts		Signal		Background					
		$M_N = 300$(GeV)	$M_N = 400$(GeV)	$Z^l + j$	$t\bar{t} + j$	$W^l\,W^l + j$	$Z^l\,W^h + j$	$Z\,W^l + j$	$Z^l\,W^l\,W^h + j$
C1	Pre-selection + $\mu^+\mu^- + 1J$	1026.85 [100%]	486.05 [100%]	5.1×10^7 [100%]	5.6×10^6 [100%]	2.2×10^5 [100%]	5.7×10^5 [100%]	1.4×10^3 [100%]	120.8 [100%]
C2	$p_T(l_1) > 100$ GeV + $p_T(l_2) > 60$ GeV	787.40 [76.68%]	416.05 [85.59%]	8.9×10^6 [16.88%]	6×10^5 [10.68%]	3.6×10^4 [16.86%]	10.2×10^4 [18.27%]	2737.3 [19.48%]	33.64 [27.85%]
C3	$M_{\mu^+\mu^-} > 200$ GeV	588.50 [57.31%]	349.80 [71.96%]	583.7 [0.0010%]	4.2×10^5 [7.37%]	2.2×10^4 [9.87%]	9.4 [0.0016%]	724.76 [5.15%]	10.42 [8.62%]
C4	b-veto	501.12 [48.80%]	295.7 [60.84%]	530.6 [9.9×10^{-4}%]	6.2×10^4 [1.1%]	2.0×10^4 [9.09%]	8.54 [0.0014%]	647.7 [4.6%]	8.5 [7.06%]
C5	MET < 60	459.29 [44.72%]	263.97 [54.31%]	371.4 [6.9×10^{-4}%]	2.1×10^4 [0.37%]	7796 [3.54%]	6.0 [10.3×10^{-4}%]	353.04 [2.5%]	3.8 [3.13%]
C6	$p_T^{J_0} > 150$ GeV	242.86 [23.65%]	175.75 [36.15%]	265.32 [4.9×10^{-4}%]	7635.9 [0.13%]	3898 [1.77%]	4.27 [7.3×10^{-4}%]	195.96 [1.39%]	2.5 [2.12%]
C7	$M^{J_0} > 50$ GeV	161.43 [15.72%]	132.09 [27.17%]	42.4 [7×10^{-5}%]	1754.2 [0.03%]	843.08 [0.38%]	0.68 [1.2×10^{-4}%]	48.21 [0.34%]	1.3 [1.11%]
C8	$\tau_{21} < 0.4$	141.59 [13.78%]	117.75 [24.22%]	21.18 [3.9×10^{-5}%]	928.6 [0.016%]	396.7 [0.18%]	0.34 [5.8×10^{-5}%]	32.66 [0.23%]	1.0 [0.85%]
C9	$M_{T2}^{(\mu_1\mu_2 J_0)} \geq 250$ GeV	135.55 [13.20%]	113.465 [23.43%]	14.72 [2.7×10^{-5}%]	412.6 [0.007%]	280.0 [0.13%]	0.24 [4.1×10^{-5}%]	23.22 [0.16%]	0.89 [0.74%]

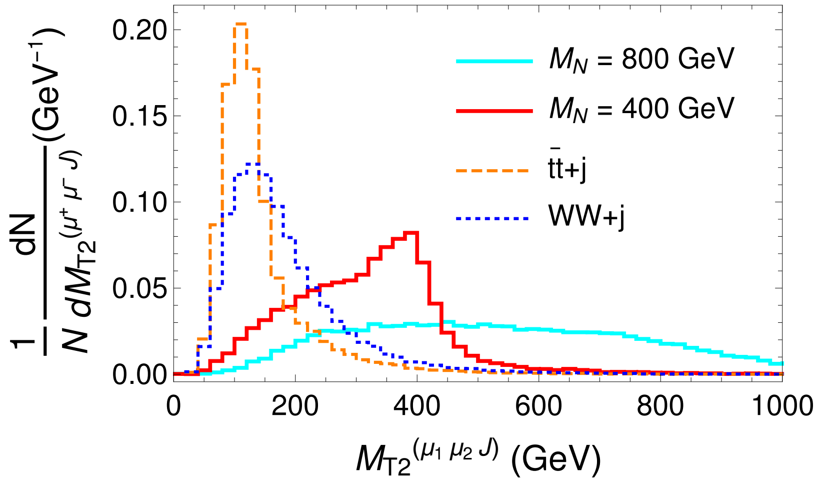

Figure 3.5: Normalised M_{T2} distributions for the two muon and the leading fat jet for an asymmetric subsystem ($\mu_1\mu_2 J_0$) is shown for $M_N = 400$ and 800 GeV along with dominant backgrounds from top-pair and W-pair.

Dirac neutrino, together with the main backgrounds. In Tab. 3.1 we summarise the effect of each selection cut in the order presented before. Expected number of events after baseline selection and the number of surviving events after each subsequent cuts (also in terms of percentages) are presented in the first and successive rows, assuming an integrated luminosity of 3000 fb^{-1}. Here, one can follow sequentially the cut efficiency for the signal and background events as per our previous discussions. It is seen that harder cuts for leptons indeed reduce all the backgrounds, without affecting the signal significantly. One can have an even harder choice for the highest-PT lepton, when probing larger M_N. Veto on b-jets shrinks events from $t\bar{t}$ and missing transverse energy (MET) is effective for all backgrounds possessing additional MET contributions from neutrinos. The other three selections in the form of $p_T^{J_0}$, M^{J0} and $\tau_{21}^{J_0}$ rely on the fat jet substructure and reduce all dominant backgrounds where fat jets are mimicked by QCD jets. We further use $M_{T2}^{\mu_1\mu_2 J_0}$ to reduce the dominant $t\bar{t}$ background. Overall efficiency for the 400 GeV signal can be observed to be around 23 %, whereas different backgrounds are reduced to between 2.7×10^{-5} % and 0.74 %. Note that the signal cross-section for heavier mass falls significantly, due to production s-channel suppression. However, better substructure efficiencies partially mitigate that reduction. This is evident from the $M_N = 300$ GeV and 400 GeV results. Statistical significances for the observed signal events (S) over the total

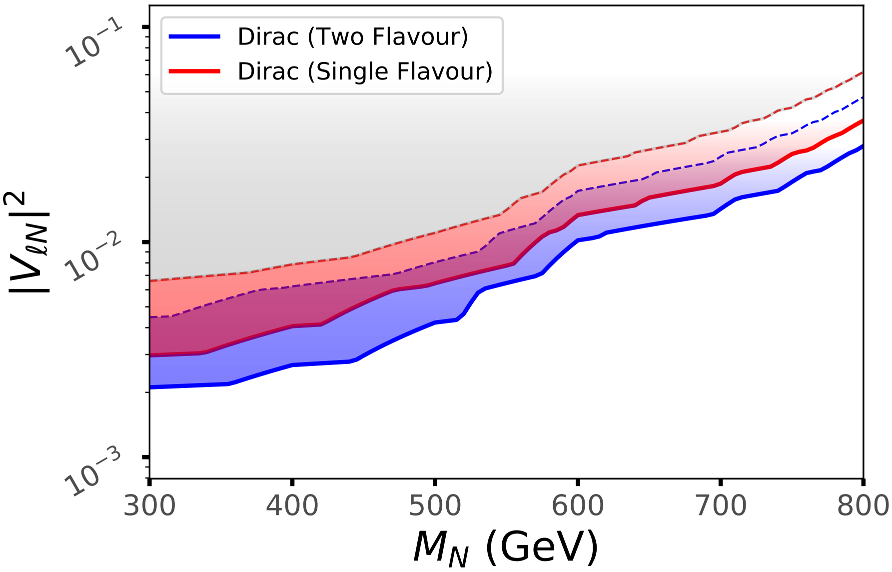

Figure 3.6: The figure shows the 2 σ exclusion limits, in terms of heavy neutrino mass M_N and $|V_{\ell N}|^2$, at 3000 fb^{-1} of integrated luminosity at the 13 TeV LHC. Where dotted line corresponding to each colour represents the 5% systematics uncertainty in the total background estimation.

irreducible standard model backgrounds (B) are calculated adopting the familiar expression $\mathcal{S} = \sqrt{2 \times ((S+B)\ln(1+S/B) - S)}$.

3.2.1 Flavor diagonal case

In this section we study the FD scenario where the two degenerate RHNs are equally mixed with the e and μ leptons. After the signal and SM background analyses we have displayed the exclusion limits on the $|V_{\ell N}|^2$ as a function of the M_N in Fig. 3.6. To account for the effects coming from systematics, we consider a characteristic 5% systematics uncertainty from ref. [95] in the background estimation; which is represented by dotted line, corresponding to two cases in Fig. 3.6. Furthermore, note that in any actual analyses, data driven techniques, for instance utilising ant b-jet vetoes or ABCD type methods, will help significantly reduce systematic uncertainties in background estimations [96]. We have assumed 3000 fb^{-1} integrated luminosity at 13 TeV LHC. There is no direct search result for the RHNs at this mass range for the inverse seesaw scenario at the colliders. For the Heavy Majorana neutrino, if exits in nature, should also show up

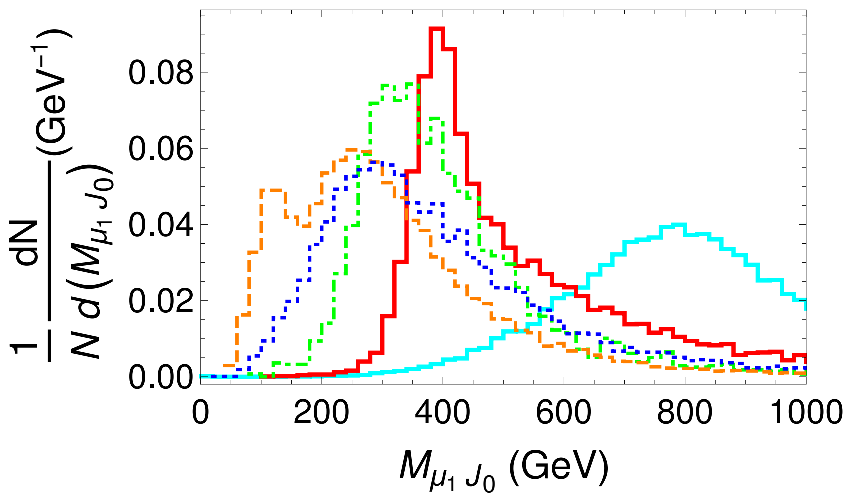

Figure 3.7: Normalised invariant mass distributions for the hardest lepton and the leading fat jet system ($M_{\mu_1 J_0}$) is shown for $M_N = 400$ and 800 GeV with dominant backgrounds. Choice of line colors and types are similar to previous Fig. 3.4

in equal strength producing lepton number violating same sign di-leptons, where backgrounds are immensely suppressed. Evidently SSDL bounds are extremely strong and studied extensively [97] in seesaw framework along with fat jet. Corresponding efficiency for selecting muon signals is at 70% while it is reduced to 50% for electron events. For different seesaw models, the exclusion limits for lower M_N values can be as low as 2×10^{-3}. The heavy neutrino production, especially at heavier mass, can get $(10\% - 60\%)$ additional contribution for the mass limit under consideration from $\gamma - W^{\pm}$ fusion [98,99], and thus can potentially improve the exclusion limits further. The results for the 2-flavour (1-flavour) case up to $M_N = 550$ GeV (500 GeV) are better than the optimistic scenario mentioned in [100] from the electroweak precision measurement in [101,102]. The optimistic limit on $|V_{\mu N}|^2$ has been mentioned as 6.0×10^{-3} in [100].

We reiterate that the given limits are based on simple criteria, optimised at $M_N = 400$ GeV. There is ample scope for improvements at higher masses. One can readily recognise the quantities which may crucially factor in for higher masses. For instance, RHN possessing mass of several hundreds of GeV would often produce both boosted leptons as well as collimated jets from boosted W bosons. P_T of hardest lepton will evidently shift towards higher values in Fig. 3.2 for these heavier masses, and the peak position will be around half of relevant

Cut	Signal		Background	
	$M_N = 600$	800	$t\bar{t} + j$	$W^l W^l + j$
Table I + $p_T(l_1) > 200$ GeV $M_{l_1 J_0} > 500$ GeV	40.01 [32.3%]	11.65 [33.62%]	180.5 $[3.2 \times 10^{-3}\%]$	154 [0.07%]

Table 3.2: Expected number of events after implementing additional cuts (together with cuts described in Tab. 3.1) suited for higher mass probe, *i.e.* $M_N > 600$GeV. The signal events are shown for Dirac neutrino in the case of single flavour. Only two dominant backgrounds are presented here.

heavy neutrino mass. We also illustrated the invariant mass of this hardest lepton and the fat jet system, in Fig. 3.7, which peaks around the benchmark heavy neutrino mass. Effective use of these two variables, as shown in Tab. 3.2, can provide an improvement by a factor of slightly more than two, for the $|V_{lN}|^2$ limits; for the heavy-neutrino masses greater than $M_N = 600$ GeV.

3.2.2 General parametrization: Flavor non diagonal case

In this section we study the flavour non diagonal (FND) scenario where the flavour structure is carried out by the Dirac Yukawa coupling. According to our formalism the mixing between the light and heavy neutrinos ($\mathcal{R} = V_{\ell N}$) is a function of the Dirac phase (δ) and the Majorana phase (ρ). $\mathcal{R}^* \mathcal{R}^T$ is a function of the general parameter Y coming from the general orthogonal matrix O. We perform a parameter scan by varying these parameters between $-\pi \leq \delta, \rho \leq \pi$ with an interval of $\frac{\pi}{20}$ and $0 \leq Y \leq 1$ with an interval of 0.02. The elements of the Dirac mass matrix grow exponentially with $|Y|$. For a value $Y > 1$, the neutrino oscillation data are realised under the fine-tuning between the large elements. Although the neutrino oscillation data are correctly reproduced for any values of Y in the general parametrization, we only consider $Y \leq 1$ to avoid the fine-tuning. The ranges of the independent parameters like δ, ρ and Y satisfy the constraints on ϵ. Hence we calculate the cross section for the $i-$th generation RHN at the

Mixing Angles	Calculated upper limits	EWPD [103–105]
$\lvert V_{eN}\rvert^2$ (NH)	6.908×10^{-4}	1.68×10^{-3}
$\lvert V_{eN}\rvert^2$ (IH)	1.884×10^{-4}	
$\lvert V_{\mu N}\rvert^2$ (NH)	8.963×10^{-4}	9.0×10^{-4}
$\lvert V_{\mu N}\rvert^2$ (IH)	1.923×10^{-4}	

Table 3.3: Calculated upper limits on the mixing angles for the NH and IH cases and comparison with the EWPD

LHC through the W boson exchange process $u\overline{d} \to \ell_\alpha^+ N_i$ and $d\overline{u} \to \ell_\alpha^- \overline{N_i}$. Hence the production cross section at the LHC can be written as

$$\sigma(q\overline{q'} \to \ell_\alpha N_i) = \sigma_{\text{LHC}} |\mathcal{R}_{\alpha i}(\delta, \rho, Y)|^2 \tag{3.23}$$

where σ_{LHC} is the production cross section the RHNs at the LHC. The partial decay widths of the RHN ($N_i \to \ell_\alpha W^+ / \nu_\alpha Z / \nu_\alpha h$) can be found by multiplying the corresponding decay widths by $|\mathcal{R}_{\alpha i}(\delta, \rho, Y)|^2$. As a result the corresponding branching ratios can be expressed in terms of δ, ρ and Y through the elements of the mixing matrix. Varying the parameters within the allowed ranges and satisfying the constraints obtained from $\mathcal{N}\mathcal{N}^\dagger \simeq 1 - \epsilon$ we obtain the upper limits on the mixing angles for the NH and IH cases with two electron ($|V_{eN}|^2$) and two muon ($|V_{\mu N}|^2$) final states, respectively in Tab. 3.3. We compare our results with the bounds obtained from the EWPD [103–105] on $|V_{eN}|^2$ (1.68×10^{-3}) and $|V_{\mu N}|^2$ (9.0×10^{-4}) respectively.

We notice that the allowed upper limit on $|V_{\mu N}|^2$ and $|V_{eN}|^2$ in the NH and IH cases are below the corresponding EWPD limits.

Fig. 3.8 shows the results of the parameter scan of the pseudo-Dirac RHN production cross section in the same flavour OSDL final state with a pair of jets coming from leading RHN production followed by its decay into a leading mode, $pp \to N\ell, N \to W\ell, W \to jj$ for $\ell = e$ or μ flavours at the LO for a benchmark value $M_N = 175$ GeV at the 13 TeV LHC. We have three other benchmark points for M_N such as 200 GeV, 250 GeV and 300 GeV.

Each point in the shaded region of the Fig. 3.8, based on Y or δ parameter dependance, satisfy all the experimental constraints imposed on ϵ-matrix. The left two columns in upper (lower) row of Fig. 3.8 show the NH cases whereas the right two columns for the IH cases considering the production of $e^{\pm}e^{\mp}jj$ ($\mu^{\pm}\mu^{\mp}jj$) events respectively. The estimated NLO cross sections ($\sigma_{\rm LHC}^{NLO}$) have been listed in Tab. 3.4 matching [84] satisfying all the constraints imposed on the ϵ-matirx.

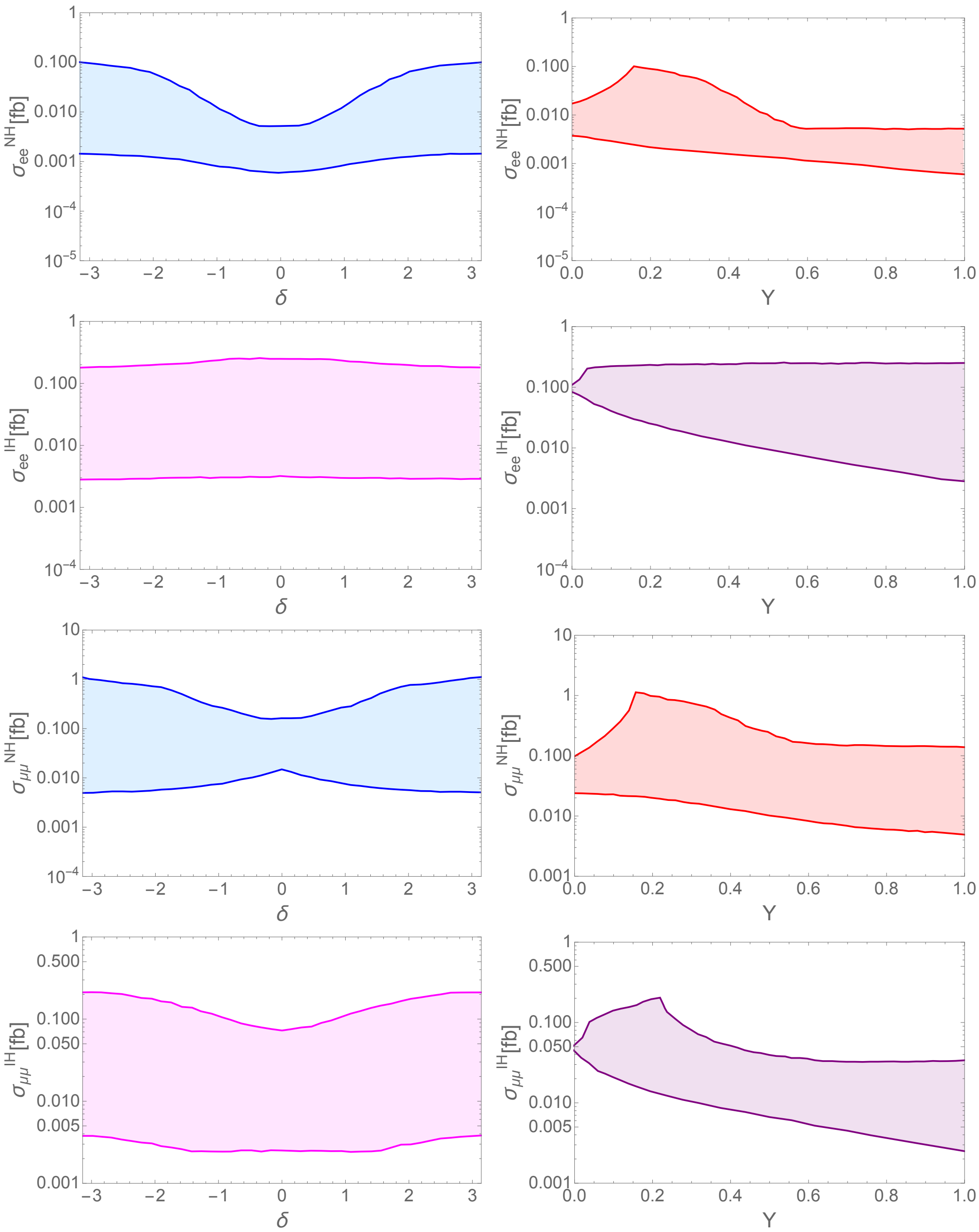

Figure 3.8: LO cross section at the 13 TeV LHC for the (upper row) $e^{\pm}e^{\mp}jj$ and (lower row) $\mu^{\pm}\mu^{\mp}jj$ final state in the general parametrization applying the constraints on the ϵ-matrix. Y and δ parameter dependance were shown, where the left two columns stand for the NH cases whereas the right two columns for the IH case.

M_N (GeV)	$e^{\pm}e^{\mp}jj$ (fb)		$\mu^{\pm}\mu^{\mp}jj$ (fb)	
	IH	NH	IH	NH
175	0.3232	0.1281	0.233	1.43
200	0.1837	0.0762	0.131	0.7254
250	0.07623	0.0294	0.055	0.271
300	0.0386	0.01562	0.0276	0.138

Table 3.4: Estimated signal cross sections at the NLO level σ_{LHC}^{NLO} for a 13 TeV LHC for different benchmark values of M_N.The second (third) column represents the $e^{\pm}e^{\mp}jj$ final state for the IH (NH) case. The fourth (fifth) column represents the $\mu^{\pm}\mu^{\mp}jj$ final state for IH (NH) case under the FND scenario.

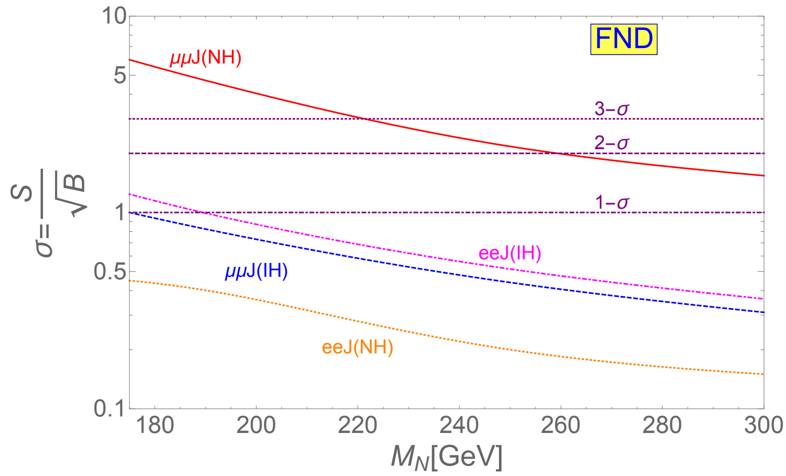

Figure 3.9: Significance reach as a function of M_N for the FND case at the 13 TeV LHC with 3000 fb^{-1} luminosity considering the constraints on the ϵ-matrix.

The efficiencies have been estimated using the cuts flow between C1-C8 used for the events as shown in Tab. 3.1 for the different benchmark values of M_N. The efficiencies are 3.64%, 4.93%, 7.07% and 9.84% for $M_N = 175, 200, 250$ and 300 GeV respectively for the $e^{\pm}e^{\mp}J$ signal. On the other hand the cut efficiencies are 5.10%, 6.90%, 9.9% and 13.78% for the corresponding muon signals. We use the upper limits on $|V_{eN}|^2$ and $|V_{\mu N}|^2$ for the NH and IH cases for the ee and $\mu\mu$ signals from Tab. 3.3. The total SM backgrounds (B) have been estimated in the Tab. 3.1 as 986.06 (1380.50) for the $e^{\pm}e^{\mp}J(\mu^{\pm}\mu^{\mp}J)$. Hence we estimate the maximum signal events ($S^{\rm NH/IH}$) for $\ell^{\pm}\ell^{\mp}J$ ($\ell = e$ or μ) for the different benchmark values of M_N using the luminosity of 3000 fb^{-1} at the 13 TeV LHC for the NH and IH cases. Using such signal and background events, we estimate the significance of the signal events $\sigma^{\mathrm{NH/IH}} = \dfrac{S^{\mathrm{NH/IH}}}{\sqrt{B}}$ at the different benchmark values of M_N for the NH and IH cases. Significances reach as a function of heavy neutrino mass M_N are plotted in Fig. 3.9. While all other cases are expected to remain unconstrained, normal hierarchy in this general parametrization can be interesting in this OSDL muon search channel, especially at the lower mass region. Even with a relatively small signal efficiency, $M_N = 175$ GeV RHN with this flavour structure can be probed more than 5 σ significance using the muon channel, where as $M_N \leq 222$ GeV can be probed up to ≥ 3 σ.

3.3 Summary and Conclusion

The Seesaw framework gives an elegant but simple mechanism for tiny neutrino masses and flavour mixings. If the sterile neutrinos in these models appear close to the electroweak scale, they may be probed at the 13 TeV LHC. Conventionally such searches for heavy neutrinos, Majorana or pseudo-Dirac, are made in the di-lepton+jets or trilepton channels. Jet substructure methods have been relatively underutilised in these contexts.

The opposite-sign di-lepton state is expected to encounter a huge standard model background. This channel is nevertheless very important as it may be the only final state, with jets, for a class of models with Dirac or pseudo-Dirac type neutrinos. Hence, strategies to effectively investigate the opposite-sign di-lepton along with a fat jet would greatly broaden the scope of collider sterile neutrino searches – both in terms of probing model aspects as well as uncovering the nature of the heavy sterile neutrinos.

In the present analysis we propose a new strategy to search for intermediate to heavy mass sterile neutrinos, when their decays lead to boosted fat jets arising from W boson hadronic decays. By looking into the jet substructure characteristics, boosted jets reveal useful information on their origin and topology. We leveraged the same to achieve good discrimination between signal and background in the opposite-sign di-lepton+fat jet channel. The computed signal significance and LHC limits for different model scenarios are shown to be competitive and at least an order of magnitude better than existing limits.

We also investigate the lepton flavour conserving modes in the flavour non-diagonal cases, for electron and muon flavours both in normal as well as inverted hierarchy. Such models are studied after utilizing extensive constrains coming from neutrino oscillation data, lepton flavour violation constraints and LEP considerations with general parametrization being constrained by non-unitarity. For $M_N = 175$ GeV, a signal $\mu^\pm\mu^\mp$+fat jet with a significance more than 5 σ in the NH case can potentially be constrained in the near future at the 13 TeV LHC, with a luminosity of 3000 fb^{-1}.

Chapter 4

Discovery prospect of Inert Higgs Doublet

In this chapter, we explore the inert doublet model (IDM) which is well motivated among the minimal consistent dark matter models. This model provides the full observed relic density in two scenarios one in the case of hierarchical mass spectrum and the other in the case of the degenerate mass spectrum. We focus our study for the hierarchical spectrum which can not be cover by the usual monojet + $\not{E}_T$ searches. Hence we propose [106] a dedicated search topology (di-fat jet + $\not{E}_T$) using jet-substructure and MVA technique to uncover this parameter space at LHC.

We briefly discuss the IDM in Sec. 4.1, outlining its scalar sector. Next, in Sec. 4.2, we invoke all the possible theoretical, collider and astrophysical constraints applicable to the IDM. Subsequently, in Sec. 4.3, we discuss four possible DM scenarios depending on the DM mass and its mass differences to the other BSM scalars to motivate our choice of benchmark points. To define our analysis set-up, we list the possible IDM processes contributing to our signal process, di-fat jet plus $\not{E}_T$ channel in Sec. 4.4. In Sec. 4.5, cut based analysis and in Sec. 4.6, we improve our probe using MVA to recast the signal vs background numbers with non-rectangular cuts and therefore, having better sensitivity for the LHC search. Finally, we summarise our results and conclude in Sec. 4.7.

4.1 Inert Doublet Model

We consider inert doublet model (IDM) where one adds an additional $\mathrm{SU}(2)_L$ complex scalar doublet Φ_2 apart from the SM Higgs doublet Φ_1, which are, respectively, odd and even under a discrete $\mathbb{Z}_2$ symmetry, *i.e.* $\Phi_1 \to \Phi_1$, $\Phi_2 \to -\Phi_2$. The most general scalar potential that respects the electroweak symmetry $\mathrm{SU}(2)_L \otimes \mathrm{U}(1)_Y \otimes \mathbb{Z}_2$ of the IDM can be written as [107],

$$\begin{aligned} V(\Phi_1,\Phi_2) &= \mu_1^2 \Phi_1^\dagger \Phi_1 + \mu_2^2 \Phi_2^\dagger \Phi_2 + \lambda_1 (\Phi_1^\dagger \Phi_1)^2 + \lambda_2 (\Phi_2^\dagger \Phi_2)^2 + \lambda_3 \Phi_1^\dagger \Phi_1 \Phi_2^\dagger \Phi_2 \\ &\quad + \lambda_4 \Phi_1^\dagger \Phi_2 \Phi_2^\dagger \Phi_1 + \frac{\lambda_5}{2}\left[(\Phi_1^\dagger \Phi_2)^2 + H.c.\right], \end{aligned} \tag{4.1}$$

where Φ_1 and Φ_2 both are hypercharged, $Y = +1$, and can be written as

$$\Phi_1 = \begin{pmatrix} G^+ \\ \dfrac{v + h + iG^0}{\sqrt{2}} \end{pmatrix}, \quad \Phi_2 = \begin{pmatrix} H^+ \\ \dfrac{H + iA}{\sqrt{2}} \end{pmatrix}. \tag{4.2}$$

Here, h is the SM Higgs with G^+, G^0 being the charged and neutral Goldstone bosons, respectively. The charged scalar H^+ is present in Φ_2, along with the neutral scalars, H, A, respectively, being CP-even and CP-odd. For the vacuum expectation values (*vev*s) of the two doublets, we adopt the notation $\langle \Phi_1 \rangle = v/\sqrt{2}$, $\langle \Phi_2 \rangle = 0$, keeping in mind the exact nature of the $\mathbb{Z}_2$ symmetry. The zero *vev* of Φ_2 is responsible for the inertness of this model. Since all the SM fermions are even under $\mathbb{Z}_2$, the new scalar doublet does not couple to the SM fermions and thus having no fermionic interactions. The scalar-gauge boson interactions originate through the kinetic term of the two doublets

$$\mathcal{L}_{kin} = (D_\mu \Phi_1)^\dagger (D^\mu \Phi_1) + (D_\mu \Phi_2)^\dagger (D^\mu \Phi_2). \tag{4.3}$$

All parameters in the scalar potential are assumed to be real in order to keep the IDM CP-invariant.

Here, the electroweak symmetry breaking takes place through the SM doublet Φ_1 getting a *vev*, and after this, the masses of the physical scalars at tree level can be written as

$$\begin{aligned}
m_h^2 &= 2\lambda_1 v^2, \\
m_{H^\pm}^2 &= \mu_2^2 + \frac{1}{2}\lambda_3 v^2, \\
m_H^2 &= \mu_2^2 + \frac{1}{2}(\lambda_3 + \lambda_4 + \lambda_5)v^2 = m_{H^\pm}^2 + \frac{1}{2}\left(\lambda_4 + \lambda_5\right)v^2, \\
m_A^2 &= \mu_2^2 + \frac{1}{2}(\lambda_3 + \lambda_4 - \lambda_5)v^2 = m_{H^\pm}^2 + \frac{1}{2}\left(\lambda_4 - \lambda_5\right)v^2.
\end{aligned} \tag{4.4}$$

Here, m_h is the SM-like Higgs boson mass, and $m_{H(A)}$ are the masses of the CP-even (odd) scalars from the inert doublet, while $m_{H^\pm}$ is the charged scalar mass. Either of the neutral scalars can be the DM candidate in this IDM framework since DM observations can not probe the CP-behaviour. For the present analysis, we consider the CP-even scalar H as the DM candidate, which corresponds to negative values of λ_5 parameter. We define $\lambda_3 + \lambda_4 + \lambda_5 = \lambda_L$, which can be either positive or negative. The relations between the λ's and the scalar masses get modified when the QED corrections are considered for both the scalar masses and scalar potential parameters. As the inert scalars do not couple to the SM quarks, higher-order QCD corrections are negligible for these parameters.

Compared to the SM, only the scalar sector is modified in the IDM. Similar to the SM, λ_1 and μ_1^2 are determined by $m_h \approx 125$ GeV and $v \approx 246$ GeV. There are five free parameters in the scalar sector of the IDM viz. λ_L, λ_2, m_A, $m_{H^\pm}$, and m_H that are expressed in terms of the five scalar potential parameters, μ_2^2 and $\lambda_{2,3,4,5}$, as shown in Eq. 4.4. The new doublet, being inert to the SM fermionic sector, does not introduce any additional new parameters in this set-up. In IDM the contribution of the self coupling parameter λ_2 is mostly limited to fixing unitarity and stability of the potential. It does not affect the scalar masses and their phenomenology. The Higgs portal coupling λ_L to the chosen DM candidate H determines the rate of the DM annihilation through the Higgs and therefore, is an essential parameter in the DM sector along with the DM mass $m_{DM} = m_H$. The collider phenomenology of the IDM depends on the scalar masses $m_{H^\pm}, m_A$ and m_H, as the mass differences between them play a significant role in proposing the search channels for different scenarios.

4.2 Constraints on the Inert Doublet Model

The IDM parameter space is constrained from various theoretical as well as experimental considerations. In the model, we have an extra doublet which brings extra parameters in the scalar potential. Therefore, it is imperative to check whether the extended potential is bounded from below, *i.e.*, stable at tree level along with the potential parameters being within the unitary and perturbative regime. With the presence of the extra doublet, oblique parameters should be re-examined with respect to the presence of a light DM and custodial symmetry breaking, respectively. The presence of light scalars can also upset the LEP constraints and the Higgs invisible decay limits. Since DM is present in the model, we should satisfy the observed relic density keeping the DM-nucleon interactions below the DM direct detection reach.

4.2.1 Theoretical constraints

The scalar sector is modified in the IDM. We ensure the enlarged potential is stable, *i.e.*, not unbounded from below and the global minimum is a neutral one. We also checked if the potential parameters are perturbative at the tree level along with satisfying unitarity bounds.

Bounded from below: Theoretical constraints on quartic potential parameters (λ's) can arise from restricting the scalar potential in Eq. 4.1 not to produce large negative numbers for large field values, *i.e.* $V > 0 \; \forall \; \Phi_i \to \pm\infty$. The mixed quartic terms can be combined to form complete square terms and demanding their coefficients to be positive, leads to the following conditions *.

$$\lambda_1 > 0, \quad \lambda_2 > 0, \quad \lambda_3 + 2\sqrt{\lambda_1\lambda_2} > 0, \quad \lambda_3 + \lambda_4 + \lambda_5 + 2\sqrt{\lambda_1\lambda_2} > 0. \tag{4.5}$$

Because of the introduction of new scalars, there are possibilities of having multiple minima. For the inert vacuum to be the global minimum, we restrict it

*Alternately, for a scalar potential with many quartic couplings, one can consider formulating the copositive matrices to guarantee the boundedness of the potential [108].

from being charged by ensuring the condition

$$\lambda_4 + \lambda_5 < 0. \tag{4.6}$$

We also ensure that the global minimum is the inert vacuum as opposed to an inert-like one, with the imposition of the condition [109,110]

$$\frac{\mu_1^2}{\sqrt{\lambda_1}} - \frac{\mu_2^2}{\sqrt{\lambda_2}} > 0. \tag{4.7}$$

Perturbativity and unitarity: We form the S-matrix with the amplitudes computed from the $2 \to 2$ scalar scattering processes taking into account all the other quartic terms in the scalar potential. The eigenvalues of the S-matrix turn out to be some combinations of these couplings. The perturbative unitarity constraints on those eigenvalues are $|\Lambda_i| \leq 8\pi$, where the scattering matrix provides us the combinations as

$$\begin{aligned}
\Lambda_{1,2} &= \lambda_3 \pm \lambda_4; \quad \Lambda_{3,4} = \lambda_3 \pm \lambda_5; \quad \Lambda_{5,6} = \lambda_3 + 2\lambda_4 \pm 3\lambda_5; \\
\Lambda_{7,8} &= -\lambda_1 - \lambda_2 \pm \sqrt{(\lambda_1 - \lambda_2)^2 + \lambda_4^2}; \\
\Lambda_{9,10} &= -3\lambda_1 - 3\lambda_2 \pm \sqrt{9(\lambda_1 - \lambda_2)^2 + (2\lambda_3 + \lambda_4)^2}; \\
\Lambda_{11,12} &= -\lambda_1 - \lambda_2 \pm \sqrt{(\lambda_1 - \lambda_2)^2 + \lambda_5^2}.
\end{aligned} \tag{4.8}$$

4.2.2 Collider constraints

Precision measurements at the LEP and the LHC contributed in pinning down the trace of new physics effects in different forms. The effects of hierarchical heavy BSM scalar mass spectrum and the presence of a lighter DM are under consideration. After the discovery of the Higgs boson, the LHC also measured its properties. Two such measurements, the Higgs decay to $\gamma\gamma$ and its invisible decay are important to consider in the context of IDM.

Oblique correction constraints: The oblique parameters S, T and U, proposed by Peskin and Takeuchi [111], are different combinations of the oblique corrections, *i.e.*, radiative corrections to the two-point functions of the SM gauge bosons. The

S parameter encodes the running of the neutral gauge boson two-point functions ($\Pi_{ZZ}, \Pi_{Z\gamma}, \Pi_{\gamma\gamma}$) in the lower energy range, from zero momentum to the Z-pole. Therefore, the S parameter is sensitive to the presence of light particles with masses below m_Z, which is the case here due to the presence of the light DM. The T parameter, on the other hand, measures the difference between the WW and the ZZ two-point functions, Π_{WW} and Π_{ZZ}, at zero momentum. Mass splitting of the scalars inside a $\mathrm{SU}(2)_L$ doublet breaks the custodial symmetry which modifies T. In the IDM, the mass splittings between the neutral and the charged scalars are controlled by the T parameter. The experimentally measured values of oblique parameters that we use in our analysis are [112]:

$$S = 0.05 \pm 0.11; \quad T = 0.09 \pm 0.13; \quad U = 0.01 \pm 0.11. \tag{4.9}$$

<u>*$h \to \gamma\gamma$ signal strength constraint:*</u> The signal strength for the $h \to \gamma\gamma$ channel is given by the following ratio [113, 114],

$$R_{\gamma\gamma} = \frac{\sigma(pp \to h)}{\sigma(pp \to h_{\mathrm{SM}})} \times \frac{\mathrm{BR}(h \to \gamma\gamma)}{\mathrm{BR}(h_{\mathrm{SM}} \to \gamma\gamma)}. \tag{4.10}$$

In the IDM, the Higgs production rate is similar to that of the SM, as it is gluon fusion dominated in both the models. So, in the IDM, the ratio can be approximated as

$$R_{\gamma\gamma} = \frac{\mathrm{BR}(h \to \gamma\gamma)_{\mathrm{IDM}}}{\mathrm{BR}(h \to \gamma\gamma)_{\mathrm{SM}}}. \tag{4.11}$$

Combined CMS and ATLAS fit in the diphoton channel provides a 2 σ limit on this observable as [115],

$$R_{\gamma\gamma} = 1.14^{+0.38}_{-0.36}. \tag{4.12}$$

Presence of a charged Higgs in the $h \to \gamma\gamma$ decay loop can induce a significant shift in this ratio for large values of hH^+H^- coupling. In the IDM, this coupling depends on λ_3 which is also related to the charged Higgs mass and this parameter is constrained from the allowed range of the ratio $R_{\gamma\gamma}$ that can deviate from unity [†].

<u>*Constraint from the Higgs invisible decay:*</u> Another constraint from the Higgs data, applicable for the scenario when Higgs can decay to a pair of DM particles with a mass $m_{DM} < m_h/2$. The invisible decay width is given by

$$\Gamma(h \to \text{Invisible}) = \frac{\lambda_L^2 v^2}{64\pi m_h}\left(1 - \frac{4\,m_{DM}^2}{m_h^2}\right)^{\frac{1}{2}}. \tag{4.13}$$

The latest ATLAS constraint on the invisible Higgs decay is [116]

$$\text{BR}(h \to \text{Invisible}) = \frac{\Gamma(h \to \text{Invisible})}{\Gamma(h \to \text{Invisible}) + \Gamma(h \to \text{SM})} < 22\%.$$

In the case for light DM when the Higgs decay to a pair of DM particles is kinematically allowed, this limit can significantly constrain the parameter space of the IDM.

<u>*LEP bounds:*</u> A reinterpretation of the neutralino search results at the LEP-II has ruled out the parameter regions [117, 118] that satisfy the following three conditions

$$m_H < 80 \text{ GeV}, \;\; \mathrm{m_A} < 100 \text{ GeV} \;\&\; \mathrm{m_A} - \mathrm{m_H} > 8 \text{ GeV}. \tag{4.14}$$

Reinterpretation of chargino search results at the LEP-II has put a bound [119] on the charged Higgs mass as,

$$m_{H^+} > 70 \text{ GeV}. \tag{4.15}$$

A hierarchical IDM scalar spectrum is not restricted from these constraints. Moreover, due to large mass gap in the spectrum, $Z \to HA, W^\pm \to HH^\pm, W^\pm \to AH^\pm$ off-shell decays have a negligible effect on the total width of the W and Z bosons, that are very precisely measured at the LEP experiments.

[†] In the IDM, only the Higgs decay rate to $\gamma\gamma$ can deviate from the SM value at the leading order. As that deviation is within the experimental limit, the Higgs boson here easily satisfies all Higgs signal data.

4.2.3 Astrophysical constraints

This model contains a DM candidate, the CP-even scalar in Φ_2. Therefore, astrophysical constraints on this model consist of the DM relic density and the direct probe of DM in the Xenon and LUX experiments.

Relic density: There are unputdownable observational pieces of evidence of the presence of DM in a vast range of length scale, starting from intergalactic rotation curve to the latest Planck experiment data. That suggests the current density of the DM comprises approximately 26% energy budget of the present Universe. The observed abundance of DM is usually represented in terms of density parameter Ω as [120]

$$\Omega_{\rm DM} h^2 = 0.1187 \pm 0.0017 \tag{4.16}$$

where the observed Hubble constant is $\mathcal{H}_0 = 100\, h\, km\, s^{-1}\, Mpc^{-1}$. The rate of DM annihilation to the SM particles is inversely proportional to the relic of the DM, and therefore constraints are imposed to avoid the overproduction of the relic in the IDM. We compute the DM relic density numerically with MicrOmega [121], implementing the IDM details there.

Direct detection constraints: Along with the constraints from the relic abundance measurement in the Planck experiment, there exist strict bounds on the DM-nucleon cross section from the DM direct detection experiments like Xenon100 (Xenon1T) [122] and more recently from LUX [123]. For scalar DM considered in this work, the spin independent DM-nucleon scattering cross section mediated by the SM Higgs is given as [124]

$$\sigma_{\rm SI} = \frac{\lambda_L^2 f^2}{4\pi} \frac{\mu^2 m_n^2}{m_h^4 m_{DM}^2}, \tag{4.17}$$

where $\mu = m_n m_{DM}/(m_n + m_{DM})$ is the DM-nucleon reduced mass and $\lambda_L = (\lambda_3 + \lambda_4 + \lambda_5)$ is the quartic coupling involved in the DM-Higgs interaction. A recent estimate of the Higgs-nucleon coupling is $f = 0.32$ [125], although the full range of allowed values is $f = 0.26 - 0.63$ [126]. As shown in Fig. 4.2 later, the Xenon1T upper bound on the DM-nucleon scattering can put a stringent limit

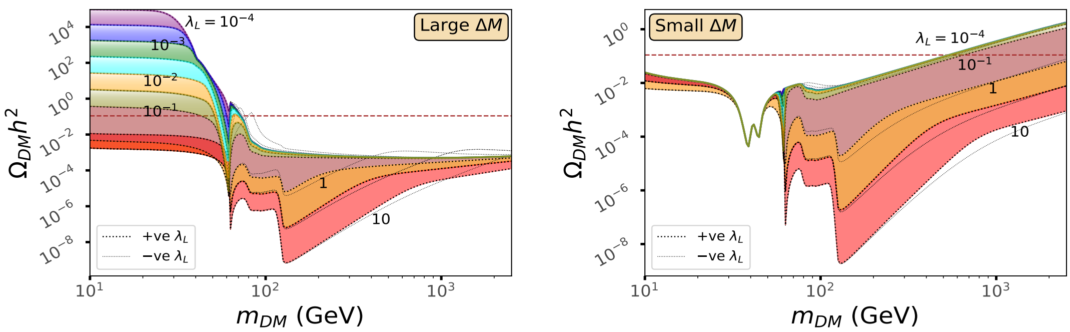

(a) (b)

Figure 4.1: Variation of relic density $\Omega_{DM}h^2$ shown as a function of dark matter mass m_{DM} in inert doublet model. Band of colours with thick dotted lines considering different λ_L values. Corresponding negative values of λ_L are shown with thin dotted lines. DM relic abundance strongly depends upon the mass difference ΔM between dark matter candidate from additional BSM scalar masses. Left and the right plots correspond to the large and small values of it, respectively. One can identify four DM paradigms inside the IDM parameter space, as discussed in Tab. 4.1.

on the allowed λ_L values that constrain the Higgs-DM coupling.

4.3 Possible searches and benchmarking

We explore the DM paradigm inside the IDM, discussing the variation of DM relic density with various model parameters. The relic density dependence on DM mass for both the hierarchical and degenerate nature of the BSM mass spectrum is presented in Fig. 4.1 for different λ_L values. The nature of the mass spectrum is quantified by two mass differences $\Delta M_1 \equiv m_{H^\pm} - m_{DM}$ and $\Delta M_2 \equiv m_A - m_{DM}$, which are assumed to be equal (ΔM) in the plots. Effects of the hierarchical mass spectrum with $\Delta M = 100$ GeV and the degenerate mass spectrum with $\Delta M = 1$ GeV on DM relic density are depicted in Fig. 4.1a and Fig. 4.1b, respectively. We also point out how sign-reversal of λ_L can alter the relic density dependence on the DM mass.

We roughly divide the DM paradigm of the IDM into four different cases depending on the DM mass and the nature of the mass spectrum, specified by $\Delta M_1, \Delta M_2$. These four cases are showcased in Tab. 4.1. In each scenario, we

ΔM \ M_{DM}	Small	Large
Small	$\boxed{\textbf{Case I}}$ M_{DM} < 80 GeV ΔM $\sim \mathcal{O}(1-10)$ GeV *Relic Density* $\sim 10\%$	$\boxed{\textbf{Case III}}$ M_{DM} ~ 550 GeV $\Delta M \sim \mathcal{O}(1)$ GeV *Relic Density* $\sim 100\%$
Large	$\boxed{\textbf{Case II}}$ M_{DM} < 80 GeV $\Delta M \sim \mathcal{O}(100)$ GeV *Relic Density* $\sim 100\%$	$\boxed{\textbf{Case IV}}$ M_{DM} ~ 550 GeV $\Delta M \sim \mathcal{O}(10-100)$ GeV *Relic Density* $\sim 1\%$

Table 4.1: Illustration of four DM paradigms inside the IDM parameter space, comparing DM mass as well as scalar mass hierarchy. Available DM density as a fraction of the required relic density is also pointed out for these cases. We study the phenomenologically interesting but challenging region marked by **Case II**.

discuss the thermal DM relic abundance along with the phenomenological study done to probe the BSM scalars.

Case I: We first consider a case of light DM with mass, $m_{\rm DM} \lesssim 80$ GeV together with all other heavy scalars within a narrow mass range. This case is severely constrained from the LEP data which rules out $m_{\rm DM} < 45$ GeV. Precise LEP measurements of the Z-width constrains $Z \to AH$ decay together with the conditions in Eq. 4.14. Even for the DM mass above 45 GeV, the degenerate nature of the spectrum ensures that all the inert scalars take part in the co-annihilation processes and reduce the relic density to somewhat below 10% of the total relic. Instead of both of the mass differences ΔM_i tiny, if one of them is taken to be large, only the scalar with smaller ΔM dominantly affect the extent of DM co-annihilation. Sharp dip appears when the DM mass is at $m_h/2$ due to the resonant production peak in the DM annihilation through the Higgs portal. Furthermore, some additional shallow dips in the relic density are also observed when the WW and the ZZ annihilation modes open up, enhancing the annihilation cross section. In this low mass region, the DM annihilation is contributed dominantly through the Higgs portal, and thus the sign of λ_L does not affect the relic density. This scenario is explored at the LHC in the mono-jet signal, as discussed in Ref. [127].

Case-II: Here, we consider the light DM with the hierarchical scalar mass spectrum, *i.e.* large mass differences (ΔM_i) with both of the other heavy scalars. Because of this large mass difference between H and $A/H^{\pm}$, the LEP Z-width measurements do not constrain such a low DM mass. DM annihilates only through the Higgs portal and therefore for tiny λ_L, the relic is overproduced. However, the entire relic density can be described at larger λ_L values, which are progressively bounded from the DM direct detection data from LUX and Xenon1T. Contrasting this with the degenerate case as pointed out in 'Case-I', here the co-annihilation effect is absent in the annihilation cross section and increases the relic density to produce a full relic in the range $m_{\rm DM} \sim 53 - 70$ GeV depending on different λ_L values. Phenomenologically this parameter range is quite interesting although detection of such very light DM along with much heavier other scalars is challenging at the collider. One has to encounter a very small production cross section along with an extremely large SM background where the signal characteristics are very background-like. The LHC potential of this case is studied in the dijet plus MET channel in Ref. [128]. Here, we take up this scenario for further analysis.

Case-III: If we move towards the heavier DM regime, a degenerate mass spectrum can provide full relic density at around $m_{\rm DM} \sim 550$ GeV [‡]. Exact mass depends strongly on the value of λ_L parameter. From a 10% relic for $m_{\rm DM} \sim 100$ GeV, it steadily increases as the $HH \to WW, ZZ$ annihilations open up and the cross section decreases with mass. The $HHVV$ coupling turns out to be $\lambda_{HHV_iV_i} \sim (4m_{\rm DM}\Delta M_i/v^2 + \lambda_L)$ in the limit DM and other heavy scalars are mass degenerate, *i.e.*, $\Delta M_1 \approx \Delta M_2 \to 0$. We explored this part of the parameter space earlier with both $\Delta M_i = 1$ GeV. Even if the DM annihilation rate increases with the DM mass, that increase is strongly suppressed due to tiny mass differences between the different BSM scalars in a nearly degenerate mass spectrum. The DM relic density, along with being inversely dependent on the annihilation cross section, also is directly proportional to the DM mass. Therefore, the interplay of these two competing effects finally ends up in a gradual increase in the DM relic density. The quartic coupling essentially depends only on λ_L in $\Delta M_i \to 0$, even then a λ_L sign reversal does not affect the DM pair annihilation. This scenario is phenomenologically interesting but quite challenging to probe at the LHC. This

[‡]Recently, this limit is brought down to the DM mass ~ 400 GeV, as shown in Ref. [129], by introducing right handed neutrinos, whose late decay to the DM compensates the underproduced DM relic density seen previously.

extremely compressed scenario can be probed at the LHC with identifying the charged track signal of a long-lived charged scalar [130].

Case-IV: In the heavier DM regime with hierarchical mass spectrum where both the mass differences are large, *e.g.*, $\Delta M_1 \approx \Delta M_2 \sim 100$ GeV, the annihilation cross section increases with the DM mass. This happens due to rapid increase of the DM-gauge boson quartic couplings with its mass, *i.e.*, $\lambda_{HHV_iV_i} = 2(2m_{\rm DM} + \Delta M_i)\Delta M_i/v^2 + \lambda_L$, for any general ΔM_i, which is a result of the large mass difference between the BSM scalars. Enhancement in the DM annihilation leads to drop of the relic density with increasing $m_{\rm DM}$ producing up to a few percents of the full observed value. Here, λ_L dependence is mostly overshadowed by large mass differences and does not affect much. In the case of very distinct choices of ΔM_i values, the DM annihilation would be dominated by the scalar having a larger mass difference through this enhanced coupling while the other one would contribute negligibly. Therefore the DM scenario in Case-III can be envisaged as a limiting case of Case-IV.

Among the four DM scenarios in the IDM as described above and also summarised in Tab. 4.1, two cases have emerged as phenomenologically exciting. Light DM ($m_{\rm DM} \sim 50 - 80$ GeV) with hierarchical mass spectrum with a substantial mass gap ($\Delta M_i \gtrsim 100$ GeV) with other heavy scalars can provide the full observed DM relic density. On the other side, we get a rather heavy DM ($m_{DM} \sim 550$ GeV) with an extremely degenerate mass spectrum, which can also provide the required relic density. Both the scenarios are challenging to probe, as the heavier BSM scalars are difficult to produce in the inert model and essentially confront with large irreducible SM backgrounds.

Now, we particularly focus on the low DM mass (50-70 GeV) with hierarchical mass spectrum *i.e.*, $\Delta M_1, \Delta M_2 \gtrsim 200$ GeV for our phenomenological study. To demonstrate the exact numerical evaluation, in Fig. 4.2, we explore the $m_{\rm DM} - \lambda_L$ parameter plane of the IDM for a light DM with $\Delta M_i = 100$ GeV applying the constraints from the DM relic density measurements, the DM direct detection experiments and the constraint from the Higgs invisible decay. This choice of 100 GeV is representative since major annihilation modes for DM are through the

Higgs portal and the parameter space of this plot is equally valid for larger ΔM choices. Blue (red) dots are the points where the observed DM relic abundance is exactly satisfied as in Eq. 4.16 for +ve (-ve) values of λ_L. The shaded area under this curve represents DM over-abundance and thus is excluded. Two other constraints can come from the invisible decay of the Higgs and the DM direct detection constraints from XENON1T, which are shown in the same plane in two other shaded regions in the upper portion of the plot, respectively. The DM direct detection constraints from LUX (Xenon1T) put stringent upper bound on λ_L, for all values of light DM. All other constraints described above, provide weaker bounds in this parameter space [131].

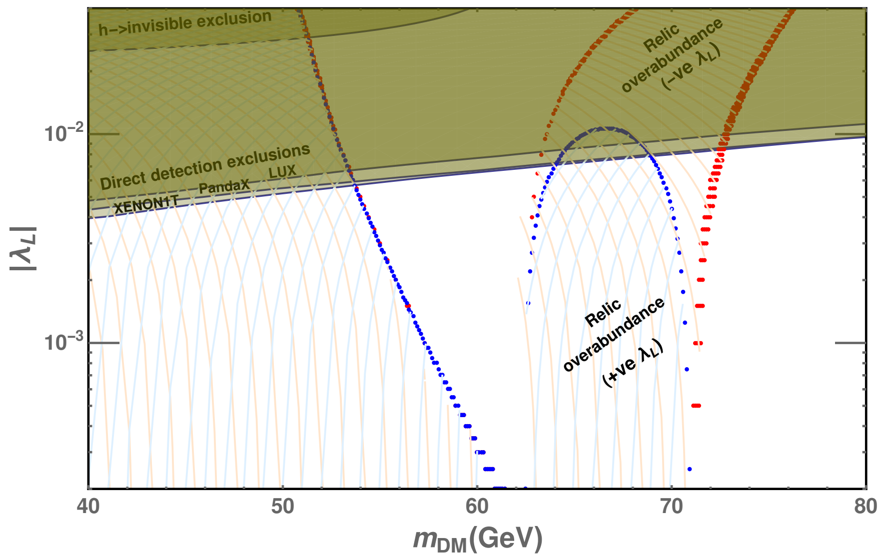

Figure 4.2: Allowed DM relic abundance in $m_{DM}-|\lambda_L|$ parameter space extracted for a set of $M_H^{\pm}, M_A$ and λ_2 values. Blue (red) dots are the points where observed abundance is exactly satisfied as in Eq. 4.16 for +ve (-ve) values of λ_L. The shaded area under this curve represents over-abundance and is thus excluded. Two other shaded regions at the upper portion of the plot are excluded from invisible decay of Higgs and DM direct detection constraints from XENON1T, Panda, and LUX, respectively.

With our understanding of allowed DM mass and λ_L parameter in the light DM scenario, we now attempt to comprehend other remaining parameters. To do so, we set these parameters to a particular choice from the allowed region of the relic density plot and then perform a scan over the remaining three parameters comprising of heavy scalar masses $(M_H^{\pm}, M_A)$ and λ_2. One such frame of the

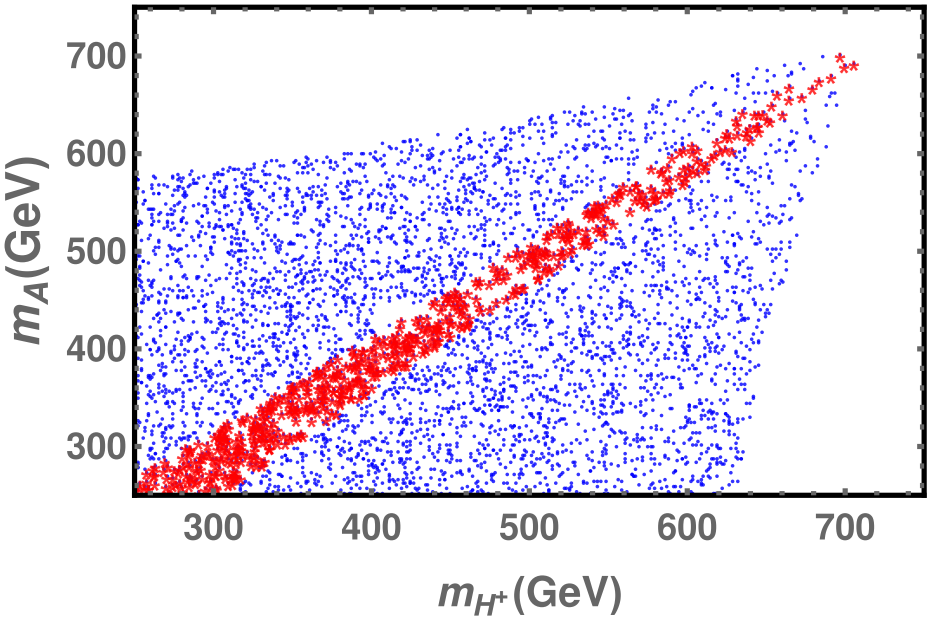

Figure 4.3: The blue scatter plot shows the limits from positivity and perturbativity constraints in the $(M_H^{\pm}, M_A)$ plane after fixing the DM mass and λ_L for all benchmark points. The red dots represent the allowed parameter space after imposing the constraints from the oblique parameters S, and T. Similar allowed parameter space is found for other benchmark points.

allowed parameter space after imposing the theoretical constraints (unitarity, perturbativity etc.) along with the $R_{\gamma\gamma}$ constraint from Secs. 4.2.1, 4.2.2 are shown by the blue scatter plots in Fig. 4.3. The red dots in the same plot represent the values of $M_H^{\pm}$ and M_A, which satisfy the oblique parameter constraints. These constraints, primarily through the T parameter, force these heavy scalar masses $M_H^{\pm}$ and M_A to be almost degenerate.

To study the specific low mass DM scenario within the IDM, we choose a set of seven benchmark points (BPs) from the allowed parameter space. These BPs covering heavy scalar mass between 250 to 550 GeV along with the corresponding input DM mass and λ parameter are summarised in Tab. 4.2. It is worth noting that the choice of M_H and λ_L is for the theoretical and experimental consistency, but the collider analysis proposed in this work holds equally good for all the allowed points in Fig. 4.2. Radiative correction to the DM-Higgs portal coupling is calculated in Ref. [132], which allows slightly more parameter space.

Parameters	BP1	BP2	BP3	BP4	BP5	BP6	BP7
$M_{H^\pm}$(GeV)	255.3	304.8	350.3	395.8	446.9	503.3	551.8
M_A(GeV)	253.9	302.9	347.4	395.1	442.4	500.7	549.63
λ_2	1.27	1.07	0.135	0.106	3.10	0.693	0.285

Table 4.2: Input parameters λ and the relevant scalar masses for some of the chosen benchmark points satisfying all the constraints coming from DM, Higgs, theoretical calculations and low energy experimental data as discussed in the text. All the mass parameters are written in units of GeV. Standard choice of the other two parameters are fixed at $M_H = 53.71$ GeV and $\lambda_L = 5.4 \times 10^{-3}$.

4.4 Collider analysis

We make use of various publicly available HEP packages for our subsequent collider study aiming for a consistent, reliable detector level analysis. We implement the IDM Lagrangian in `FeynRules` [133] to create the UFO [134] model files for the event generator `MadGraph5 (v2.5.5)` [72] which is used to generate all signal and background events. These events are generated at the leading order (LO) and the higher-order corrections are included by multiplying appropriate QCD K-factors. We use `CTEQ6L1` [135] parton distribution functions for event generation by setting default dynamical renormalization and factorization scales used in `MadGraph5` [136]. Events are passed through `Pythia8` [73] to perform showering and hadronization and matched up to two to four additional jets for different processes using `MLM` matching scheme [74, 75] with virtuality-ordered Pythia showers to remove the double counting of the matrix element partons with parton showers. The matching parameter, `QCUT` is appropriately determined for different processes as discussed in Ref. [137]. Detector effects are simulated using `Delphes` [77] with the default CMS card. Fatjets are reconstructed using the `FastJet` [31] package by clustering `Delphes` tower objects. We employ Cambridge-Achen (CA) [22] algorithm with radius parameter $R = 0.8$ for jet clustering. Each fat jet is required to have P_T at least 180 GeV. We use the adaptive Boosted Decision Tree (BDT) algorithm in the `TMVA` framework [36] for MVA.

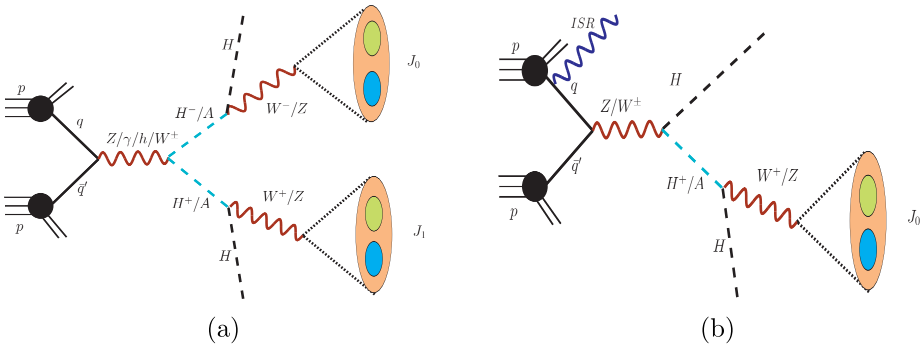

Figure 4.4: Representative parton level diagrams of (a) di-V-jet plus missing-energy ($2J_V + \not{E}_T$) and (b) mono-V-jet plus missing-energy ($1J_V + \not{E}_T$).

4.4.1 Signal topology

The hierarchical mass pattern in the IDM scalar sector, (*i.e.*, $M_A \sim M_{H^\pm} \gg M_H$) provides us with interesting final states. Once a pair of heavy scalars (or one heavy scalar associated with DM candidate) are produced at the LHC, they eventually decay dominantly producing two (or one) boosted vector bosons, each of which is decaying hadronically and thus producing V-jet (J_V) where $V = \{W, Z\}$. These boosted V-jets are always associated with large MET ($\not{E}_T$), an outcome of our inability to detect the DM pair at the detector. Representative Feynman diagrams of these signal topologies are demonstrated in Fig. 4.4. Among them, it must already be clear to the readers that the $1J_V + \not{E}_T$ channel alone, although being cross-section-wise bigger than $2J_V + \not{E}_T$, has less sensitivity at the LHC due to overwhelmingly large SM background. Therefore, we primarily focus on the $2J_V + \not{E}_T$ channel where the large background can be tamed down by employing jet substructure variables in an MVA framework. Our signal is not pure $1J_V + \not{E}_T$ or $2J_V + \not{E}_T$ topologies rather it is an admixture of both processes. Note that the baseline selections (defined in Sec. 4.5.2) are designed keeping $2J_V + \not{E}_T$ topology in mind. This keeps a large fraction of events from the $1J_V + \not{E}_T$ topology. In doing this we gain in the signal, but at the same time one can avoid extremely large background related to the $1J_V + \not{E}_T$ topology, (*i.e.*, by demanding at least one J_V instead of two). Before moving on to the actual analysis, we give some useful details about these two signal topologies.

<u>$2J_V + \not{E}_T$ channel:</u> This final state can arise in the IDM for the aforementioned benchmarks from the following three different channels, Here, A and $H^{\pm}$ decay to ZH and $W^{\pm}H$, respectively. As Z and W are originating from a heavy resonance, it is possible that they have sufficient boost to be reconstructed in a large radius jet. We do not distinguish a Z-jet or a W-jet and call them V-jet as we always select fat jets with a broad mass range. A V-jet possesses a two prong substructure, *i.e.*, energy distribution is centered around two subjet axes. We utilise the N-subjettiness ratio τ_{21} (defined later) to tag V-jets.

<u>$1J_V + \not{E}_T$ channel:</u> This final state can arise from the following two different channels, Extra jets can arise in the final state due to initial state radiation (ISR) and can form another fat jet. So these channels can potentially mimic the $2J_V + \not{E}_T$ final state. We generate matched samples of this signal with up to two additional jets in the final state. In this topology, only one of the two fat jets has the V-jet like structure and the other jet originates from the QCD radiation which mimics the fat jet characteristics. We find that the contributions to the $2J_V + \not{E}_T$ final state from the $1J_V + \not{E}_T$ topologies are quite significant and sometimes bigger than the $2J_V + \not{E}_T$ contribution itself after our final selection. This is mainly due to bigger production cross-sections of $pp \to AH, H^{\pm}H$ processes and the tail events which satisfy the fat jet criteria of our analysis [§].

The leading order production cross sections for the signal processes discussed above for different BPs are given in Tab. 4.3. We have used NLO QCD k-factors of 1.27 and 1.50 for the $q\bar{q}$ and the gg initiated productions for the signal [140].

4.4.2 Backgrounds

For our hybrid signal discussed in the introduction as well as in Sec. 4.4.1, major backgrounds come from the following SM processes which we discuss briefly below. All these backgrounds are carefully included in our analysis.

<u>$V + jets$:</u>

[§]The motivation to choose $2J_V + \not{E}_T$ channel is that one has larger features than in the case of $1J_V + \not{E}_T$ to handle the enormous background, where $1J_V + \not{E}_T$ also contributes to the signal $2J_V + \not{E}_T$ when the extra QCD jet mimics as a fat jet. The $1J_V + \not{E}_T$ is explored in the searches in Refs. [138, 139].

Benchmark Points	$\sigma(pp \to xy)$ (fb)				
	AH^0	$H^\pm H^0$	$AH^\pm$	H^+H^-	AA
BP1	34.54	62.53	12.62	7.96	0.50
BP2	18.71	34.12	6.22	4.23	0.40
BP3	11.43	20.84	3.50	2.59	0.34
BP4	7.11	13.32	2.05	1.70	0.28
BP5	4.63	8.44	1.22	1.13	0.24
BP6	2.84	5.32	0.71	0.76	0.19
BP7	1.95	3.70	0.45	0.56	0.16

Table 4.3: Production cross sections for the signal processes that contribute to the $1J_V + \not\!\!E_T$ and $2J_V + \not\!\!E_T$ final states at the 14 TeV LHC. These numbers are for $pp \to xy$ level before the decay of IDM scalars.

There are the following two types of mono-vector boson processes that contribute dominantly in the background.

- $\underline{Z + jets}$: This is the most dominant background in our case. We generate the event samples by simulating the inclusive $pp \to Z + jets \to \nu\nu + jets$ process matched up to four extra partons. Here, invisible decay of Z gives rise to a large amount of $\not\!\!E_T$ and QCD jets mimic as fat jets.

- $\underline{W + jets}$: This process also contributes significantly in the background when W decays leptonically, and the lepton does not satisfy the selection criteria. This is often known as the lost lepton background. The neutrino comes from the W-decay and contributes to missing energy and QCD jets mimic as fat jets. We generate the event samples by simulating inclusive $pp \to W + jets \to \ell_{(e,\mu)}\nu + jets$ process matched up to four extra partons.

In order to get statistically significant background events coming from the tail phase space region with large $\not\!\!E_T$, we apply a hard cut of $\not\!\!E_T > 100$ GeV at the generation level to generate these background events.

$\underline{VV + jets}$:

Different diboson processes like WZ, WW and ZZ also mimic the signal and contribute to the SM background. The $pp \to WZ$ process contributes most significantly among these three diboson channels when W decays hadronically, and Z decays invisibly. We call this background as W_hZ_ν. Similarly, W_hW_ℓ, where

Background process		σ (pb)
$V + jets$ [79, 141]	$Z + jets$	6.33×10^4 [NNLO]
	$W + jets$	1.95×10^5 [NLO]
$VV + jets$ [81]	$WW + jets$	124.31 [NLO]
	$WZ + jets$	51.82 [NLO]
	$ZZ + jets$	17.72 [NLO]
Single top [142]	tW	83.1 [N^{2}LO]
	tb	248.0 [N^{2}LO]
	tj	12.35 [N^{2}LO]
Top pair [83]	$tt + jets$	988.57 [N^{3}LO]

Table 4.4: Cross sections for the background processes considered in this analysis at the 14 TeV LHC. These numbers are shown with the QCD correction order provided in brackets.

one W decays hadronically and the other leptonically, and $Z_h Z_\ell$ (a hadronic Z and a leptonic Z) can also contribute to the SM backgrounds when leptons remain unidentified. All the diboson processes are generated up to two extra jets with `MLM` matching. In this case, one of the fat jets can come from the hadronic decay of V, and the other can come from the hard partons.

Single top:

Single top production in the SM includes three types of processes viz. top associated with W (*i*.e. $pp \to tW$ process), s-channel single top process (*i*.e., $pp \to tb$) and t-channel single top process (*i*.e., $pp \to tj$). Among these, the associated production tW contributes significantly in the SM background for our signal topologies.

$tt + jets$:

This can be a background for our signal topologies when it decays semileptonically, *i*.e., one of the top decays leptonically and the other decays hadronically. This background contains b-jets. We control this background by applying a b-veto. This background always has one V-jet. Another fat jet can originate from an untagged b-jet or QCD radiation.

Apart from the above background processes, we also calculate the contributions from triboson and QCD multijet processes. However, these contributions are found to be insignificant as compared to the background discussed above, and therefore, we neglect the contribution of these backgrounds in the analysis. The production cross-sections with higher order QCD corrections for all the background processes considered in this analysis at the 14 TeV LHC are listed in Tab. 5.4.

4.5 Cut-based analysis

We perform a CBA to estimate the sensitivity of observing the IDM signatures at the high luminosity LHC runs. It is evident that the signal cross sections are too small compared to the vast SM background. Therefore, one needs sophisticated kinematic observables for the isolation of signal events from the background events. Our signal processes always include at least a hadronically decaying vector boson that can provide a V-like fat jet. Therefore, we make use of the jet substructure variables for our purpose.

4.5.1 V-jet tagging: jet substructure observables

Jet substructure observables have emerged as a powerful technique to search for new physics signatures at colliders. In our case, boosted W and Z bosons, originated from the decay of heavy IDM scalars ($H^{\pm}$, A), give rise to collimated jets that can form a large radius jet (fat jet). These fat jets have two-prong substructures. We utilise two jet substructure observables viz. the jet-mass (M_J) and N-subjettiness ratio (τ_{21}). The M_J is a viable observable to classify the V-jets from the fat jets originated from QCD jets. We calculate the jet mass as $M_J = (\sum_{i \in J} P_i)^2$ where P_i are the four-vector of energy hits in the calorimeter. The discrimination power of M_J reduces if extra contribution comes from the parton, which does not actually originate from the V-decay. This results in broadening of the peak in the M_J distributions. Different jet grooming techniques are proposed to remove these softer and wide-angle radiations, such as trimming, pruning, and filtering [25–28]. We choose pruning for grooming the fat jets. In Fig. 4.5, we show the distributions for pruned jet mass for signal (BP3) and the important backgrounds. It is evident from these distributions that the peak around $80 - 90$ GeV reflect the V-mass peak for the signal whereas for most of the background processes the peaks below 20 GeV reflect the fat jets mimic from a single prong hard QCD jet. In Fig. 4.6, the distribution for the N-subjettiness ratio for signal BP3 and leading background are shown. The value for τ_{21} is small for fat jets emerging from the signal than the background. The N-subjettiness ratio τ_{21} is close to zero if correctly identify the N-prong structure of the jet. The detail detailed discussion of pruned jet mass and N-subjettiness is given in chapter 2.

4.5.2 Event selection

We list our baseline selection criteria to select events for further analysis.

Baseline selection criteria:

- Events are selected with missing transverse energy $\not{E}_T > 100$ GeV.
- We demand for at least two fat jets of radius parameter $R = 0.8$ constructed using the CA algorithm with fat jet transverse momentum $P_T(J) > 180$ GeV.
- We apply the following lepton veto, so that, events are rejected if they contain a lepton with transverse momentum $P_T(\ell) > 10$ GeV and pseudorapidity $|\eta(\ell)| < 2.4$.
- We further demand that the azimuthal separation $\Delta\phi$ between the fat jets and $\not{E}_T$, $|\Delta\phi(J, \not{E}_T)| > 0.2$. This minimises the effect of jet mismeasurement contributing to $\not{E}_T$.

After primary selection, we apply the following final selection criteria on events satisfying the baseline selection criteria for final analysis.

Final selection criteria:

- After optimization with signal and background, the minimum $\not{E}_T$ requirement is raised from 100 to 200 GeV.

- In order to reduce the huge background coming from the $tt+jets$, we apply a b-veto with p_T-dependent b-tagging efficiency as implemented in `Delphes`. Here, jets are formed using the anti-k_t algorithm with radius parameter $R = 0.5$.

- We demand that the pruned jet mass of leading and subleading fat jets should be in 65 GeV $< M_{J_i} <$ 105 GeV to tag J_V candidates.

- Further to discriminate the fat jet J_V from the QCD jets, we look for the two-prong nature of the fat jet using N-subjettiness and select the events with $\tau_{21}(J_i) < 0.35$ of the unpruned fat jet.

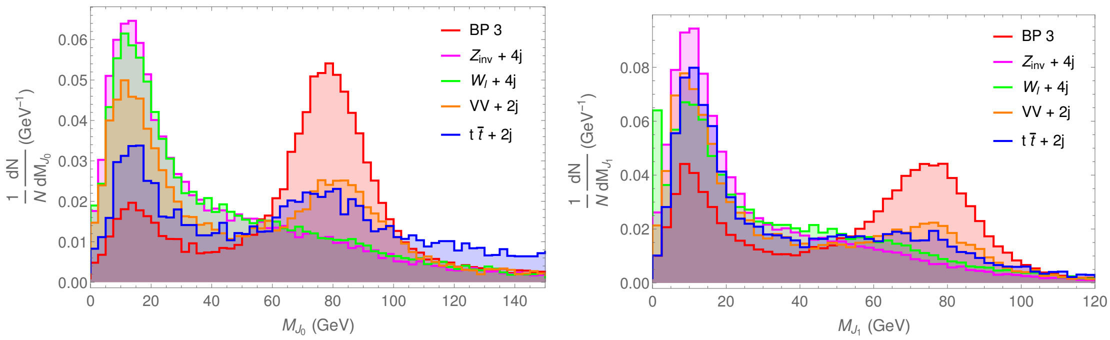

Figure 4.5: Normalised distributions for invariant mass of leading fat jet M_{J_0} (left) and and subleading fat jet M_{J_1} (right) after the *baseline selection cuts*.

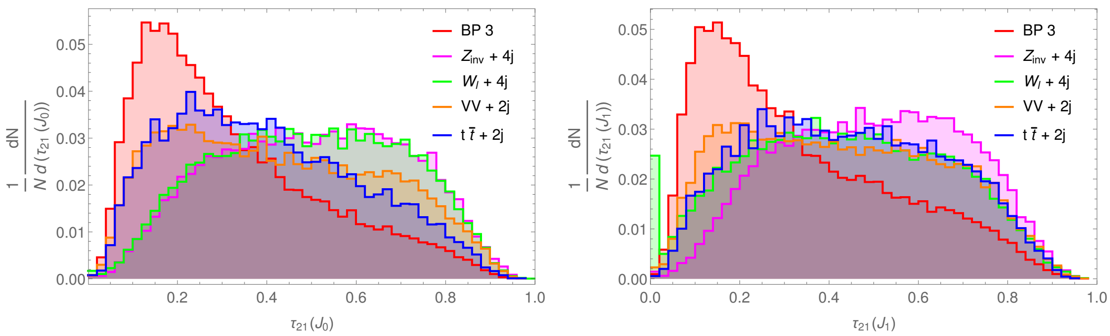

Figure 4.6: Normalised distributions for N-subjettiness of the leading fat jet $\tau_{21}(J_0)$ (left) and and subleading fat jet $\tau_{21}(J_1)$ (right) after the *baseline selection cuts*.

In Tab. 4.5, we present the cut-flow for the signal (BP3) associated with the cut efficiencies and the number of events for an integrated luminosity of 3000 fb^{-1} at the 14 TeV LHC. Similarly, Tab. 4.6 represents the cut-flow for the different

Cut	Signal **BP3**				
	AH^0	$H^{\pm}H^0$	$AH^{\pm}$	H^+H^-	AA
Baseline $+\not{E}_T > 200$ GeV	672.03 [100%]	1608.8 [100%]	711.62 [100%]	562.15 [100%]	64.5 [100%]
b-veto	474.24 [70.70%]	1291.74 [80.28%]	474.81 [66.66%]	426.85 [75.95%]	32.5 [50.49%]
65 GeV $< M(J_0), M(J_1) <$ 105 GeV	79.50 [11.83%]	274.17 [17.04%]	171.83 [24.12%]	137.56 [24.48%]	4.87 [18.13%]
$\tau_{21}(J_0), \tau_{21}(J_1) < 0.35$	52.44 [7.88%]	171.79 [10.67%]	128.40 [18.02%]	101.98 [18.13%]	3.5 [5.18%]

Table 4.5: After implementing the corresponding cut, the expected number of events and cut efficiency are shown for signal (BP3) for all possible channels which are contributing to the two $2J_V$ + MET final state,for an integrated luminosity of 3000 fb^{-1} at the 14 TeV LHC.

Cut	Background				
	$Z_\nu + jets$	$W_\ell + jets$	$VV + jets$	$Single - top$	$tt + jets$
Baseline $+\not{E}_T > 200$ GeV	3.22×10^6 [100%]	4.76×10^6 [100%]	1.47×10^5 [100%]	2.06×10^5 [100%]	3.81×10^5 [100%]
b-veto	2.69×10^6 [83.65%]	4.30×10^5 [9.22%]	1.13×10^5 [75.01%]	3.63×10^4 [16.90%]	4.60×10^4 [12.34%]
65 GeV $< M(J_0), M(J_1) <$ 105 GeV	3.80×10^4 [1.19%]	1.67×10^4 [0.35%]	4.09×10^3 [2.81%]	1.96×10^3 [0.72%]	1.66×10^3 [0.43%]
$\tau_{21}(J_0), \tau_{21}(J_1) < 0.35$	1.30×10^4 [0.41%]	3.79×10^3 [0.07%]	1.62×10^3 [1.03%]	1.44×10^3 [0.56%]	3.84×10^2 [0.10%]

Table 4.6: Cut flow for the SM backgrounds after corresponding cuts are implemented, for an integrated luminosity of 3000 fb^{-1} at the 14 TeV LHC.

backgrounds. From these numbers, it is explicit that the τ_{21} and M_J are powerful variables to have large background reduction with good signal acceptance. We can further infer from Tab. 4.5 that in spite of quite low efficiencies of AH and $H^{\pm}H$ channels to satisfy the $2J_V + \not{E}_T$ criteria, they give comparable contributions to the signal due to its large production cross section.

We compute the statistical signal significance using $\mathcal{S} = \mathcal{N}_S/\sqrt{\mathcal{N}_S + \mathcal{N}_B}$, where $\mathcal{N}_S$ and $\mathcal{N}_B$ represent the remaining number of signal and background events after implementing all the cuts. We show the statistical significance for different benchmark points in Tab. 4.7. The highest significance is found for BP3.

We would like to emphasise that even after utilizing the novel techniques of jet substructure this particular region of parameter space is very challenging to probe with high sensitivity at the HL-LHC. In order to optimise our search further, we use MVA with jet substructure variables.

Benchmarks	BP1	BP2	BP3	BP4	BP5	BP6	BP7
Significance	1.9	2.9	3.2	2.9	1.9	1.6	1.1

Table 4.7: Statistical significance of the signal for different benchmark points in di-fat jet + $\not{E}_T$ analysis for an integrated luminosity of 3000 fb^{-1} at the 14 TeV LHC.

4.6 Multivariate analysis

In the previous section, we present the reach of our model using a CBA. Although we have not achieved discovery significance of 5σ in any of our benchmark points, we see that the two variables viz. M_J and τ_{21} are very powerful to separate the tiny signal from the large SM background. In this section, we use a sophisticated MVA to achieve better sensitivity than a CBA. We would like to discuss two important points here. First, we have observed that MVA does not perform well if we use events selected just with the baseline cuts since the signal is too tiny compared to the overwhelmingly large background. Therefore, we need to apply, in addition to the baseline selection cuts, the following strong cut on the hardest fat jet mass, $M_{J_0} > 40$ GeV and b-veto on jets to further trim down the large background before passing events to MVA. These cuts are very effective to drastically reduce the background but not the signal and are optimally chosen such that it is not too close or too relaxed compared to the cuts used in CBA. If the extra strong cuts for MVA are too close to the cuts applied for the CBA, MVA will not give us an improved sensitivity. On the other hand, if they are too relaxed, the performance of MVA will degrade as the background will become too large. Although we select events with two high-p_T fat jets, we only demand the jet mass of the leading-p_T fat jet is greater than 40 GeV. This will pass a large fraction of mono-fat jet signal events along with the di-fat jet. Therefore, on the one hand, this will increase the signal. However, on the other hand, this will also increase the background.

Topology	BP1	BP2	BP3	BP4	BP5	BP6	BP7
$1J_V$	1668	2025	2023	1472	1334	1190	920
$2J_V$	601	1112	1572	1254	979	948	608
Z	W	t	tt	WZ	ZZ	WW	Total
3.15×10^6	1.43×10^6	1.6×10^5	1.6×10^5	1.76×10^5	2.97×10^4	1.21×10^4	5.1×10^6

Table 4.8: Number of signal and background events at the 14 TeV LHC with 3000 fb^{-1} integrated luminosity. These numbers are obtained by applying $M_{J_0} > 40$ GeV and b - jet veto in addition to the baseline cuts defined in the text.

In Tab. 4.8, we show the number of signal ($1J_V$ and $2J_V$ categories) and background events at the 14 TeV LHC with 3000 fb^{-1} integrated luminosity. Observe that although we demand two fat jets in our selection, the number of $1J_V$ events that contribute to the signal are always bigger than the $2J_V$ contributions for all BPs. This is due to the fact that cross sections for $1J_V$ topologies are much bigger than the $2J_V$ topologies and also a significant fraction of $1J_V$ events pass the selection cuts. Therefore, it is necessary to design hybrid selection cuts, stricter than $1J_V$ but looser than $2J_V$, where both $1J_V$ and $2J_V$ topologies contribute. Our selection cuts are, therefore, optimally designed to achieve better sensitivity.

For our MVA, we use the adaptive BDT algorithm. We obtain two statistically independent event samples for the signal as well as for the background and split the dataset randomly 50% for testing and the rest for training purposes for both the signal and background. Note that there are multiple processes that are contributing to the signal and similarly for the background. In MVA, we construct the signal classes by combining both the $1J_V$ and $2J_V$ topologies that pass our MVA selection criteria. These different signal samples are separately generated at LO and then mixed according to their proper weights to obtain the kinematical distributions for the combined signal. Similarly, all different background samples are mixed to obtain similar distributions for the background class.

The final set of variables that are used in the MVA are decided from a larger set of kinematic variables by looking at their power of discrimination between signal and background classes. Four substructure variables for two fat jets, *i*.e., $M_{J_{0,1}}$ and $\tau_{21}(J_{0,1})$ has already proved to be very important discriminators in our CBA. Stronger transverse momenta cut for such jets are favorable to retain the correct classification of these variables. We already required reasonably high P_T criteria for both such jets. However, to construct the hybrid selection cuts $P_T(J_0)$ can still take a role in determining the purity of the hardest fat jet J_0. We also include relative separation between these fat jets $\Delta R(J_0, J_1)$ and the azimuthal angle separation between the leading fat jet from the missing transverse momentum direction $\Delta\phi(J_0, \not{E}_T)$. The scale of new physics is relatively high, and that is typically captured by some of the topology independent inclusive variables like H_T, $\not{H}_T$, $\not{E}_T$ etc. We utilise the global inclusive variable $\sqrt{\hat{S}_{min}}$ proposed to determine the mass scale of new physics for events with invisible particles such as ours [92, 143, 144]. This variable, constructed out of all reconstructed objects at the detector, demonstrates better efficiency compared to other inclusive counterparts. For example, we did not use $\not{E}_T$ as a feature after baseline cut since it showed a high correlation with $\sqrt{\hat{S}_{min}}$ and turned out to be less important than it.

In Fig. 4.7, we show the normalised distributions of all eight input variables used in the MVA. Signal distributions are obtained for BP3 including $1J_V$ and $2J_V$ topologies and the background includes all the dominant backgrounds discussed in Sec. 5.3.2 for the 14 TeV LHC. For the same benchmark scenario, method unspecific relative importance of all the kinematic variables are available during TMVA analysis and presented in Fig. 4.8. Moreover, we mostly keep variables which are less correlated (or anti-correlated) for both the signal and the background. Relative importance is a measure that is used to rank the variables in MVA. In other words, a variable has better discriminatory power if it has greater relative importance. For this particular benchmark point, BP3, $M_{J_{0,1}}$ variables are very good discriminators according to their relative importance. The N-subjettiness variables, $\tau_{21}(J_{0,1})$, are also very good discriminators as expected. Note that, the relative importance can change for different benchmark points or different LHC energies etc., that can change the shapes of the variables. The linear correlation matrices for the signal and the background can be seen in Fig. 4.9. Observe that M_{J_1} and $\tau_{21}(J_1)$ variables are strongly anti-correlated. The correlation in the M_{J_1}

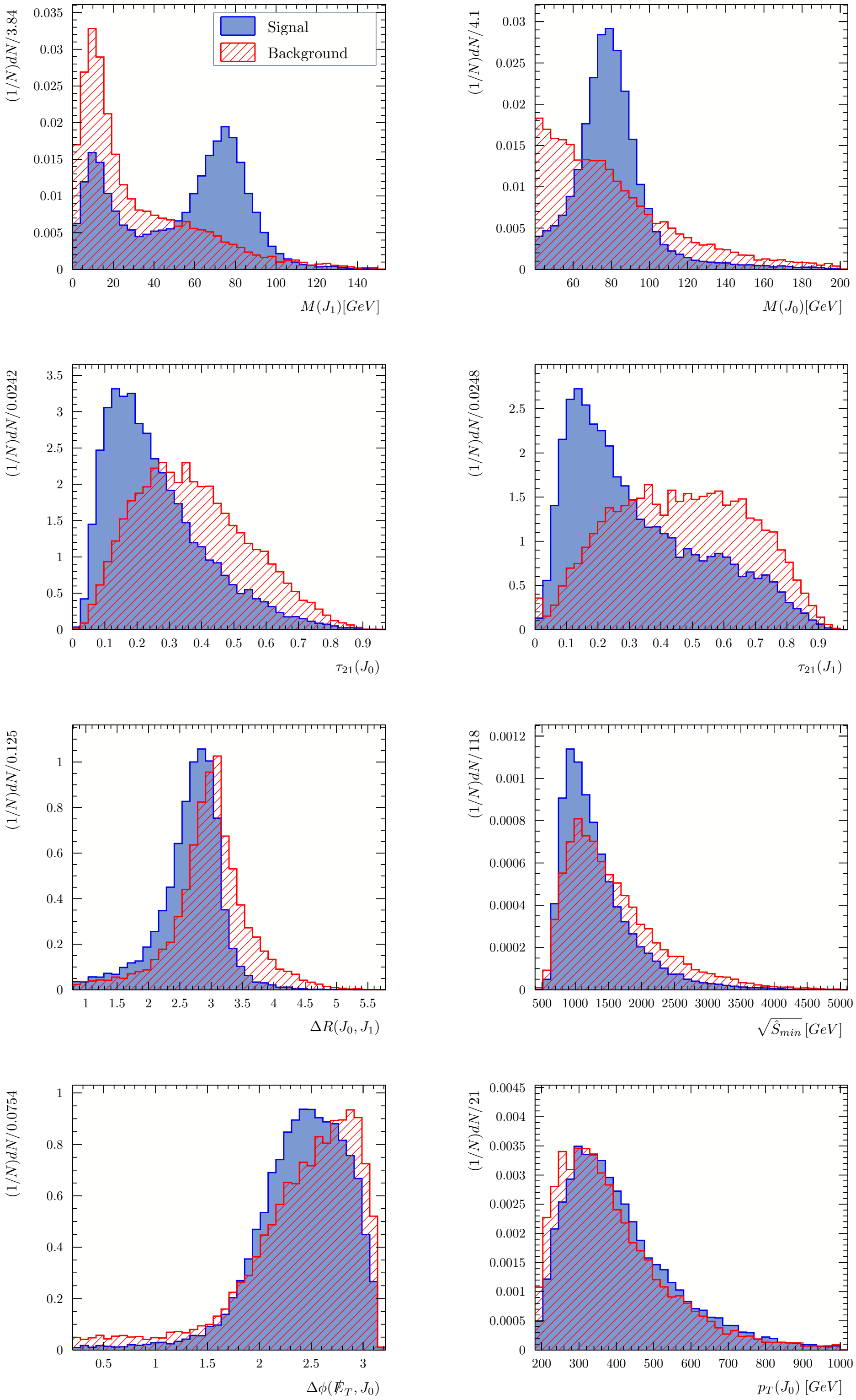

Figure 4.7: Normalised distributions of the input variables at the LHC ($\sqrt{s} = 14$ TeV) used in the MVA for the signal (blue) and the background (red). Signal distributions are obtained for BP3 including $1J_V$ and $2J_V$ topologies and the background includes all the dominant backgrounds discussed in Sec. 5.3.2.

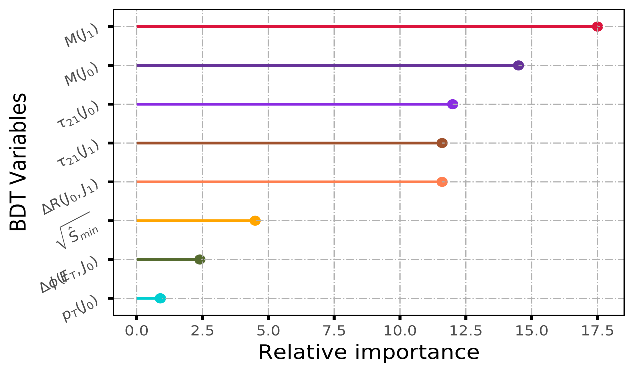

Figure 4.8: Kinematic variables used for our MVA and their relative importance. We obtain these numbers from the TMVA package for the benchmark point BP3. Here, we show method unspecific relative importance. This can change slightly for different algorithms and their tuning parameters.

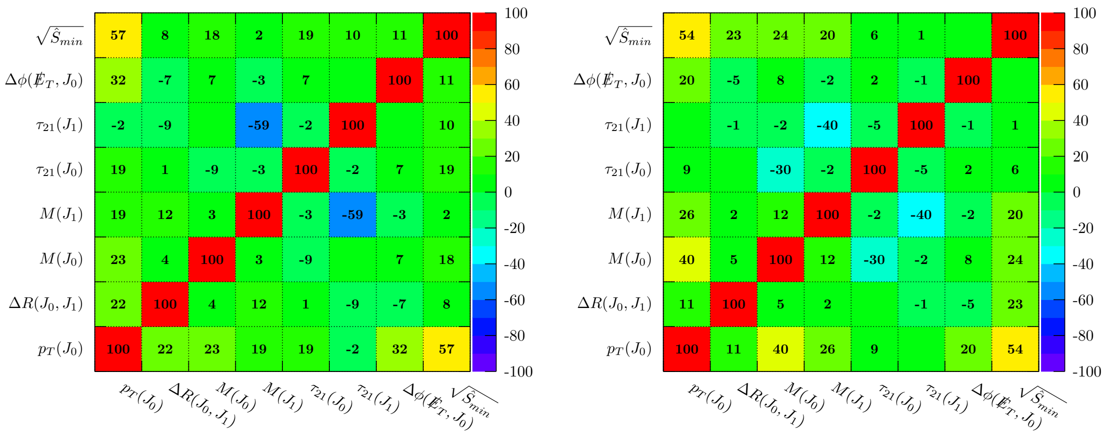

Figure 4.9: The linear correlation coefficients (in %) for signal (left panel) and background (right panel) among different kinematical variables that are used for the MVA for BP3. Positive and negative signs of the coefficients signify that the two variables are positively correlated and negatively correlated (anti-correlated).

and $\tau_{21}(J_1)$ variable is due to a mixture of $1J_V$ and $2J_V$ topology in the signal. However, we keep both of them in the MVA since both of them are very powerful discriminators for $2J_V$ topology.

Since the BDT algorithm is prone to overtraining, one should be careful while using it. This usually happens during the training of the algorithm due to inappropriate choices of the BDT specific parameters. One can avoid overtraining by checking the Kolmogorov-Smirnov probability during training. We train the algorithm for every benchmark point separately and ensure that the algorithm

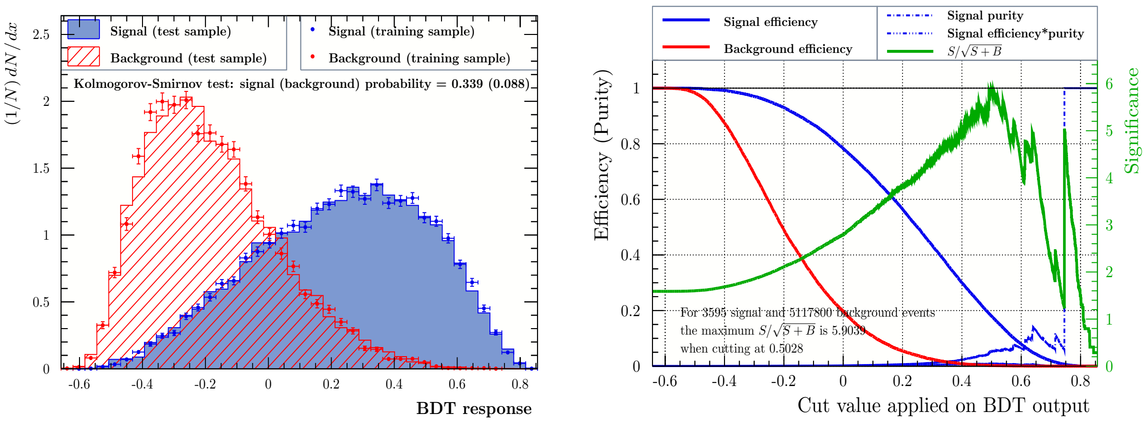

Figure 4.10: (Left panel) Normalised BDT response distributions for the signal and the background for BP3. (Right panel) Cut efficiencies as functions of BDT cut values.

is not overtrained in our analysis. Note that the set of eight variables that are used in our analysis may not be the optimal ones. There is always the scope of improving the analysis by choosing a cleverer set of variables. But since the variables we use in MVA are very good discriminators, our obtained sensitivities are fairly robust.

In Fig. 4.10, we show the normalised BDT response for the signal and the background (training and test samples for both the classes) for BP3. One can clearly see that the BDT responses for the signal and background classes are well separated. We apply a cut on the BDT responses *i.e.*, $\text{BDT}_{res} > \text{BDT}_{cut}$ and show the corresponding cut efficiencies for the signal (blue) and the background (red) and the significance (green) as functions of BDT_{cut}. The significance is computed using the formula $\sigma = \mathcal{N}_S/\sqrt{\mathcal{N}_S + \mathcal{N}_B}$ where $\mathcal{N}_S$ and $\mathcal{N}_B$ are the signal and background events that are survived after the $\text{BDT}_{res} > \text{BDT}_{cut}$ cut for a given integrated luminosity. The optimal BDT cut, BDT_{opt} is the cut for which the significance is maximised. In Tab. 5.6 we show $\mathcal{N}_S$, $\mathcal{N}_B$ and σ for different BPs for the 14 TeV LHC, considering an integrated luminosity of 3000 fb^{-1}. We also demonstrate this significance as a function of $M_{H^\pm,A}$ in Fig. 4.11 (red curve), whereas the blue curve represents the required luminosity for the 2 σ exclusion of different BPs.

BP	$\mathcal{N}_S^{bc}$	BDT$_{opt}$	$\mathcal{N}_S$	$\mathcal{N}_B$	$\mathcal{N}_S/\sqrt{\mathcal{N}_S+\mathcal{N}_B}$
1	2269	0.45	412	10748	3.9
2	3137	0.42	596	14200	4.9
3	3595	0.50	635	10957	5.9
4	2726	0.52	504	11514	4.6
5	2313	0.51	404	8880	4.2
6	2138	0.58	385	9871	3.8
7	1528	0.55	278	6823	3.3
$\mathcal{N}_{\rm SM}$	5117800	-	-	-	-

Table 4.9: Total number of signal events are $\mathcal{N}_S^{bc}$ (including $1J_V$ and $2J_V$ topologies as shown in Tab. 4.8) and with number of background events $\mathcal{N}_{\rm SM}$ before BDT$_{opt}$ cut. The number of signal and background events after the BDT$_{opt}$ cut are denoted by $\mathcal{N}_S$ and $\mathcal{N}_B$ respectively.

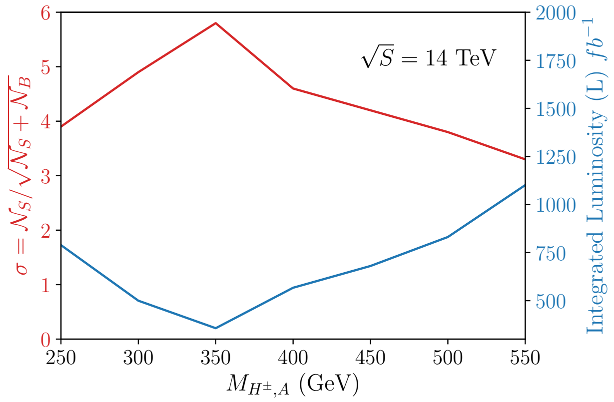

Figure 4.11: Significance as a function of heavy scalar mass $M_{H^\pm}$ at the 14 TeV LHC with 3000 fb^{-1} integrated luminosity. We also present required luminosity for the exclusion (2 σ) of different benchmark points based on this heavy scalar mass.

4.7 Summary and Conclusion

The IDM is a simple theoretical framework with rich phenomenology providing possible DM candidates. We classify the model space in four categories depending on the masses of the scalars in the model as summarised in Tab. 4.1. Some of them are quite interesting in view of the observed properties of the Z-boson, Higgs and DM, together with fulfilling all the available theoretical constraints and from the low energy experiments. All such constraints on the IDM are critically analyzed to establish that a hierarchical BSM spectrum with a light DM ($m_{\rm DM} \lesssim 80$ GeV) provides an appealing scenario, as it fulfills the full observed relic density. Furthermore, additional constraints from the Higgs invisible decay and the DM direct detection limits leave us with little allowed parameter space left to be explored at the LHC, albeit a rather difficult region to explore.

Exploiting the fact that after production, the heavy BSM scaler essentially decays into boosted vector bosons together with light DM candidates, we propose a search strategy of a scenario consisting of two boosted fat jets with large MET. Hadronic decay from such boosted vector bosons carries distinctive substructures characteristically different from the single prong large radius QCD jets and can be distinguished with moderate efficiencies using jet substructure observables.

It turns out that our signal of boosted $2J_V + \not{E}_T$ also gets significant contributions from single heavy scalar productions with light DM, where the other second J_V is mimicked by a QCD jet, especially since the later production is roughly one order of magnitude higher than the two J_V processes. Essentially the di-fat jet signal, after our selection cuts, turns out to be a hybrid of di-J_V and mono-J_V signals. The corresponding background to the mono-J_V channel is also very large, which contributes to the overall background. The $V + jets$ SM processes are the dominant backgrounds to the above signal, and the sheer magnitudes of these backgrounds of order ~ 1000 pb make it very difficult to search for the BSM scalars of the IDM in any channel. We use intuitive application of jet substructure variables like the fat jet mass (M_J) and the N-subjettiness (τ_{21}) which encode the internal structure of the fat jets.

Even with these variables, it is extremely difficult to overcome the huge background and therefore, the best case cut-based analysis discovery potential remains restricted to less than 3 σ. While cuts on these variables, as detailed in Tab. 4.5 and 4.6, can bring down the background to less than the 1% level from the generated ones simultaneously bringing down the signal numbers to $10\% - 20\%$. In the end, we do not obtain any significant improvement in the discovery potential to make it cross the desired 5σ barrier for discovery. The best LHC sensitivity is obtained for the BP3 with $m_{H^\pm} \approx m_A \sim 350$ GeV and significance decreases both sides of the spectrum. With the increase of $m_{H^\pm}, m_A$, we get a higher boost for the decaying vector bosons, resulting in better discrimination power of the jet substructure variables. On the other hand, the presence of heavier particles leads to the suppressed signal cross section. Therefore, the best signal to background sensitivity is obtained only in an intermediate mass range.

To improve the LHC discovery potential, an MVA is undertaken where we employ a total eight kinematic variables which try to devise a boosted decision tree and provide the optimum separation between signal and background. Instead of the rectangular cuts used in CBA, MVA can use the full potential of jet substructure variables to study the full hierarchical parameter space of the IDM which is allowed after imposing all the theoretical and experimental constraints. The LHC sensitivity is improved to 5.6 σ for BP3 using MVA. Hence, much of the parameter space in a well motivated scenario within the IDM framework which provides a hierarchical BSM spectrum with light DM ($m_{\rm DM} \lesssim 80$ GeV), along with an almost degenerate heavy charged Higgs and a pseudoscalar A within the mass range between 250 - 550 GeV, can be excluded with 1100 fb^{-1} integrated luminosity at the 14 TeV LHC.

Chapter 5

Examining Compressed SUSY

Supersymmetry (SUSY) has been one of the front-runner candidates for beyond standard model (BSM) physics for the last few decades, and its search at experiments provides common ground to many non-SUSY searches too. In view of the null results at the run 1 and run 2 of LHC, compressed SUSY (cSUSY) has gained relevance in its ongoing pursuit, primarily aimed at looking at the elusive scenario of new physics with a significantly degenerate mass spectra. In non-minimal scenarios, the SUSY signals maybe substantially modified in the presence of alternative candidates for LSP and provide valuable probes of detection for the MSSM sector. In such cases, the SUSY signal is characterised by the presence of hard objects and large $\not{E}_T$ in the final state. Typical compressed spectra are not restricted to cSUSY scenarios only and also show up in a variety of other new physics scenarios such as extra-dimensions as well as in extended gauge sectors demanding further phenomenological studies in this context.

In this chapter, we focus on compressed SUSY scenarios with a higgsino-like $\widetilde{\chi}_1^0$ as the next-to-lightest sparticle (NLSP) and a light keV-scale gravitino ($\widetilde{G}$) as the LSP and potential dark matter (DM) candidate [145]. The rest of the spectrum, comprising of the strong and electroweak sparticles, are compressed in mass with respect to the NLSP and/or the LSP. In this case, a dominantly higgsino-like $\widetilde{\chi}_1^0$ NLSP decays to a Higgs boson or a Z boson along with the $\widetilde{G}$. Therefore the final states arising from the decay of the heavy sparticles lead to multifarious diboson (hh, ZZ, Zh) signals with large $\not{E}_T$.

This chapter is organised as follows: in Sec. 5.1 we discuss the relevant decays of the higgsino-like $\widetilde{\chi}_1^0$ NLSP. In Sec. 5.2, the current experimental constraints from LHC on the current scenario are discussed and some representative benchmark points satisfying current experimental limits are chosen. The detailed signal and background analysis for the two boosted fat jets and missing energy is performed and results are presented in Sec. 5.3. New kinematic observables to distinguish between compressed and uncompressed spectra are discussed in Sec. 5.4. Sec. 5.5 summarises and concludes the work.

5.1 Decay properties of a higgsino-like NLSP

Our focus is on a compressed MSSM sector with the higgsino-like $\widetilde{\chi}_1^0$ as the NLSP along with a light $\widetilde{G}$ LSP. For more details we refer the readers to reference [146, 147]. Here we only revisit the relevant decays of the NLSP and the current experimental constraints from LHC that dictate our choice of benchmark points.

The branching ratios of the $\widetilde{\chi}_1^0$ decay are governed by its composition and therefore on the value of the parameters M_1, M_2, μ and $\tan\beta$ [147–151]. For a gaugino-like $\widetilde{\chi}_1^0$ NLSP, the obvious decay modes to the $Z\widetilde{G}$ and $\gamma\widetilde{G}$ are open whereas for the higgsino-like case, its decay to the Higgs mode ($h\widetilde{G}$) also opens up. Note that for the higgsino-like case there is a huge suppression in branching probability to $\gamma\widetilde{G}$ mode. Thus the relevant partial decay widths of the lightest neutralino in the decoupling limit ($\mu << M_1, M_2$) are [148–150]:

$$\Gamma(\widetilde{\chi}_1^0 \to h\widetilde{G}) \propto |N_{14}\cos\beta + N_{13}\sin\beta|^2\,(M_{Pl}m_{\widetilde{G}})^{-2}$$
$$\Gamma(\widetilde{\chi}_1^0 \to Z\widetilde{G}) \propto (|N_{11}\sin\theta_W - N_{12}\cos\theta_W|^2 + \frac{1}{2}|N_{14}\cos\beta - N_{13}\sin\beta|^2)\,(M_{Pl}m_{\widetilde{G}})^{-2}$$

where N_{ij} refer to the elements of the neutralino mixing matrix. The terms proportional to N_{14} and N_{13} denote the Goldstone couplings to h/Z and $\widetilde{G}$ whereas θ_W denotes the Weinberg angle and $\tan\beta = v_u/v_d$ is the ratio of the *vev's* v_u and v_d of the two Higgs doublets, H_u and H_d, respectively.

In Fig. 5.1 we plot the variation of the branching ratios of $\widetilde{\chi}_1^0$ into a Higgs or Z as a function of (μ/M_1). Corresponding fixed values of M_1, M_2 and other

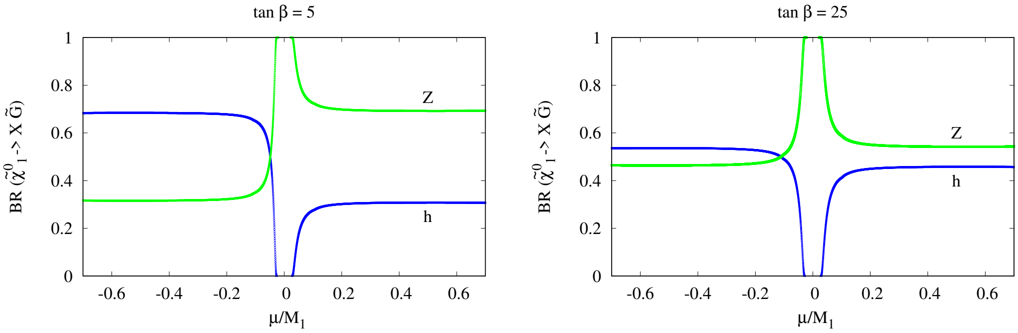

Figure 5.1: Variation of the branching ratios of the $\widetilde{\chi}^0_1$ NLSP producing the Higgs (blue dots) or Z boson (green dots) as a function of ratio $\frac{\mu}{M_1}$ for fixed values of M_1, M_2. All parameters are shown in Tab. 5.1. Two plots are for $\tan\beta = 5$ and 25 respectively.

Parameters	$\lvert\mu\rvert$ (TeV)	sign(μ)	$\tan\beta$
Values	0.2-2.8	±1	5,25

Table 5.1: Relevant range of the input parameters for the parameter-space scan to study the decay probabilities of the lightest neutralino. Other parameters at fixed values which include: $M_1 = 4$ TeV, $M_2 = 4$ TeV, $M_3 = 2.9$ TeV, $M_{Q_3} = 2.8$ TeV, $M_{U_3} = 2.8$ TeV, $M_A = 3.0$ TeV, $A_t = 3.2$ TeV and $m_{\widetilde{G}} = 1$ keV.

parameters are listed in Tab. 5.1 where μ is the higgsino mass parameter, while M_1 and M_2 are the bino and wino soft mass parameters respectively. The plots are shown for two values of $\tan\beta = 5, 25$. We have used `SPheno-v3.3.6` [152,153] to scan the parameter space.

We observe a gradual increase of the branching into the Higgs with increasing ratio (μ/M_1) due to an increase in the higgsino fraction of the NLSP. The general features of the plots are summarised below:

- For positive (μ/M_1), the branching ratios to the $Z\widetilde{G}$ and $h\widetilde{G}$ modes are comparable except in the low $\tan\beta$ regime where the former dominates.
- For negative (μ/M_1), the $h\widetilde{G}$ decay is greater than $Z\widetilde{G}$ decay, primarily in the low $\tan\beta$ regime.

This motivates choice of regions in the parameter space where either decay mode or both have branching fractions which are substantial in order to explore the multifarious signal possibilites. Accordingly, we choose the representative benchmarks after briefly summarising the relevant experimental constraints in the following section.

5.2 Benchmarks

Final state	Production channels	ATLAS	CMS
$2/3/4b + \not{E}_T$	$\widetilde{\chi}_1^0\widetilde{\chi}_1^\pm, \widetilde{\chi}_2^0\widetilde{\chi}_1^\pm, \widetilde{\chi}_1^+\widetilde{\chi}_1^-, \widetilde{\chi}_1^0\widetilde{\chi}_2^0$	[154]	[155]
$\ell^+\ell^- + \not{E}_T$	$\widetilde{\chi}_1^0\widetilde{\chi}_1^\pm, \widetilde{\chi}_2^0\widetilde{\chi}_1^\pm, \widetilde{\chi}_1^+\widetilde{\chi}_1^-, \widetilde{\chi}_1^0\widetilde{\chi}_2^0$		[155]
$\geq 3\ell + \not{E}_T$	$\widetilde{\chi}_1^0\widetilde{\chi}_1^\pm, \widetilde{\chi}_2^0\widetilde{\chi}_1^\pm, \widetilde{\chi}_1^+\widetilde{\chi}_1^-, \widetilde{\chi}_1^0\widetilde{\chi}_2^0$		[155]
$hh + \not{E}_T$	$\widetilde{g}\widetilde{g}$		[156]
$4\ell + \not{E}_T$	$\widetilde{\chi}_1^+\widetilde{\chi}_1^-, \widetilde{\chi}_1^\pm\widetilde{\chi}_2^0$	[157]	
$\geq 2j + \not{E}_T$	$\widetilde{g}\widetilde{g}, \widetilde{q}\widetilde{q}$	[158]	[159]
$b\bar{b} + \not{E}_T$	$\widetilde{\chi}_2^0\widetilde{\chi}_1^\pm$	[160]	
$3\ell + \not{E}_T$	$\widetilde{\chi}_2^0\widetilde{\chi}_1^\pm$	[160]	
$\ell^\pm\ell^\pm + \not{E}_T$	$\widetilde{\chi}_2^0\widetilde{\chi}_1^\pm$	[160]	
$2b + 1\ell + \not{E}_T$	$\widetilde{\chi}_1^\pm\widetilde{\chi}_2^0$	[161]	

Table 5.2: List of the experimental searches from LHC for higgsinos as relevant for our current study with $\widetilde{G}$ LSP.

Before moving on to choose relevant benchmarks for our current study, we list the currently available constraints from LHC in Tab. 5.2. The current exclusion limits on a light higgsino NLSP and gravitino LSP scenario follow:

- Stringent limits from ATLAS which arise from searches involving multiple b-jets along with missing transverse energy ($\not{E}_T$) excluding $m_{\widetilde{\chi}_1^0} < 380$ GeV for equal branching of the $\widetilde{\chi}_1^0$ into $h\,\widetilde{G}$ and $Z\,\widetilde{G}$ boson. For an increased branching fraction into the Higgs(100%), the mass limits strengthen considerably excluding $m_{\widetilde{\chi}_1^0} < 890$ GeV [162].

- The CMS Collaboration also sets complementary limits summarised in references [155, 163, 164]. Searches involving multiple b-jets and $\not{E}_T$ [164] rule out $m_{\widetilde{\chi}_1^0} < 500$ GeV for 60% decay of $\widetilde{\chi}_1^0$ into $h\,\widetilde{G}$. A combination of searches involving the hadronic search as well as multiple leptons and diphotons constrain $m_{\widetilde{\chi}_1^0}$ up to 700 GeV for equal branching of $\widetilde{\chi}_1^0$ into h and Z along with a $\widetilde{G}$ [155]. The exclusion limit improves slightly for the full decay of the $\widetilde{\chi}_1^0$ to the Higgs or Z ($m_{\widetilde{\chi}_1^0} < 750$ GeV).

Stongly interacting sparticles are also strongly constrained from LHC searches. A recent study performed using boosted jet techniques in reference [156] excludes gluino masses up to 1.8 (2.2) TeV for neutralino LSP mass up to 600 GeV (for $\widetilde{\chi}_1^0$ decaying into Higgs and/or Z boson).

We choose benchmark points representative of the parameter space allowed by the LHC for a light higgsino-like NLSP scenario with a keV $\widetilde{G}$ LSP. Our focus is on cSUSY scenarios as considered in previous studies [146, 165] with the lightest higgsino-like $\widetilde{\chi}_1^0$ as the NLSP. One also has to accommodate constraints from the observation of a light Higgs in the mass range 122-128 GeV, constraints from LEP on the sparticles (primarily the lightest chargino) as well as constraints from flavour physics. The details of such contraints are shown in reference [165] for the kind of compressed spectra we are interested in. The presence of the $\widetilde{G}$ relaxes the dark matter (DM) constraints on the MSSM part of the spectrum with a keV $\widetilde{G}$ DM candidate constituting a warm dark matter candidate [166–170]. We use `SPheno-v3.3.6` [152, 153] to obtain the benchmarks for the current study. We ensure that the benchmarks chosen pass all the relevant experimental searches from run 1 and run 2 at the LHC implemented in `CheckMATE` [171].

Keeping the above constraints in mind, the strongly interacting sector, namely the first and second generation squarks and gluinos, are kept in the mass range 2.4-3 TeV with varying orders of mass hierarchy amongst them. The third generation squarks are kept heavier than or equal to the first and second generation squarks by choice. In this work we focus on the hadronic signals and choose to keep the electroweak sector heavier than the strong sector. We also focus on a few non-compressed cases to compare the results of our search strategies. Note that our choice of benchmarks are representative of the parameter space involved. The NLSP decaying to the LSP leads to the presence of either Higgs and/or Z bosons in the final state. Thus the expected final states are $hh + \not{E}_T$, $hZ + \not{E}_T$ and $ZZ + \not{E}_T$, with the light gravitino LSP contributing to the missing transverse energy ($\not{E}_T$). The presence of a very light gravitino ensures that the decay products of the NLSP carry high transverse momentum and hence, a large missing energy in the signal as well. The use of jet substructure techniques will thus be very useful to study the boosted h/Z boson in the final states in order to uncover compressed spectra as studied in this work. We discuss the analysis techniques and results in Sec. 5.3.

Parameters	BP1	BP2	BP3	BP4	BP5	BP6	U1	U2
M_1	2900	3000	3000	3000	3500	3500	2900	2900
μ	2340	-2442	2505	2600	2812	2910	2390	1000
$\tan\beta$	25	25	5	25	25	25	25	25
A_t	-3200	-3200	-3300	-3200	-3200	-3200	-3200	-3200
m_A	2500	3000	2500	2500	3000	3000	3000	2500
m_h	124.7	124.6	122.1	124.8	124.6	124.6	124.7	124.7
$m_{\widetilde{g}}$	2395.1	2494.6	2609.0	2600.9	2999.6	2953.3	3031.7	3031.7
$m_{\widetilde{q}_L}$	2399.1	2500.9	2603.5	2667.7	2983.4	2961.7	2402.1	2402.2
$m_{\widetilde{q}_R}$	2398.0	2496.7	2599.3	2666.4	2980.0	2960.6	2397.8	2395.7
$m_{\widetilde{t}_1}$	2598.5	2612.5	2638.7	2612.5	2893.2	2929.7	2606.4	2587.7
$m_{\widetilde{t}_2}$	2787.5	2789.8	2845.9	2800.2	3056.0	3096.5	2784.7	2768.2
$m_{\widetilde{b}_1}$	2716.1	2704.9	2734.9	2726.6	2949.2	2985.6	2689.2	2690.5
$m_{\widetilde{b}_2}$	2781.3	2790.7	2789.5	2792.3	3010.1	3047.4	2784.7	2722.9
$m_{\widetilde{l}_L}$	3338.3	3339.1	3339.6	3339.1	3344.7	3345.1	3338.1	3338.1
$m_{\widetilde{l}_R}$	3338.5	3338.8	3338.9	3338.8	3341.3	3341.5	3338.4	3338.5
$m_{\widetilde{\chi}_1^0}$	2339.5	2399.9	2498.1	2591.0	2809.9	2905.1	1014.2	2387.3
$m_{\widetilde{\chi}_2^0}$	-2348.7	-2408.6	-2510.8	-2603.4	-2817.7	-2914.0	-1018.1	-2397.4
$m_{\widetilde{\chi}_1^\pm}$	2342.7	2402.9	2502.2	2595.1	2812.7	2908.2	1015.9	2390.8
$m_{\widetilde{\chi}_2^\pm}$	2898.6	2997.3	2997.8	3004.1	3485.6	3486.7	2896.2	2897.8
$m_{\widetilde{\chi}_3^0}$	2872.5	2972.0	2971.6	2974.4	3463.0	3462.0	2872.5	2872.6
$m_{\widetilde{\chi}_4^0}$	2899.0	2997.7	2998.7	3004.8	3485.9	3487.1	2896.2	2897.8
ΔM	59.6	101.0	110.9	76.7	189.7	56.6	2017.5	644.4
$BR(\widetilde{\chi}_1^0 \to Z\widetilde{G})$	0.55	0.55	0.71	0.56	0.55	0.55	0.56	0.55
$BR(\widetilde{\chi}_1^0 \to h\widetilde{G})$	0.45	0.45	0.29	0.44	0.45	0.45	0.44	0.45

Table 5.3: List of benchmark points, corresponding parameters and NLSP branching ratios chosen for our study. The mass parameters are in GeV unless specified otherwise. For all benchmarks, gravitino mass is kept fixed at $m_{\widetilde{G}} = 1$ keV.

We now discuss the salient features of our benchmark points (BP) as listed in Tab. 5.3. We construct two sets of them as below. While **BP1-BP6** represent a compressed spectra with narrow mass difference, $\Delta M < 200$ GeV, **U1-U2** are for uncompressed spectra having similar yields.

- **BP1-BP6**: These represent cSUSY spectra where one has comparable branching ratio of the $\widetilde{\chi}_1^0 \to h\widetilde{G}$ and $\widetilde{\chi}_1^0 \to Z\widetilde{G}$ decay modes. The compression parameter (ΔM) which is defined as the difference between the mass of the heaviest colored sparticle (i.e, gluinos or the first and second generation squarks) and the NLSP, varies in the range $\Delta M \simeq 56-190$ GeV while $m_{\widetilde{\chi}_1^0} \simeq 2.34-2.91$ TeV.

- **U1-U2**: These represent two uncompressed spectra with a lighter NLSP ($m_{\widetilde{\chi}_1^0} \simeq 1.01, 2.39$ TeV) with $\Delta M \simeq 2.02, 0.64$ TeV respectively.

The different benchmarks involving the compressed spectra vary from one another in the level of mass compression as well as the hierarchical arrangements of the first and second generation squarks and gluinos. For example, **BP1**–**BP3**, **BP5** and **BP6** have a compressed band involving the strong sector sparticles within 5 - 10 GeV while **BP4** accommodates the case where there is a larger mass gap ($\simeq 67$ GeV) between the squarks and gluinos. This allows the presence of additional light jets in the latter case as compared to the former ones.

5.3 Collider Analysis

5.3.1 Signal topology

In this study, the lightest neutralino has significant higgsino component which opens up new interesting but challenging channels to study. With the above choice, we can have three interesting final states ($\tilde{\chi}_1^0\tilde{\chi}_1^0 \to hh\tilde{G}\tilde{G}$, $\tilde{\chi}_1^0\tilde{\chi}_1^0 \to ZZ\tilde{G}\tilde{G}$, $\tilde{\chi}_1^0\tilde{\chi}_1^0 \to hZ\tilde{G}\tilde{G}$). It is governed by the benchmarks from Tab. 5.3 that the Higgs and the Z boson will be highly boosted and the total hadronic activity of the decay of h/Z can be captured in a large radius jet (fat jet of radius R), which will be directed by the relation

$$R \sim \frac{2M^{h/Z}}{P_T^{h/Z}}. \tag{5.1}$$

As shown in Tab. 5.3 the mass of neutralino ($\widetilde{\chi}_1^0$) lies in the range of 2-3 TeV. In this case, the Higgs tagger based on b-tagging techniques deteriorates its efficiency [172]. In this process, we also lose a sufficient number of events when ($\widetilde{\chi}_1^0$) is decaying to Z boson. To overcome this issue we propose to capture the Higgs and Z candidate using 2-prong finder tagger which is based on the radiation pattern inside the fat jet. We utilise the jet substructure techniques to identify h/Z candidate by looking for the following signal topology

$$PP \to 2 \texttt{ CA8 } \text{Fat-jets } (J) + \text{large } \not{E}_T,$$

where `CA8` represents the jets clustered with Cambridge-Aachen algorithm with R = 0.8. Later we utilise the 2-prong finder like N-subjettiness and energy correlation function (ECF) to tag the Higgs or Z like fat jets.

5.3.2 Backgrounds

The major contribution to the background comes from the following standard model processes. Corresponding cross sections as used in present analysis are listed in Tab. 5.4 with the order of QCD corrections.

- $Z \to \nu\bar{\nu}$ +jets turns out to be the most dominating background due to large missing transverse momentum and high fake rate of QCD fat jets as h/Z jets.

- $W \to l\nu$ +jets contributes to the SM background processes when the lepton is misidentified. Then the dynamics are the same as Z+jets. Due to the large cross-section, these processes contribute significantly.

- $VV{+}jets$: Diboson production in three different channels, such as, $W_hW_l, W_hZ_{\nu\bar{\nu}}$, and $Z_lZ_{\nu\bar{\nu}}$. Here the V_h, V_l and $V_{\nu\bar{\nu}}$ denotes the hadronic, leptonic and invisible decay modes respectively of W/Z bosons. Although, diboson process possess similar kinematics as the signal topology but contribute as subdominant background due to relative small cross section than the mono-V +jets channel.

- $Single{-}top$ production: Among the three different productions of the single top (tW, tj and tb) the main contribution comes from single top associated with W boson.

- $t\bar{t}$ decaying semi-leptonically gives rise to missing transverse energy when the lepton is misidentified. The possible source for fat jets is either one of the W decaying hadronically or mistagged b-jets.

Background process	Cross section (pb)
Z + jets [N^2LO]	6.33×10^4 [79, 141]
W + jets [NLO]	1.95×10^5 [72]
$Single - top$ (tW, tj and tb) [N^2LO]	83.1 , 12.35, 248.0 [142]
$Diboson(ZZ, WW, ZW)$ + jets [NLO]	17.72, 124.31, 51.82 [81]
$t\bar{t}$ + jets [N^3LO]	988.57 [83]

Table 5.4: The cross sections for the background processes used in this analysis are shown with the order of QCD corrections provided in brackets.

We additionally compute the contributions from the triboson and QCD multijet background which is rendered negligible because of high $\not{E}_T$ and two hard fat jet criteria.

5.3.3 Simulated events and Data sample

We have generated the cSUSY mass spectrum using `SPheno-v3.3.6`. All the events are generated using `Madgraph5 (v2.6.5)` [72] at leading order (LO) followed by `Pythia` (v8) [73] for showering and hadronization. To incorporate detector effects events are passed through `Delphes-v3.4.1` [77] using the default CMS card. Delphes tower are used as an input for fat jet clustering. Fat-jet are reconstructed using the Cambridge-Aachen algorithm [22] with radius parameter $R = 0.8$, as implemented in the `Fastjet`-v3.3.2 [31]. The minimum p_T for fat jet is required to be 300 GeV. We use `Root` [173] for the baseline event selection. The final multivariate analysis (MVA) is performed using Boosted Decision Tree (BDT), as implemented in toolkit for Multivariate Analysis `TMVA` [36]. The events used in the multivariate analysis are selected after the following baseline cuts which are designed for the signal topology discussed in Sec. 5.3.1.

Baseline selection criteria -

- We veto the events if any lepton with $p_T > 10$ GeV lies in the central psuedorapidity range $|\eta| < 2.4$.
- We select the events with at least two Cambridge-Aachen fat jets of radius parameter = 0.8 and with minimum transverse momentum $p_T = 300$ GeV.

- To overcome the effect of jet mismeasurement contributing to missing transverse energy both the fat jet should satisfy the criteria of $|\Delta\phi(J, \not{E}_T)| > 0.2$.
- The signal has large missing energy hence we select the events with $\not{E}_T$ greater than 100 GeV.

5.3.4 Multivariate analysis

We perform the collider study using a multivariate analysis (MVA) employing the Boosted Decision Tree (BDT) algorithm. The multivariate analysis outperforms the cut-based analysis since a cut-based analysis can select only one hypercube as the signal region of phase space, whereas, the decision tree can split the phase space into a large number of hypercubes. Each of these hypercubes is then identified as either a 'signal-like' or a 'background-like' tree. Then a non-linear boundary is created in hyperspaces to segregate the signal and background.

We use the following thirteen observables as input to BDT network. The normalised distributions of these input variables are shown in Fig. 5.2, Fig. 5.3, where the number on Y-axis represents the bin size.

- Transverse momentum of leading fat jet $P_T(J_0)$, Fig. 5.2a.
- Transverse momentum of sub-leading fat jet $P_T(J_1)$, similar figure not shown.
- The angular distance difference between two fat jets $\Delta R(J_0, J_1)$, Fig. 5.2b
- The missing transverse energy $\not{E}_T$, Fig. 5.2c
- The azimuthal angle difference between missing transverse energy and leading fat jet $\Delta\phi(J_0, \not{E}_T)$, Fig. 5.2d
- The azimuthal angle difference between missing transverse energy and subleading fat jet $\Delta\phi(J_1, \not{E}_T)$, Fig. 5.2e
- The effective mass of the process $M_{eff} = \sum_{vis} |P_T| + |\not{E}_T|$, shown in Fig. 5.2f

- The mass of leading fat jet M_{J_0} and sub-leading fat jet M_{J_1} are shown in Fig. 5.3a and Fig. 5.3b, respectively. We used the pruned jet mass by applying the pruning method described in references [26, 27] to clean the softer and wide-angle emission. We first calculate $z = min(P_{Ti}, P_{Tj})/P_{T_{i+j}}$ and the angular separation ΔR_{ij} between two proto-jets i and j at each step of recombination. Now, the softer proto-jet is discarded if $z < z_{cut}$ and $\Delta R_{ij} > R_{fact}$ and i-th and j-th proto-jets are not recombined. Otherwise, i-th and j-th proto-jets are recombined, and the procedure is repeated unless we remove all the softer and wide-angle proto-jet from the fat jet. We have used a fixed $R_{fact} = 0.5$ and $z_{cut} = 0.1$ as suggested in reference [26].

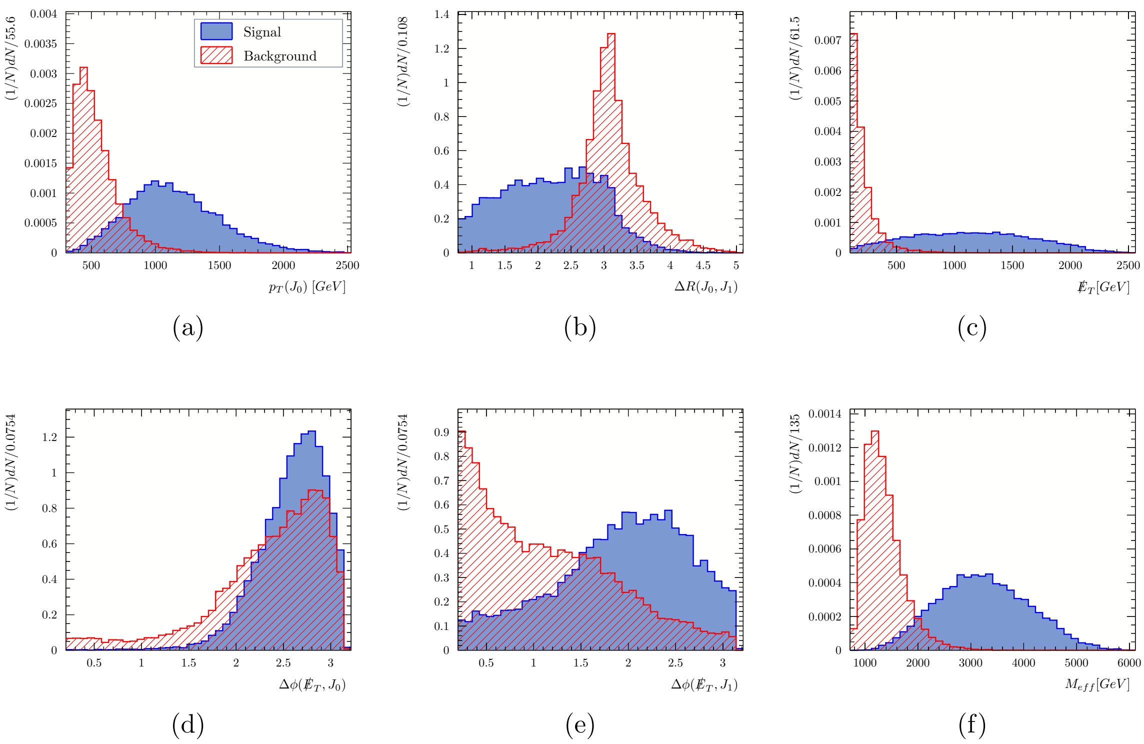

Figure 5.2: Normalised distributions of the basic input variables related to two reconstructed fat jets J_i and missing transverse energy $\not{E}_T$ at the LHC ($\sqrt{s} = 14$ TeV) used in the MVA for the signal (blue) and the background (red). Signal distributions are obtained for benchmark point **BP1** and the background includes all the dominant backgrounds.

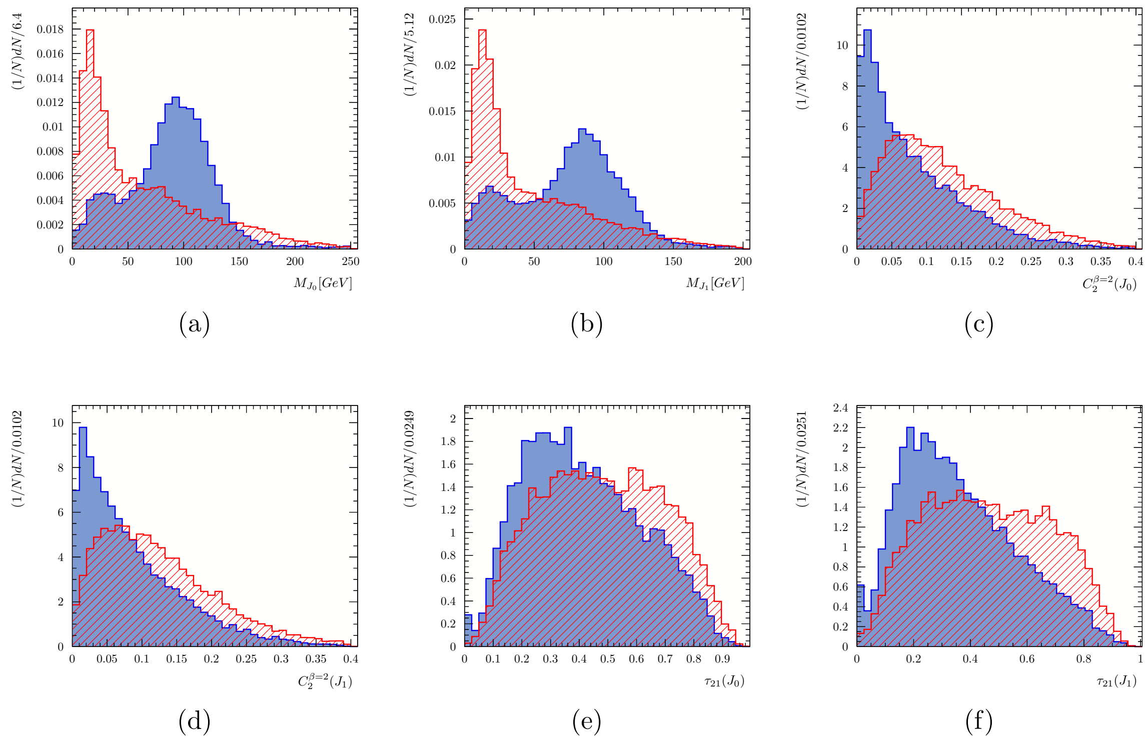

Figure 5.3: Normalised distributions of the additional input high level variables constructed for the fat jets at the LHC ($\sqrt{s}$ = 14 TeV) used in the MVA for the signal (blue) and the background (red). Signal distributions are obtained for benchmark point **BP1** and the background includes all the dominant backgrounds.

- We use 2-prong discriminant energy correlation functions [32]

$$C_2^{(\beta)} = \frac{e_3^{(\beta)}}{(e_2^{(\beta)})^2} \tag{5.2}$$

  where, $e_2^{(\beta)} = \sum_{1 \leq i < j \leq n_J} z_i z_j \theta_{ij}^{\beta}$ and $e_3^{(\beta)} = \sum_{1 \leq i < j < k \leq n_J} z_i z_j z_k \theta_{ij}^{\beta} \theta_{ik}^{\beta} \theta_{jk}^{\beta}$ are 2-point and 3-point energy correlation functions respectively. The β represents the exponent. Here z is the energy fraction variable, and θ is angular variable. The distributions of C_2 for leading and sub-leading fat jets are shown in Fig. 5.3c and 5.3d respectively.

- To reveal the two-prong nature of the fat jet, we also use the N-subjettiness ratio [29, 30]

$$\tau_N^{(\beta)} = \frac{1}{\mathcal{N}_0} \sum_i p_{i,T} \min\left\{\Delta R_{i1}^{\beta}, \Delta R_{i2}^{\beta}, \cdots, \Delta R_{iN}^{\beta}\right\} \tag{5.3}$$

where, $\mathcal{N}_0 = \sum_i p_{i,T} R_0$ is the normalizing factor, R_0 is the radius parameter of the fat jet, N is the axis of the subjet assumed within the fat jet and i runs over the constituents of the fat jet. We take the thrust parameter $\beta = 2$ which gives more weightage to the angular separation of the constituents from the subjet axis. The distributions of N-subjettiness for leading and sub-leading fat jets are shown in Fig. 5.3e and 5.3f.

Linear correlation among the variables plays a crucial rule to determine the information carried by the variable is unique or not. Most of the variables used in this study are highly uncorrelated with each other as shown in Fig. 5.4. Here positive and negative signs of the coefficients signify correlation and anti-correlation with the other variable. Some sets of variable like $\{P_T(J_0),\ P_T(J_1),\ M_{eff}\}$ and $\{\Delta\Phi(\not{E}_T, J_0),\ \Delta\Phi(\not{E}_T, J_1)\}$ show slightly high correlation for signal but have mild correlation in the background. This is mainly because of different kinematics of signal and background process.

We further show the method unspecific ranking (relative importance) for each observable according to their separation in Fig. 5.5. The separation in terms of an observable λ is defined as [36]

$$\Delta_{(\lambda)} = \int \frac{(\hat{y}_s(\lambda) - \hat{y}_b(\lambda))^2}{\hat{y}_s(\lambda) + \hat{y}_b(\lambda)} d\lambda. \tag{5.4}$$

where $\hat{y}_s$ and $\hat{y}_b$ are the probability distribution functions for signal and background for a given observable λ respectively. We have discussed this in detail in Chapter 2.

After calculating the importance of variables, we divide the data set in two equal parts. One part of the data sample is used to train the BDT algorithm and the other part is used for the validation. The parameters used to train the BDT algorithm are shown in Tab. 5.5 below:

Results from BDT analysis considering one sample benchmark point (BP1) is

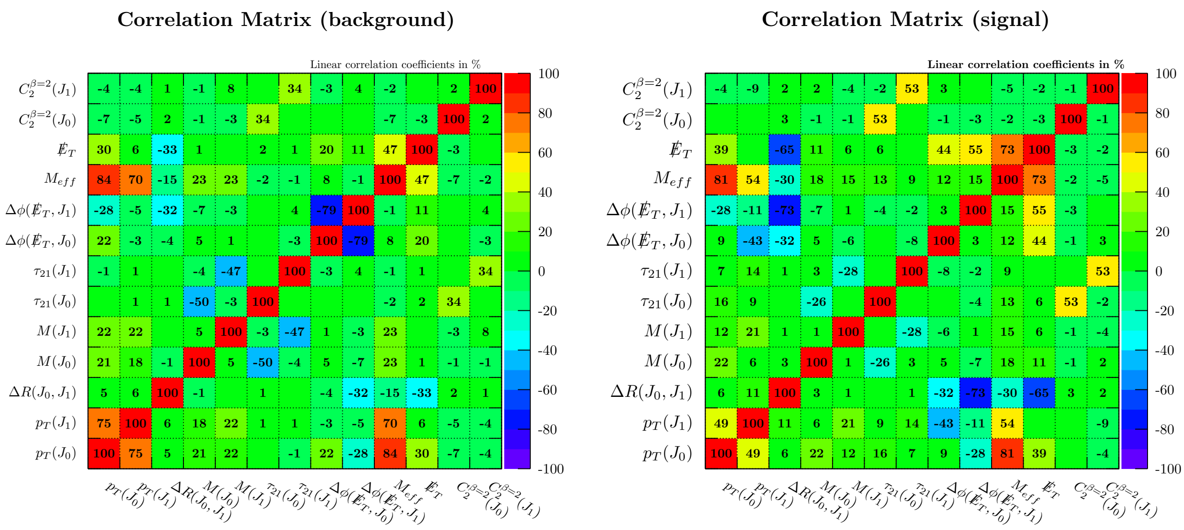

(a) (b)

Figure 5.4: The linear correlations coefficients (in %) for (a) signal and (b) background among different kinematical variables that are used for the MVA for benchmark point **BP1**. Positive and negative signs of the coefficients signify that the two variables are positively correlated and negatively correlated (anti-correlated).

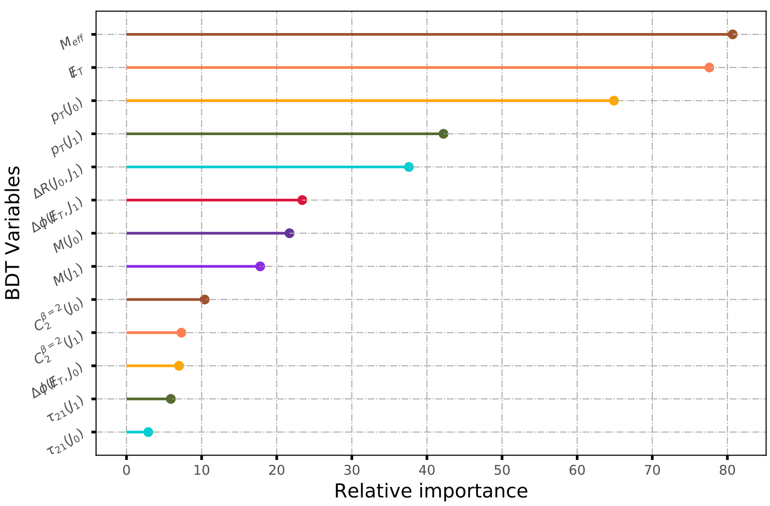

Figure 5.5: Kinematic variables used for our MVA and their relative importance. We obtain these using numbers from the TMVA package for the benchmark point. Here, we show method unspecific relative importance.

demonstrated in Fig. 5.6. Kolmogorov-Smirnov probability for training and testing sample are shown to confirm that the network is not overtrained. The testing data fit well to the training data and the validation is shown in Fig. 5.6a. The BDT is trained for each benchmark point separately. We apply the cut on BDT

NTrees	400	Number of trees in the forest
MaxDepth	2	Max depth of the decision tree allowed
MinNodeSize	5.6%	Minimum % of training events required in a leaf node
BoostType	AdaBoost	Boosting type for the trees in the forest
AdaBoostBeta	0.5	Learning rate for AdaBoost algorithm
nCuts	20	Number of grid points in variable range used in finding optimal cut in node splitting

Table 5.5: Parameter used in BDT architecture

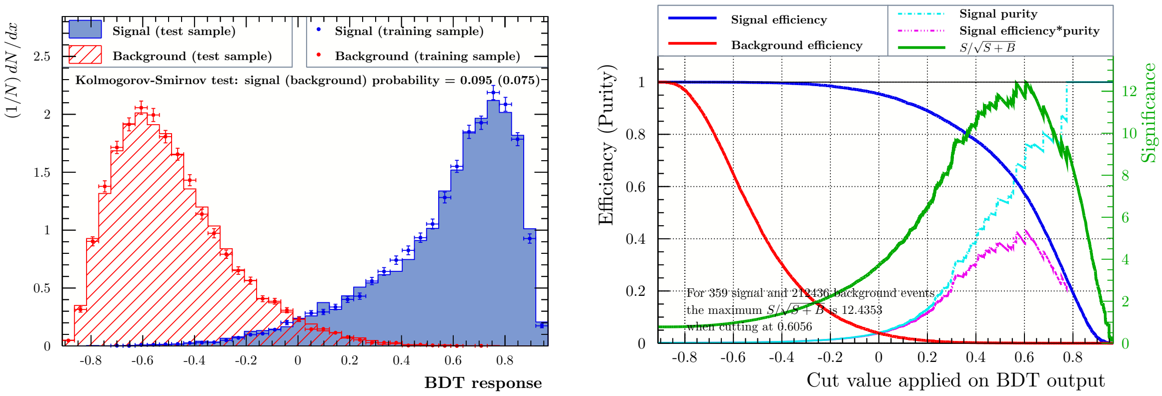

(a) (b)

Figure 5.6: (a) Normalised BDT response distributions for the signal and the background for the benchmark point **BP1**. (b) Cut efficiencies as functions of BDT cut values. All plots are evaluated for for benchmark point **BP1** using integrated luminosity of 200 fb^{-1} at the 14 TeV LHC.

response and obtain the corresponding number of signal $\mathcal{N}_S$ and background $\mathcal{N}_B$. Finally we calculate the statistical significance using formula $\sigma = \mathcal{N}_S/\sqrt{\mathcal{N}_S + \mathcal{N}_B}$. The cut value of BDT response is BDT$_{opt}$, where the maximum significance is achieved. These steps were depicted in second plot for the sample benchmark point, as shown in Fig. 5.6b. Finally, the results for all benchmark points are displayed in Tab. 5.6.

BPs	$\mathcal{N}_S^{bc}$	BDT$_{opt}$	$\mathcal{N}_S$	$\mathcal{N}_B$	$\mathcal{N}_S/\sqrt{\mathcal{N}_S+\mathcal{N}_B}$	$\mathcal{L}^{req}(5\ \sigma) fb^{-1}$
BP1	359	0.60	202	63	12.43	32.3
BP2	256	0.67	137	50	10.03	49.7
BP3	346	0.42	183	49	12.03	34.5
BP4	153	0.65	87	15	8.61	67.4
BP5	32	0.61	25	51	2.9	595.4
BP6	74	0.58	37	42	4.2	283.2
U1	266	0.57	149	49	10.6	44.4
U2	352	0.56	216	41	13.5	27.4
$\mathcal{N}_{\rm SM}$	212436	-	-	-	-	

Table 5.6: Total number of signal events $\mathcal{N}_S^{bc}$ and background events $\mathcal{N}_{\rm SM}$ before utilising the optimum BDT criteria BDT$_{opt}$ for an integrated luminosity of 200 fb^{-1} at the 14 TeV LHC. The number of signal and background events after the BDT$_{opt}$ cut are denoted by $\mathcal{N}_S$ and $\mathcal{N}_B$ respectively. Finally, listed the statistical significance for an integrated luminosity of 200 fb^{-1} and also required luminosity for a five sigma discovery in case of each BP.

5.3.5 Complementary signals at high energy and high luminosity upgrades of LHC at $\sqrt{s}$=27 TeV

Semi-leptonic and leptonic channels with leptons inside the fat jet, i.e, *lepton-jets* are potential alternate channels to confirm the presence of the higgsino-like NLSP besides the hadronic channel. For example, the decay chain $\widetilde{\chi}_1^0 \to hh/hZ, (h \to WW^*), (W \to jj, W \to l\nu)$ will give rise to an interesting signature of a lepton inside the fat jet due to high boost of the Higgs. Note that a leptonic decay of the Z boson would also lead to a pair of collimated leptons in the final state. Therefore new signatures with lepton(s) inside jets such as $(jj)(jj)$, $(jj)(ll)$, $(jj)(jjl)$ and $(ll)(ll)$ along with $\not{E}_T$ (where $l = e, \mu$) may serve as complementary signals to identify the current scenario. We estimate the number of events prior to signal analysis as summarised in Tab. 5.7 for $\sqrt{s}$ = 14 (27) TeV at 3 (15) ab^{-1}. We have used the `NNPDF` [174] parton distribution function to generate the signal events at $\sqrt{s}$ = 27 TeV and obtained the K-factors at NLO from `Prospino` [175–179].

From Tab. 5.7 it is observed that the fully hadronic final state $(jj)(jj)$ is the best channel for discovery of the higgsino NLSP scenario over the other leptonic and semi-leptonic channels due to the dominant branching fraction into the hadronic channel. Although the number of events are expected to fall after all

Channel	$\sqrt{s} = 14$ ($\mathcal{L} = 3ab^{-1}$) TeV	$\sqrt{s} = 27$ TeV ($\mathcal{L} = 15ab^{-1}$)
$(jj)(jj)$	4593	756177
$(jj)(ll)$	352	58011
$(ll)(ll)$	13	2126
$(jj)(jjl)$	4	664
$(ll)(jjl)$	1	157

Table 5.7: Number of events computed using $\sigma * BR$ for **BP1** at NLO for $\sqrt{s} = 14$ ($\mathcal{L} = 3\text{ab}^{-1}$) and 27 TeV ($\mathcal{L} = 15\text{ab}^{-1}$) at LHC before analysis cuts are applied.

detector effects such as reconstruction efficiencies of the jets and leptons are taken into account. Further, signal selection criteria would also lead to reduction in the number of observed events. Therefore, at $\sqrt{s} = 14$ TeV, only the fully hadronic channel is the best possible channel for discovery of the higgsino-NLSP scenario. From Sec. 5.3, at $\sqrt{s} = 14$ TeV we see that the two fat jet + $\not{E}_T$ final state can reach a mass range of $\simeq 2.4 - 3$ TeV at an integrated luminosity, $\mathcal{L} = 200$ fb $^{-1}$. Although the semi-leptonic channels $(jj)(ll)$ and $(jj)(jjl)$ can be interesting channels of discovery due to the presence of leptons in the final state, they have relatively fewer events at $\sqrt{s} = 14$ TeV and are not expected to be significant after detector effects and signal selection efficiencies are taken into account. However such channels would possibly be discoverable at the high energy upgrade of the LHC at $\sqrt{s} = 27$ TeV as shown in Tab. 5.7. The dilepton pair (ll) arising from the decay of the Z boson would also be an indicator of the composition of the NLSP since the Z boson arising from the decay of the higgsino-like NLSP would be longitudinally polarised in the high energy limit where $\sqrt{s} >> m_Z$. On the contrary, a gaugino-like NLSP would give rise to a mostly transversely polarised Z boson. Therefore, the presence of the longitudinal Z boson would be useful to ascertain the higgsino-like nature of the NLSP. Kinematic observables such as $\cos\theta^*$ and other variables derived therefrom are useful to explore the polarisation of the Z boson as has been studied in [147] for non-boosted topologies. We leave such studies using boosted techniques for a future work. In addition, channels including a lepton inside a jet, such as (jjl) dominantly arise from the decay of the Higgs, $h \to WW^* \to jjl$ in the final state. It would be a useful indicator of the presence of a Higgs boson in the final state as opposed to a Z boson and thereby affirming the higgsino-like composition of the NLSP.

5.4 Distinction of Compressed and Uncompressed spectra

As the results suggest in Tab. 5.6, the signal yield for different compression is similar for a few benchmarks. It is important to compare the scenario of different compression scale. We define ΔM as compression scale, where ΔM is the mass difference between the heaviest colour particle and the NLSP. ΔM varies from 56-190 GeV for the case of compressed spectra while for uncompressed it is in between 500 - 2000 GeV. With $\widetilde{G}$ being almost massless and NLSP being in the range of (1-3 TeV) we expect that the decay product of NLSP will be sufficiently boosted in both the cases. Hence both kinds of compression spectra satisfy the loose criteria of at least two fat jet.

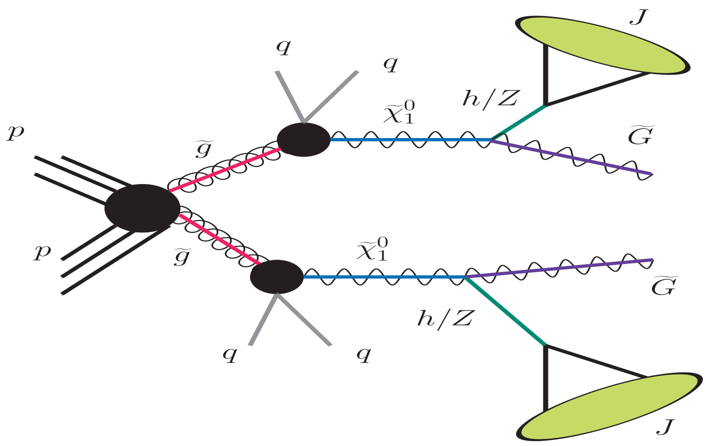

Figure 5.7: Representative diagram for the signal topology.

A large number of high p_T jets are the result of the cascade decay in case of the uncompressed spectrum, whereas the compressed spectrum has very soft jet coming from the cascade decay. Using this information we design two new observables to distinguish these two spectra. To understand the construction of these observables the prototypical signal topology is shown in Fig. 5.7.

We first define the anti-kT jet (`AK4`) of radius parameter R = 0.4 with P_T = 20 GeV. Further, we identify these `AK4` jets (j_k) as "*unique jet*" jets which are not the part of fat jet (J_i) *i.e.* $\Delta R_{J_i j_k}$ between the reconstructed fat jet and a `AK4` jet is greater than 0.8. The origin of unique jets is primarily from cascade decay hence they can be identified in a small radius jet.

- The first observable is defined as the ratio of P_T of leading unique `AK4` jet by the P_T of leading fat jet, written as

$$\mathcal{Z}_1 = \frac{P_T(j_0)_{unique}}{P_T(J_0)}. \tag{5.5}$$

- Similarly, we define another variable as the ratio of P_T of leading unique jet by the P_T of sub-leading fat jet, written as

$$\mathcal{Z}_2 = \frac{P_T(j_0)_{unique}}{P_T(J_1)}. \tag{5.6}$$

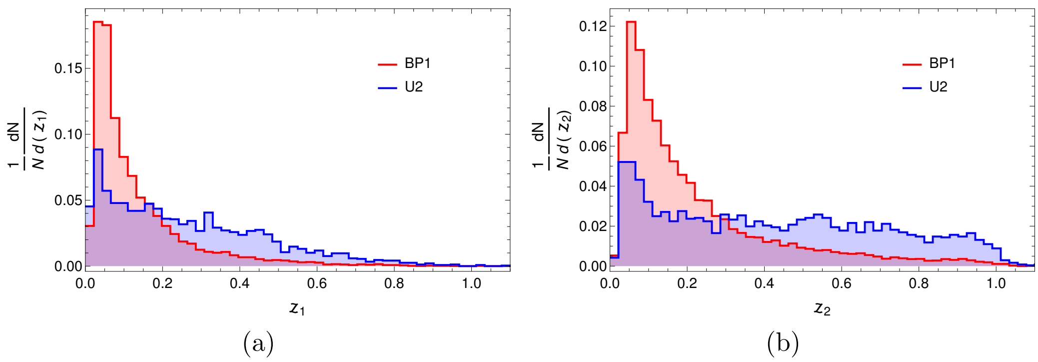

Figure 5.8: Normalised distributions of new kinematic variable $\mathcal{Z}_1$ and $\mathcal{Z}_2$ for the discriminant of compressed and uncompressed spectra.

The distribution for these variables are shown in Fig. 5.8a and 5.8b respectively. These distributions are plotted with the selected events after the BDT analysis. Evidently, both variables can capture significant information about the compression of the spectrum. The $\mathcal{Z}_1$ and $\mathcal{Z}_2$ both have significant contribution at smaller value for **BP1** (compressed case) compared to a relatively flat distribution in **U2** (uncompressed case). As expected, p_T of the leading unique jet is less in case of compressed than in the case of uncompressed spectra and these variables can be used as powerful discriminators in hadronic final state studies of cSUSY.

5.5 Summary and Conclusions

With no clear indication of new physics yet at the LHC, compressed mass spectrum gained significant limelight as a possible explanation for the elusive nature in the realisation of new physics. In this work, we consider a compressed SUSY scenario, where both coloured and electro-weak new physics sectors are sitting at multi-TeV scale in the presence of a light gravitino as dark matter candidate. The lightest neutralino, which is also the natural NLSP candidate in phenomenological MSSM, decays into the gravitino together with Higgs or Z-boson. A large mass gap between them invariably produces a significantly boosted boson. Recognising the fact that its hadronic decay can form boosted fat jet objects opens up an intriguing new possibility. This new channel can be beneficial contrary to looking through the typical leptonic search which is in any case expected to be suppressed by small branching ratio, or reconstruction efficiency at a high p_T. Moreover, reconstructed fat jets can still carry the characteristics of the parent particle in their masses and substructures. The present analysis exploits such properties to counter the extensive background coming from QCD jets. With multiple observables, including pruned fat jet masses, energy correlation functions as well as N-subjettiness, we demonstrate the full potential of jet substructure by using a dedicated multivariate analysis. The LHC sensitivity can be improved substantially that most of the constructed benchmark points can be explored with an integrated luminosity of 200 fb^{-1} at the 14 TeV LHC. One can exclude masses up to 3.2 TeV at $\mathcal{L} = 3000$ fb^{-1}, with a 3.2 σ signal significance achievable for a compressed spectrum similar to **BP6** ($\Delta M \simeq 60$ GeV).

At this point, it is worth mentioning that an uncompressed scenario can produce characteristically different signature. We constructed new observables in our present framework sensitive to the compression of our model. New possible leptonic and semi-leptonic signatures are also proposed which would be observable at a high energy and high luminosity upgrade of the LHC at $\sqrt{s} = 27$ TeV.

Chapter 6

Determining the Higgs CP properties

After finding the long-sought Higgs boson, one of the main goal for LHC is to determine its properties. The possibility of CP-odd Higgs is completely ruled out but a CP admixture with both the scalar and the pseudoscalar components is still allowed. A CP admixture Higgs would lead to the CP-violating couplings with other SM particles. CPV in the Higgs sector is more prominent in its fermionic couplings than gauge boson couplings as the couplings of the pseudoscalar to gauge bosons are absent at tree level and can only arise at the one-loop level. We explored the possibility of CP-violation in the $H\tau^+\tau^-$ Yukawa coupling. For this we proposed several obserbavles which are sensitive to the Higgs CP phase [180]. We also provide a novel technique to reconstruct the τ momentum decaying semi-invisible.

In next Sec. 6.1, we introduce the importance of looking at the $H \to \tau^+\tau^-$ channel for the CP phase. Thereafter, in Sec. 6.2 we introduce the CP observables and their construction. Since the rest frame observables are proved to be more effective, reconstruction of these semi-invisible events are necessary which will be discussed in Sec. 6.3. We discuss a new method for reconstructing the semi-invisible tau decay, All the results together with the capability of studying CP phase is finally presented in Sec. 6.4 before concluding in Sec. 6.5.

6.1 Higgs boson production and decays

We study the decay of Higgs in to the $H \to \tau^+\tau^-$ final state through our methodology to determine the CP phase in the $H \to \tau^+\tau^-$ coupling. Here we are interested in the gluon fusion channel, however the mehtod can easily be applied to any other Higgs production channel, such as, VBF process or the associated vector boson productios. We consider both the τ^+ and τ^- to decay hadronically in order to minimise the loss of kinematic information due to multiple missing neutrinos. For the τ's decay modes, we take into account the following 1-prong decays in our analysis: $\tau^\pm \to \pi^\pm\, \nu_\tau$. A representative diagram for the Higgs production and its decay to $\tau^+\tau^-$ followed by τ decays has been shown in Fig. 6.1.

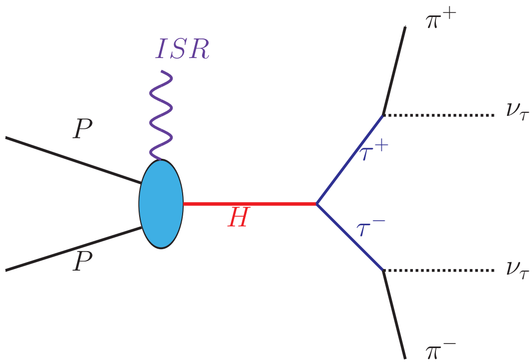

Figure 6.1: Representative diagram for $h \to \tau^-\tau^+$ with tau lepton decay hadronically via one prong decay channel. We assign momenta for the final state invisible (neutrinos) and visible (pions) particles as q_i and p_i respectively with i = 1,2.

In our analysis, we consider the Higgs boson to be a CP admixture and does not have a definite CP transformation properties. The model for such a scenario could be an extension of a Higgs sector such as 2HDM, MSSM etc. with a CP violation in Higgs couplings. The Yukawa terms in the Lagrangian for such a Higgs boson can be parameterised as following:

$$\mathcal{L} \supset -m_\tau \bar{\tau}\tau - \frac{y_\tau}{\sqrt{2}} H\bar{\tau}(\cos\alpha + i\gamma_5 \sin\alpha)\tau \tag{6.1}$$

where τ and H are the physical fields, respectively, y_τ is the effective strength of the τ-Yukawa interaction and α denotes the degree of mixing of the scalar and pseudoscalar component of the Higgs boson. For the SM Higgs boson, α

vanishes identically at tree level reproducing a CP even Higgs and $y_\tau = m_\tau/v$. The CP phase can vary in the range $(-\frac{\pi}{2}, \frac{\pi}{2})$ with $\alpha = \pi/2$ corresponds to a pure pseudoscalar and $\alpha = \pi/4$ to a maximally CP-violating case. Here to go forward we keep the y_τ fixed to the SM value and only vary the CP phase of the τ-Yukawa coupling to study the deviations in the expectation values of the observable with respect to the CP phase.

In our analysis, we consider Higgs mass $M_h = 125$ GeV. We have incorporated the anomalous Higgs couplings to tau leptons in `Madgraph` [72] using `FeynRules` [133]. The decays of the taus are handled with the tau-decay model [181] implemented in `Madgraph`. We use `Madgraph` to generate the parton level events which are then passed to the `Pythia` [182] for our analysis.

6.2 Observables

The Higgs spin and parity information are coded into the correlations between τ^+ and τ^- spins. The spin of $\tau^\pm$ and correlation between τ^+ and τ^- spins are not directly measurable rather they are determined from the distribution of their decay products. They may also manifest themselves in the correlations among momenta of the $\tau^\pm$ decay products in particular to the plane transverse to $\tau^+\tau^-$ axes. This is because the decay distribution of $(H/A \to \tau^+\tau^-)$ is proportional to $d\Gamma \propto (1 + s_{||}^{\tau^+} s_{||}^{\tau^-} \pm s_{\perp}^{\tau^+} s_{\perp}^{\tau^+})$ [183] where $||$ and $\perp$ denote the longitudinal and transverse components of $\tau^\pm$ spin with respect to Higgs momentum as seen from the $\tau^+\tau^-$ rest frame.

Taking into account of the aforementioned fact and recognizing that a triple product correlation is sensitive to a scalar and pseudoscalar contribution, we study several simple triple product correlations constructed out of momenta of the particles involved in the process. We utilise the momenta of the τ^+, τ^- and their decay products, i.e., $\pi^\pm$, to construct momentum correlations. Under CP, $\vec{p}_{\tau^-} \xrightarrow{CP} -\vec{p}_{\tau^+}$ and $\vec{p}_{\pi^-} \xrightarrow{CP} -\vec{p}_{\pi^+}$. A triple product correlation transforms under CP as: $\vec{p}_{\tau^-} \cdot (\vec{p}_{\pi^-} \times \vec{p}_{\pi^+}) \xrightarrow{CP} -\vec{p}_{\tau^-}.(\vec{p}_{\pi^-} \times \vec{p}_{\pi^+})$. Thus, all the observables listed in Tab. 6.1 are CP odd and T odd*. Note that the list does not exhaust all possible

*Henceforth, T will always refer to naive time reversal, i.e., reversal of all momenta and combination of triple product correlations involving particle momenta involved in the process. But here our primary interest was to construct triple product in terms momenta of tau leptons and pions in the most trivial way possible. In principle, one could also include each neutrino momenta in constructing these correlations provided that they are determined at the LHC. Here we focus only on those combinations having substantial sensitivity to the cp phase.

The amplitude for the full Higgs decay chain $h \to \tau^+\tau^- \to \pi^+\pi^-\nu_\tau\bar{\nu}_\tau$ can be written as

$$\mathcal{M} \quad \propto \quad \bar{u}_{\nu_\tau}(\not{p}_{\tau^-} + \mathrm{m}_\tau)(\cos\alpha + \mathrm{i}\gamma_5 \sin\alpha) \times (-\not{p}_{\tau^+} + \mathrm{m}_\tau)\mathrm{P_L}\mathrm{v}_{\bar{\nu}_\tau}. \tag{6.2}$$

In a full matrix element squared, one would get CP angle α independent and dependent terms. Here we are only interested in α dependent terms. The decay distribution for this process contains a triple product correlation like the ones we have listed in Tab. 6.1 which one can get after summing over all the fermion spins in terms of $\epsilon_{\mu\nu\rho\sigma} p^\mu_{\tau^-} p^\nu_{\tau^+} p^\rho_{\pi^-} p^\sigma_{\pi^+}$. Here we have replaced neutrino momentum by $p_{\nu_\tau} = p_\tau - p_\pi$.

We consider two different frames to study these momentum correlations. Observables $\mathcal{O}_1$ have been defined in $\tau^+\tau^-$ zero momentum frame (ZMF) in which both τ^+ and τ^- are back-to-back (also known as "Higgs rest frame"). In the ZMF frame, due to the large difference in the Higgs boson mass and the τ lepton mass, the $\tau^\pm$ are highly boosted leading to highly collimated decay products along the direction of $\tau^\pm$ momentum. This brings in some difficulty to reconstruct momenta of each particle in the event and hinders the prospects of performing angular analysis in such a frame. To get around these setbacks, we also define a peculiar frame where one part of the scalar product, constructed using tau momenta or tau decay product momenta, is in the ZMF frame while the second part is constructed in $\tau^\pm$ rest frames (denoted as 'prime' frame). In addition, the polarization is a frame dependent quantity and it depends on the Lorentz boost of the observable. Although there is no unique way that decides the frame, we have constructed some of our observables in the prime frame in order to extract

spins without interchanging the initial and final states.

Observables	Frame
$\mathcal{O}_1 = (\vec{p}_{\tau^-} - \vec{p}_{\tau^+}).(\vec{p}_{\pi^-} \times \vec{p}_{\pi^+})$	ZMF
$\mathcal{O}_2 = (\vec{p}_{\tau^-} - \vec{p}_{\tau^+})^h.(\vec{p}_{\pi^-} \times \vec{p}_{\pi^+})^\tau$	Prime
$\mathcal{O}_3 = (\vec{p}_{\pi^-} - \vec{p}_{\pi^+})^\tau.(\vec{p}_{\pi^-} \times \vec{p}_{\pi^+})^h$	Prime
$\mathcal{O}_4 = (\vec{p}_{\pi^-} - \vec{p}_{\pi^+})^h.(\vec{p}_{\pi^-} \times \vec{p}_{\pi^+})^\tau$	Prime

Table 6.1: T odd observables constructed in the process $h \to \tau^+\tau^- \to \pi^+\pi^-\nu\bar{\nu}$ at the LHC. All the observables have the definite CP and T transformation properties. Observables $\mathcal{O}_1$ have been defined in the Higgs rest frame or ZMF frame, while $\mathcal{O}_{2-4}$ are defined in prime frame (defined in the text).

the polarization information maximally. Observables $\mathcal{O}_{2,3,4}$ are defined in this frame and the superscript h or τ in the expression is to mark the corresponding rest frame. Note that one of the observable $\mathcal{O}_2$ was first introduced in [184], where efficiency was studied along with effects of cuts and smearing. Our results are consistent with that study. In addition, we also present an asymmetry as a function of the CP phase.

6.3 Reconstruction of semi-invisible event

In the previous section, we discussed the observables which are triple product correlations constructed out of momenta of $\tau^\pm$ and $\pi^\pm$ in several frames. However, to get any meaningful information on the usefulness of these CP observables at the LHC, it remains to be seen how precisely one can reconstruct these semi-invisible tau pair events from the Higgs decay. Some of the recently proposed techniques in the literature particularly for such a scenario are in order. Popular and some of the early proposals, *viz.*, *collinear approximation* [185, 186] determine invisible neutrino momenta by assuming tau decay products to be collinear. With this assumption, the neutrino(s) from tau take a fraction of tau momenta which results in the reduction of unknowns to two. Neutrino momenta then can be solved exactly using missing transverse momenta constraints. *Missing mass calculator* [187, 188] solves for the four unknown components (explained in the next paragraph) of the neutrino momenta and remaining two unknowns are parametrised using a probability function. The probability function utilises an independent measurement of angular separation between visible and invisible particles from $Z \to \tau\tau$ channel. *Displaced vertex method* [189] assumes at least one tau decays via 3−prong channel. It determines the tau momenta by utilizing the secondary vertex information and available constraints in the event. *Constrained $\hat{s}$ method* [190] assigns momenta to tau after optimizing the phase space by taking care of available kinematic constraints. *M_{2Cons} method* [191,192] is a 3D M_2 variable which minimises phase space by utilizing the Higgs mass and transverse momenta constraints and gives generic mass measurement prescription for antler decay topology. The reconstruction of neutrino momenta, in the present scenario, proved to be very precise. Recently developed reconstruction [193] utilises the tau mass-shell, missing transverse constraints together with measured impact parameter to reconstruct the semi-invisible events. The impact parameter is the perpendicular distance of pion momentum direction from the Higgs boson production vertex which can be identified using the tracks of jets produced with Higgs.

While there are many reconstruction methods, most of them are not sensitive to the observables considered in this analysis. A method which approximates the neutrino momenta exactly along the tau direction may not be sensitive to these variables because each of them is scalar triple products. In general, full reconstruction of these events is challenging because even for the hadronic decay of tau, there are two neutrinos present in the final state which traverse the detector without getting detected. Full reconstruction of $h \to \tau^+\tau^- \to \pi^+\pi^-\nu_\tau\bar{\nu}_\tau$ requires determining all the components of the neutrinos momenta involved in the process. Assuming that there is no other source of missing energy in the process, the measured missing transverse momentum can be parametrised in terms of the unknown neutrinos momenta as follows,

$$\not{E}_{Tx} = q_{\nu 1}\sin\theta_{\nu 1}\cos\Phi_{\nu 1} + q_{\nu 2}\sin\theta_{\nu 2}\cos\Phi_{\nu 2}, \quad (6.3)$$

$$\not{E}_{Ty} = q_{\nu 1}\sin\theta_{\nu 1}\sin\Phi_{\nu 1} + q_{\nu 2}\sin\theta_{\nu 2}\sin\Phi_{\nu 2}, \quad (6.4)$$

where $q_{\nu 1,2}$ are the magnitude of the neutrino momenta and $\theta_{\nu 1,\nu 2}$, $\Phi_{\nu 1,\nu 2}$ are polar and azimuthal angles of the neutrinos respectively. As it is evident from Eq. 6.3 and 6.4 that each tau pair event is under constraint because there are six unknowns but only five measurements including the tau and Higgs mass-shell constraints.

We start with two unknown degrees of freedom, $\Phi_{\nu 1}$ and $\Phi_{\nu 2}$, and scan over the full parameter space to completely solve the system with a mass window of 2 GeV for Higgs boson which we attributed to the fact there can be, unknown measurement, error in it. This resulted in fixing the angular separation between the corresponding visible and invisible particle but one parameter is still not constrained allowing the infinite number of solutions possible in each event.

At this point, it is important to note that the tau pair produced from Higgs decay possess considerably large decay length, as large as 87 μm, which we have not used so far. The large decay length of tau, in turn, allows for the measurement of the impact parameter which can then be used to get the tau direction. This additional measurement along with the other constraints discussed above uniquely determines the neutrinos momenta in each event[†].

To calculate the tau decay length vector first we take exact primary vertex coordinate from the `Pythia` (v8) [73] and calculated the impact parameter. We then smeared the primary vertex [194] using Gaussian smearing distribution with $\sigma_T = 0.01\ mm$ and $\sigma_Z = 0.1\ mm$, in order to take the measurement error into account. We pick that unique solution of $\Phi_{\nu 1}$ and $\Phi_{\nu 2}$ which gives the minimum error associated with the reconstructed tau decay length vector.

6.4 Results

In this section, we discuss the statistical sensitivity of the observables proposed in this paper on the measurement of the CP phase of the tau Yukawa coupling. For the analysis, corresponding to each of the T odd observables $\mathcal{O}_{1,2,3,4}$, we focus on the angular correlations among the triple products listed in Tab. 6.1, i.e.,

[†]Note that the reconstruction proposed in ref. [193] is slightly different than our method because it uses both the impact parameter of tau as well as the Higgs mass constraint to fully reconstruct the event. Since there are large measurement errors associated with the impact parameter, we took the one with larger magnitude for our analysis.

$\cos\theta_i = \hat{P}\cdot\hat{Q}$ where P and Q are first and second terms of the scalar-triple products. We display the distributions of angular correlations $\cos\theta_{1,2,3,4}$ in Fig. 6.2 for a pure scalar ($\alpha = 0$), pseudoscalar Higgs boson ($\alpha = \pi/2$) and for the maximally CP violating case ($\alpha = \pi/4$). As expected we find that the distribution is symmetric for $\alpha = 0$ and ($\alpha = \pi/2$) which denote the CP conserving scenarios and thus leading to the vanishing expectation values of the asymmetries (defined in Eq. 6.5) associated with these observables. On the other hand, for a maximally CP violating scenario i.e., $\alpha = \pi/4$, there is a significant distortion in the distributions relative to CP conserving case indicating that the asymmetries are sensitive to CP violating phase α.

For each distribution shown in the Fig. 6.2, we define a corresponding asymmetry as follows

$$A_{\theta_i} = \frac{1}{\mathcal{N}_{\rm tot}}\left[\mathcal{N}(\cos\theta_i < 0) - \mathcal{N}(\cos\theta_i > 0)\right] \tag{6.5}$$

where $\mathcal{N}_{\rm tot}$ is the total number of events. Note that the expression for the asymmetry can be applied for both the new physics contributions and the SM backgrounds. Including the contributions from the SM background, the total asymmetry, $A^{\rm total}_{\theta_i}$, can be written as

$$A^{\rm total}_{\theta_i} = A^{\rm NP}_{\theta_i} R + A^{\rm bckg}_{\theta_i}(1-R), \tag{6.6}$$

$$R = \frac{\sigma_{\rm NP}}{\sigma_{\rm NP}+\sigma_{\rm bckg}}, \tag{6.7}$$

where $\sigma_{\rm NP}$, $\sigma_{\rm bckg}$, $A^{\rm NP}_{\theta_i}$ and $A^{\rm bckg}_{\theta_i}$ are the contributions to new physics (NP) cross section, background cross section, asymmetry due to NP and asymmetry due to SM backgrounds respectively. From the Eqns. 6.6, we can see that the effect of the background contribution to the asymmetry is to reduce the magnitude of R and thus reducing the sensitivity of NP contribution to the asymmetry.

We also study the behavior of these asymmetries as a function of CP phase α. These asymmetries have been displayed in the right panels of Fig. 6.2 for observables $\mathcal{O}_{1,2,3,4}$ respectively. The blue (solid) curve for the asymmetry in the figure denote the truth-level scenario assuming that information regarding

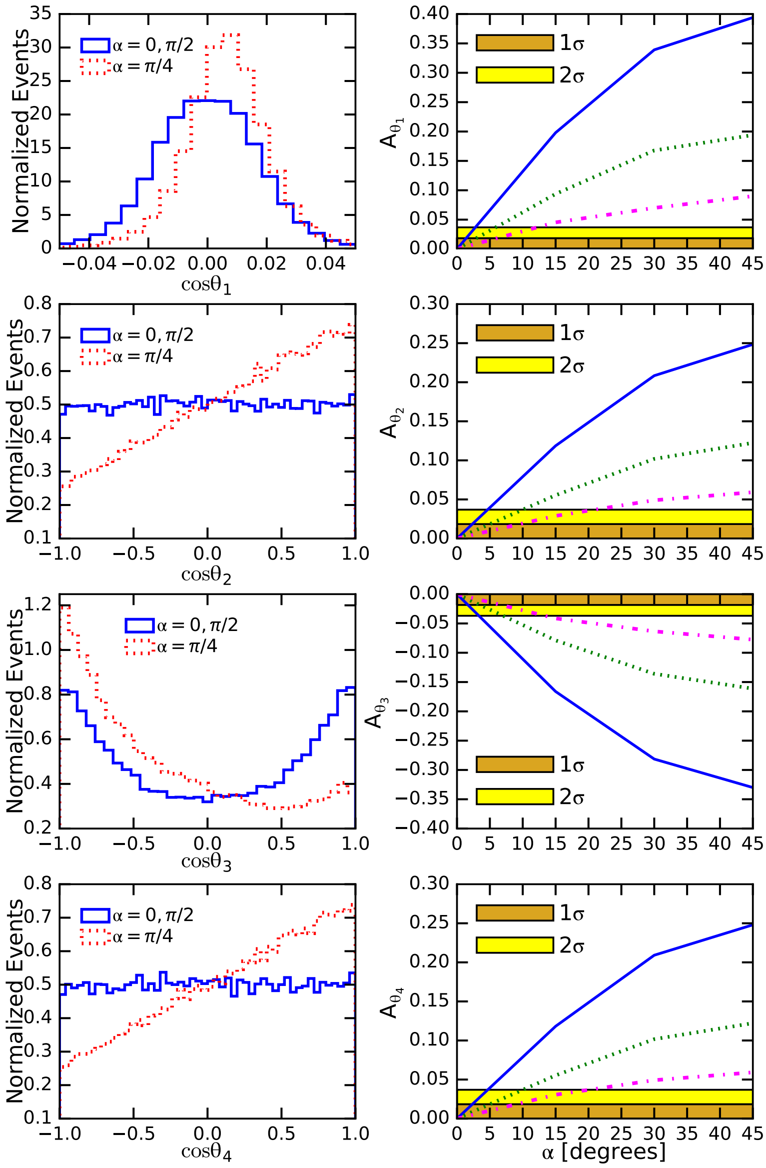

Figure 6.2: Distribution of $\cos\theta_i$ for observables $\mathcal{O}_{1,\ldots,4}$ considering various values of CP violating phase $\alpha = 0, \pi/2$ for pure CP conserving and $\pi/4$ for a maximally CP violating Higgs at the LHC. Variations of corresponding asymmetries versus the phase α are presented in the right plot. The 1σ and 2σ bands for the statistical uncertainties (obtained using Eq. 6.8) in the measurement of asymmetries with 1000 fb^{-1} of integrated luminosity at the LHC are also shown. Solid (blue), dotted (green) and dash-dotted (magenta) curves denote the asymmetries obtained using the information at truth level, reconstruction level and reconstruction level with smearing of primary vertex respectively.

the tau momenta is fully known. The green (dash-dotted) curve denote the case where the tau momenta have been reconstructed using the formalism discussed in Sec. 6.3. The magenta (dotted) curve is obtained when the reconstruction of tau moments is performed along with the smeared primary vertex and thus presents the most realistic estimation of the asymmetry in an actual LHC environment.

From the plots of asymmetries, we find that the asymmetry is vanishing for a CP conserving scenario ($\alpha = 0$ or $\pi/2$) resulting from a symmetric $\cos\theta_i$ distribution. For a maximally CP violating scenario ($\alpha = \pi/4$), the asymmetry is the largest for the observable $\mathcal{O}_3$ with the value $\sim 33\%$ (at truth-level) while observables $\mathcal{O}_{2,4}$ also provide the modest asymmetry of $\sim 25\%$. Also, the slopes of the asymmetries are fairly steep showing a good sensitivity to the measurement of CP phase α. However, at the realistic scenario (after the reconstruction of taus momenta and smeared primary vertex), the asymmetry drops somewhat as can be seen from the figure. Nevertheless, asymmetries are significant enough to provide stringent bounds on the CP angle α.

Looking at $\mathcal{O}_2$ and $\mathcal{O}_4$, one can realise that both are essentially the similar variables with first term replacing tau momenta with the corresponding pion momenta at the Higgs rest frame. In general, they can generate different contributions. However, in our present example, tau's are highly boosted at the Higgs rest frame. Thus, the decaying pion would essentially follow almost the same direction as corresponding tau and hence generating nearly close values both in these variables[‡]. This is also evident in the angular distribution and asymmetry.

We now discuss the sensitivity of these asymmetries to the measurement of CP phase, α, in $H\tau^+\tau^-$ coupling at the 13 TeV LHC. To obtain the bound on CP violating coupling α, we find those values of α for which the asymmetries deviate from the SM prediction by a certain confidence level. The statistical uncertainty in the measurement of an asymmetry is defined as follows

$$\Delta\mathcal{A} = \frac{\sqrt{1-\mathcal{A}_{\rm SM}^2}}{\sqrt{\sigma_{\rm SM}\;\epsilon\;\mathcal{L}}}, \tag{6.8}$$

where $\mathcal{L}$ is the integrated luminosity, $\mathcal{A}_{\rm SM}$ is the expected value of an asymme-

[‡]Here we emphasise that these observables can also be interesting, depending on the boost of the daughter particle, in other scenarios as well. For example the heavy Higgs, in a BSM scenario, to top pair process can be a potential channel to apply these variables where one does not expect the top quark to be highly boosted unlike the tau case, as a result the observable $\mathcal{O}_2$ and $\mathcal{O}_4$ would behaves differently.

try in the SM, $\sigma_{\rm SM}$ is the total tau pair cross section in the SM and ϵ is the experimental efficiency factor for the detection of such events after inclusion of realistic cuts and background elimination. We estimate this efficiency utilizing the recent analysis on Higgs boson searches in its hadronic τ decays. The ϵ is the ratio between the number of events after the realistic cuts and the expected number of events. From recent ATLAS paper [195] for gluon fusion channel and subsequent decays of Higgs into hadronic taus, the efficiency factor turned out to be 8.9%. The expected number of events is obtained by the product of the theoretical Higgs production cross section in gluon fusion at 8 TeV (19.27 pb), the Higgs decay branching ratio into tau pairs, tau decay branching fractions to charged pion and the integrated luminosity. We have assumed this efficiency factor to be same for 13 TeV and used in the estimation of sensitivity of our observables.

In the right panel of Fig. 6.2, we display the 1σ and 2σ statistical uncertainty in the measurement of respective asymmetries through shaded bands. While presenting these statistical regions, we consider 1000 fb^{-1} of integrated luminosity. From the figures, we find that the asymmetry A_{θ_1} is the most sensitive of all the asymmetries we analyzed in this analysis and the measurement of this asymmetry can determine the CP phase α up to 12 degrees at 2σ CL. The asymmetries A_{θ_2}, A_{θ_3} and A_{θ_4} can determine this angle up to 20, 15 and 20 degrees, respectively at 2σ CL for 13 TeV LHC.

In the Fig. 6.3 we present the 2σ statistical sensitivities of the observables up to which the CP phase α can be probed with the projected luminosity for 14 TeV at the HL-LHC. The sensitivity of each observable at the theoretical level (blue solid), reconstructed level (green dotted) and the reconstructed with the smeared primary vertex (magenta dashed-dotted) are displayed as a function of integrated luminosity ranging from 300 to 3000 fb^{-1}. We find that the asymmetry A_{θ_1} can pin down the CP phase α up to 6 degree for 3000 fb^{-1} at 14 TeV HL-LHC. Here we have taken the tau momentum reconstruction efficiency into account along with uncertainty in the primary vertex as well as the efficiency factor ϵ for this channel.

Note that while estimating the bounds on the CP violating phase α using various asymmetries, we do not include background contribution into the total asymmetry as defined in Eqns. 6.6. Thus, in this analysis, we assume R to be equal to 1. Thus, it is obvious that in the presence of background, the sensitivity of the various observables would reduce. Nevertheless, the focus of this work is to suggest some new observables for extracting CP phase in tau-Yukawa couplings and present a new reconstruction technique for tau-momentum at the LHC.

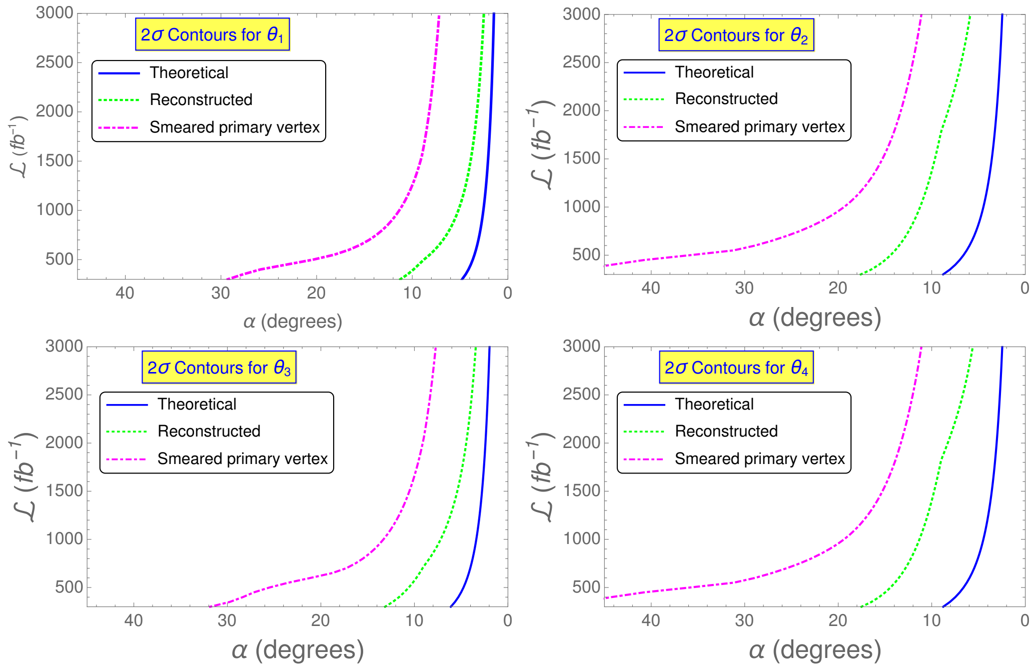

Figure 6.3: The figure shows 2σ statistical sensitivity for the CP phase α which can be pinned down with the increasing luminosity at the HL-LHC. The 2σ statistical sensitivity is calculated using information at truth level (blue solid), reconstruction level (green dotted) and reconstruction level with the smearing of primary vertex (magenta dash-dotted) respectively.

6.5 Summary and Conclusion

The determination of the CP properties of Higgs boson is one of the important aims at the large hadron collider (LHC) in its current and future runs. The goal is facilitated in the Higgs couplings to the third generation of fermions, in particular $\tau^{\pm}$ leptons. Spin of $\tau^{\pm}$ and the correlations between them may provide a great insight to the CP properties of Higgs boson. However, these are not directly measurable and manifest themselves in the distribution of its decay products.

In spirit of the aforementioned fact that the spin correlations are reflected in final state distributions, we proposed several triple product correlations which are constructed from the momenta of various particles involved in the process. Recognizing that the sensitive observables are best represented at the rest frame, we consider two different type of frames to study the correlations. These correlations have a definite CP and T transformation properties. We present the distribution of angular correlations obtained the various momentum correlations discussed earlier. These are shown to be sensitive to the CP phase in the $H\tau^+\tau^-$ couplings at the LHC.

In Sec. 6.3, we discussed various methods of tau momentum reconstruction available in the literature. We also proposed a new method of tau reconstruction which is based on the measurements of impact parameter and primary vertex. We employed this method to reconstruct the various observables studied in the paper and analyzed the distribution and asymmetries in the realistic LHC environment.

We also constructed the asymmetries using each angular correlation and studied their behavior as a function of the CP phase. Some of these asymmetries are found to be as large as 35% for the maximally CP violating scenario. A statistical analysis of the sensitivity of these asymmetries on the measurement of CP phase is studied with the reconstruction efficiency of $\tau^{\pm}$ pair events at the LHC. We found that with 1000 fb^{-1} of integrated luminosity, the CP phase can be determined up to 15 degrees at the 13 TeV LHC.

Chapter 7

Summary and Conclusions

The SM has been profoundly successful in explaining a broad range of experimental observations. In 2012, the remarkable discovery of the Higgs boson at the LHC fixes the last missing bit of the SM. However, it cannot explain the presence of tiny yet nonzero masses of the neutrinos that are already established in the observation of neutrino oscillation from the solar, atmospheric, reactor experiments. Besides, the SM does not contain any particle that can satisfy the observed density of the dark matter, along with explaining its other properties. These two major experimental observations, along with several others both for theoretical and experimental grounds, necessitate the extension of the SM. Many extensions are proposed both in terms of only particle extension or along with group extension in the literature to addressed these issues. Now, the main goal at the HL-LHC is to probe the properties of the Higgs boson and find the hint of new physics if it exists within its energy range.

Searching for new physics at the multi-TeV scale requires new techniques as it poses immense challenges. It is extremely important to search for BSM in all final states to explore the majority of its unexplored parameter space. In this view, hadronic final states play a crucial role as in most of the BSM scenarios new heavy particles decay into SM gauge bosons or the top quark and subsequent decay of these particles dominantly produces hadronic final states (jets). However, hadronic final states suffer from enormous QCD background in hadronic collider environment like the LHC and expected to be extremely difficult as a probe.

Such a stalemate can be broken by observing boosted jets produced through the decay of highly energetic heavy particle, although such observation requires new state-of-the-art techniques like jet-substructure. Construction of most of the jet observables in boosted regime is motivated by different energy distribution inside a fat jet. The energy distribution is symmetric when a boosted heavy particle decays(signal type), whereas the distribution is asymmetric in case of a high energy quark/gluon (background type). In this thesis, we cover a variety of different BSM scenarios in different hadronic final states which can be discovered or excluded in upcoming runs of the LHC.

We start by brief review the Standard Model of particle physics and also discuss some aspects why we need to look for physics beyond the SM. We also cover some key aspects of hadron collider physics required for the phenomenological analysis as cover in this thesis. In the next chapter, we provide a brief description of the methodology used to search for different BSM scenario explored in this thesis. The methodology is motivated with newly developed field of boosted topology and jet substructures to study the hadronic final states. We further discuss important jet substructure observables like invariant jet mass, N-subjettiness and Energy Correlation Functions. A brief discussion is on the multivariate analysis technique is also dicussed which we utilise to optimise the collider searches.

In chapter 3, we study the inverse seesaw model which is one the elegant way to generate small neutrino masses at TeV scale together with a large coupling to probe at the LHC. We study collider signatures of heavy pseudo-Dirac neutrinos with a sizable mixing with the SM neutrinos under two different flavour structures, viz., Flavour Diagonal (FD) and Flavour Non-Diagonal (FND) scenarios. For the latter scenario, we use a general parametrization for the model parameters by introducing an arbitrary orthogonal matrix and nonzero Dirac and Majorana phases. We then perform a parameter scan to identify allowed parameter regions which satisfy all experimental constraints. As an alternative channel to the traditional trilepton signature, we propose the opposite-sign di-lepton signature in the final state, in association with a fat jet from the hadronic decay of the boosted $W^{\pm}$. We specifically consider a fat jet topology and explore the required enhancements from exploiting the characteristics of the jet substructure techniques. We perform a comprehensive collider analysis to demonstrate the effectiveness of this channel in both of the scenarios, significantly enhancing the bounds on the RHN mass and mixing angles at the 13 TeV LHC. Interestingly we found that the FND scenario can reach up to a 5 σ limit under the presence of the general parametrization at the high luminosity LHC.

Next, we look for the simplest extension of the SM which can provide a viable candidate for the DM. In chapter 4, we explore the challenging but phenomenologically interesting hierarchical mass spectrum of the Inert Doublet Model where relatively light dark matter along with much heavier scalar states can fully satisfy the constraints on the relic abundance and also fulfil other theoretical as well as collider and astrophysical bounds. To probe this region of parameter space at the LHC, we propose a new signal process that combines up to two large radius boosted jets along with substantial missing transverse momentum. Aided by our intuitive signal selection, we capture a hybrid process where the di-fatjet signal is significantly enhanced by the mono-fatjet contribution with minimal effects on the SM di-fatjet background. Substantiated by the sizable mass difference between the scalars, these boosted jets, originally produced from the hadronic decay of massive vector bosons, still carry the inherent footprint of their root. These features implanted inside the jet substructure can provide additional handles to deal with a large background involving QCD jets. We adopt a multivariate analysis using boosted decision tree to provide a robust mechanism to explore the hierarchical scenario, which would bring almost the entire available parameter space well within reach of the 14 TeV LHC runs with high luminosity.

In chapter 5, We search for compressed supersymmetry at multi-TeV scale, in the presence of a light gravitino dark matter. It can get sizable uplift while looking into the associated fat jets with missing transverse momenta as a signature of the boson produced in the decay process of much heavier next-to-lightest sparticle. We focus on the hadronic decay of the ensuing Higgs and/or Z boson giving rise to at least two fat jets and $\not{E}_T$ in the final state. We perform a detailed background study adopting a multivariate analysis using a boosted decision tree to provide a robust investigation to explore the discovery potential for such signal at 14 TeV LHC considering different benchmark points satisfying all the theoretical and experimental constraints. This channel provides the best discovery prospects with most of the benchmarks discoverable within an integrated luminosity of $\mathcal{L} = 200$ fb^{-1}. We also propose two kinematic observables in order to distinguish between compressed and uncompressed spectra having similar event yields.

In chapter 6, we also explore the Higgs CP properties as a probe to BSM in the Higgs sector itself. we study the prospect of determining the CP-violating phase in τ-lepton Yukawa coupling at the LHC. While the current run is already exploring the production of a pair of the third generation τ leptons from Higgs decay, these measurements are not sensitive enough to constrain the CP-violating phase. In this paper, several CP odd observables are proposed and analyzed utilizing the dominant channels with the semi-invisible hadronic decay of τ. Several asymmetries corresponding to the T odd momentum correlations are also studied and their sensitivities to the CP-violating phase in tau-lepton Yukawa couplings are estimated at 13 TeV LHC with 1000 fb^{-1} of integrated luminosity. We also present a novel way to reconstruct τ momentum at the LHC utilizing the information of the impact parameter. Finally, we obtain that the asymmetries can be as large as 35% for a case of maximal CP violation in the τ Yukawa couplings.

In conclusion, this thesis covers many interesting BSM physics which could give the possible explanations which SM is still lacking. We provide robust analysis and techniques for the discovery of the BSM models studied in this thesis. We demonstrated the effectiveness of the jet substructure techniques along with different jet observables by employing them in a variety of BSM scenarios. Although in this thesis our focus has mainly on some particular models but can be applied to other BSM models since the methodology and analysis techniques due to its general nature. In Future, the present methodology can be improved further by using machine learning algorithms.

Bibliography

[1] S. L. Glashow, *Partial Symmetries of Weak Interactions*, *Nucl. Phys.* **22** (1961) 579–588.

[2] A. Salam and J. C. Ward, *Electromagnetic and weak interactions*, *Phys. Lett.* **13** (1964) 168–171.

[3] S. Weinberg, *A Model of Leptons*, *Phys. Rev. Lett.* **19** (1967) 1264–1266.

[4] Particle Data Group collaboration, M. Tanabashi et al., *Review of Particle Physics*, *Phys. Rev.* **D98** (2018) 030001.

[5] P. W. Anderson, *Plasmons, Gauge Invariance, and Mass*, *Phys. Rev.* **130** (1963) 439–442.

[6] P. W. Higgs, *Broken Symmetries and the Masses of Gauge Bosons*, *Phys. Rev. Lett.* **13** (1964) 508–509.

[7] F. Englert and R. Brout, *Broken Symmetry and the Mass of Gauge Vector Mesons*, *Phys. Rev. Lett.* **13** (1964) 321–323.

[8] G. S. Guralnik, C. R. Hagen and T. W. B. Kibble, *Global Conservation Laws and Massless Particles*, *Phys. Rev. Lett.* **13** (1964) 585–587.

[9] A. D. Sakharov, *Violation of CP Invariance, C asymmetry, and baryon asymmetry of the universe*, *Pisma Zh. Eksp. Teor. Fiz.* **5** (1967) 32–35.

[10] The Large Hadron Collider. `https://home.cern/science/accelerators/large-hadron-collider`.

[11] ATLAS collaboration, G. Aad et al., *The ATLAS Experiment at the CERN Large Hadron Collider*, *JINST* **3** (2008) S08003.

[12] CMS collaboration, S. Chatrchyan et al., *The CMS Experiment at the CERN LHC*, *JINST* **3** (2008) S08004.

[13] ALICE collaboration, K. Aamodt et al., *The ALICE experiment at the CERN LHC*, *JINST* **3** (2008) S08002.

[14] LHCb collaboration, A. A. Alves, Jr. et al., *The LHCb Detector at the LHC*, *JINST* **3** (2008) S08005.

[15] L. R. F. Castillo, "The atlas and cms detectors." http://dx.doi.org/10.1088/978-1-6817-4078-2ch4, 2015.

[16] G. F. Sterman and S. Weinberg, *Phys. Rev. Lett.* **39** (1977) 1436.

[17] W. Bartel et al., *[JADE Collaboration], Z. Phys. C* **33** (1986) 23.

[18] S. Bethke et al., *[JADE Collaboration], Phys. Lett. B* **213** (1988) 235.

[19] S. Catani, Y. L. Dokshitzer, M. Olsson, G. Turnock and B. R. Webber, *Phys. Lett. B* **269** (432) 1991.

[20] S. D. Ellis and D. E. Soper, *Successive combination jet algorithm for hadron collisions*, *Phys. Rev. D* **48** (1993) 3160–3166, [hep-ph/9305266].

[21] M. Cacciari, G. P. Salam and G. Soyez, *The anti-k_t jet clustering algorithm*, *JHEP* **04** (2008) 063, [0802.1189].

[22] Y. L. Dokshitzer, G. Leder, S. Moretti and B. Webber, *Better jet clustering algorithms*, *JHEP* **08** (1997) 001, [hep-ph/9707323].

[23] G. P. Salam, *Towards Jetography*, *Eur. Phys. J. C* **67** (2010) 637–686, [0906.1833].

[24] J. Shelton, *Jet Substructure*, in *Theoretical Advanced Study Institute in Elementary Particle Physics: Searching for New Physics at Small and Large Scales*, pp. 303–340, 2013. 1302.0260. DOI.

[25] D. Krohn, J. Thaler and L.-T. Wang, *Jet Trimming*, *JHEP* **02** (2010) 084, [0912.1342].

[26] S. D. Ellis, C. K. Vermilion and J. R. Walsh, *Techniques for improved heavy particle searches with jet substructure*, *Phys. Rev.* **D80** (2009) 051501, [0903.5081].

[27] S. D. Ellis, C. K. Vermilion and J. R. Walsh, *Recombination Algorithms and Jet Substructure: Pruning as a Tool for Heavy Particle Searches*, *Phys. Rev.* **D81** (2010) 094023, [0912.0033].

[28] J. M. Butterworth, A. R. Davison, M. Rubin and G. P. Salam, *Jet substructure as a new Higgs search channel at the LHC*, *Phys. Rev. Lett.* **100** (2008) 242001, [0802.2470].

[29] J. Thaler and K. Van Tilburg, *Identifying Boosted Objects with N-subjettiness*, *JHEP* **03** (2011) 015, [1011.2268].

[30] J. Thaler and K. Van Tilburg, *Maximizing Boosted Top Identification by Minimizing N-subjettiness*, *JHEP* **02** (2012) 093, [1108.2701].

[31] M. Cacciari, G. P. Salam and G. Soyez, *FastJet User Manual*, *Eur. Phys. J.* **C72** (2012) 1896, [1111.6097].

[32] A. J. Larkoski, I. Moult and D. Neill, *Power Counting to Better Jet Observables*, *JHEP* **12** (2014) 009, [1409.6298].

[33] I. Moult, L. Necib and J. Thaler, *New Angles on Energy Correlation Functions*, *JHEP* **12** (2016) 153, [1609.07483].

[34] S. Marzani, G. Soyez and M. Spannowsky, *Looking inside jets: an introduction to jet substructure and boosted-object phenomenology*, vol. 958. Springer, 2019, 10.1007/978-3-030-15709-8.

[35] B. P. Roe, H.-J. Yang, J. Zhu, Y. Liu, I. Stancu and G. McGregor, *Boosted decision trees, an alternative to artificial neural networks*, *Nucl. Instrum. Meth. A* **543** (2005) 577–584, [physics/0408124].

[36] A. Hocker et al., *TMVA - Toolkit for Multivariate Data Analysis*, physics/0703039.

[37] P. Minkowski, *$\mu \to e\gamma$ at a Rate of One Out of 10^9 Muon Decays?*, *Phys. Lett.* **67B** (1977) 421–428.

[38] T. Yanagida, *Horizontal Symmetry and Masses of Neutrinos*, *Prog. Theor. Phys.* **64** (1980) 1103.

[39] J. Schechter and J. W. F. Valle, *Neutrino Masses in SU(2) x U(1) Theories*, *Phys. Rev.* **D22** (1980) 2227.

[40] O. Sawada and A. Sugamoto, eds., *Proceedings: Workshop on the Unified Theories and the Baryon Number in the Universe*, (Tsukuba, Japan), Natl.Lab.High Energy Phys., Natl.Lab.High Energy Phys., 1979.

[41] M. Gell-Mann, P. Ramond and R. Slansky, *Complex Spinors and Unified Theories*, *Conf. Proc.* **C790927** (1979) 315–321, [1306.4669].

[42] S. L. Glashow, *The Future of Elementary Particle Physics*, *NATO Sci. Ser. B* **61** (1980) 687.

[43] R. N. Mohapatra and G. Senjanovic, *Neutrino Mass and Spontaneous Parity Violation*, *Phys. Rev. Lett.* **44** (1980) 912.

[44] S. Weinberg, *Baryon and Lepton Nonconserving Processes*, *Phys. Rev. Lett.* **43** (1979) 1566–1570.

[45] R. N. Mohapatra, *Mechanism for Understanding Small Neutrino Mass in Superstring Theories*, *Phys. Rev. Lett.* **56** (1986) 561–563.

[46] R. N. Mohapatra and J. W. F. Valle, *Neutrino Mass and Baryon Number Nonconservation in Superstring Models*, *Phys. Rev.* **D34** (1986) 1642.

[47] A. Das, P. S. B. Dev and R. N. Mohapatra, *Same Sign versus Opposite Sign Dileptons as a Probe of Low Scale Seesaw Mechanisms*, *Phys. Rev. D* **97** (2018) 015018, [1709.06553].

[48] A. Das, P. S. Bhupal Dev and N. Okada, *Direct bounds on electroweak scale pseudo-Dirac neutrinos from $\sqrt{s} = 8$ TeV LHC data*, *Phys. Lett.* **B735** (2014) 364–370, [1405.0177].

[49] A. Das and N. Okada, *Improved bounds on the heavy neutrino productions at the LHC*, *Phys. Rev.* **D93** (2016) 033003, [1510.04790].

[50] G. 't Hooft, *Naturalness, chiral symmetry, and spontaneous chiral symmetry breaking*, *NATO Sci. Ser. B* **59** (1980) 135–157.

[51] A. Bhardwaj, A. Das, P. Konar and A. Thalapillil, *Looking for Minimal Inverse Seesaw scenarios at the LHC with Jet Substructure Techniques*, *J. Phys. G* **47** (2020) 075002, [1801.00797].

[52] F. del Aguila and J. A. Aguilar-Saavedra, *Distinguishing seesaw models at LHC with multi-lepton signals*, *Nucl. Phys.* **B813** (2009) 22–90, [0808.2468].

[53] M. Malinsky, T. Ohlsson, Z.-z. Xing and H. Zhang, *Non-unitary neutrino mixing and CP violation in the minimal inverse seesaw model*, *Phys. Lett.* **B679** (2009) 242–248, [0905.2889].

[54] I. Garg, S. Goswami, K. N. Vishnudath and N. Khan, *Electroweak vacuum stability in presence of singlet scalar dark matter in TeV scale seesaw models*, *Phys. Rev.* **D96** (2017) 055020, [1706.08851].

[55] A. Das and N. Okada, *Inverse seesaw neutrino signatures at the LHC and ILC*, *Phys. Rev.* **D88** (2013) 113001, [1207.3734].

[56] A. Das and N. Okada, *Bounds on heavy Majorana neutrinos in type-I seesaw and implications for collider searches*, *Phys. Lett.* **B774** (2017) 32–40, [1702.04668].

[57] J. A. Casas and A. Ibarra, *Oscillating neutrinos and muon $---> e$, gamma*, *Nucl. Phys.* **B618** (2001) 171–204, [hep-ph/0103065].

[58] Daya Bay collaboration, F. P. An et al., *Observation of electron-antineutrino disappearance at Daya Bay*, Phys. Rev. Lett. **108** (2012) 171803, [1203.1669].

[59] Particle Data Group collaboration, C. Patrignani et al., *Review of Particle Physics*, Chin. Phys. **C40** (2016) 100001.

[60] S. Antusch, C. Biggio, E. Fernandez-Martinez, M. B. Gavela and J. Lopez-Pavon, *Unitarity of the Leptonic Mixing Matrix*, JHEP **10** (2006) 084, [hep-ph/0607020].

[61] A. Abada, C. Biggio, F. Bonnet, M. B. Gavela and T. Hambye, *Low energy effects of neutrino masses*, JHEP **12** (2007) 061, [0707.4058].

[62] A. Ibarra, E. Molinaro and S. T. Petcov, *TeV Scale See-Saw Mechanisms of Neutrino Mass Generation, the Majorana Nature of the Heavy Singlet Neutrinos and $(\beta\beta)_{0\nu}$-Decay*, JHEP **09** (2010) 108, [1007.2378].

[63] A. Ibarra, E. Molinaro and S. T. Petcov, *Low Energy Signatures of the TeV Scale See-Saw Mechanism*, Phys. Rev. **D84** (2011) 013005, [1103.6217].

[64] D. N. Dinh, A. Ibarra, E. Molinaro and S. T. Petcov, *The $\mu - e$ Conversion in Nuclei, $\mu \to e\gamma, \mu \to 3e$ Decays and TeV Scale See-Saw Scenarios of Neutrino Mass Generation*, JHEP **08** (2012) 125, [1205.4671].

[65] MEG collaboration, J. Adam et al., *New limit on the lepton-flavour violating decay $\mu^+ \to e^+\gamma$*, Phys. Rev. Lett. **107** (2011) 171801, [1107.5547].

[66] BaBar collaboration, B. Aubert et al., *Searches for Lepton Flavor Violation in the Decays tau+- —¿ e+- gamma and tau+- —¿ mu+- gamma*, Phys. Rev. Lett. **104** (2010) 021802, [0908.2381].

[67] SuperB collaboration, B. O'Leary et al., *SuperB Progress Reports – Physics*, 1008.1541.

[68] MEG collaboration, A. M. Baldini et al., *Search for the lepton flavour violating decay $\mu^+ \to e^+\gamma$ with the full dataset of the MEG experiment*, *Eur. Phys. J.* **C76** (2016) 434, [1605.05081].

[69] E. Fernandez-Martinez, J. Hernandez-Garcia and J. Lopez-Pavon, *Global constraints on heavy neutrino mixing*, *JHEP* **08** (2016) 033, [1605.08774].

[70] S. Antusch, E. Cazzato, O. Fischer, A. Hammad and K. Wang, *Lepton Flavor Violating Dilepton Dijet Signatures from Sterile Neutrinos at Proton Colliders*, *JHEP* **10** (2018) 067, [1805.11400].

[71] J. Alwall, M. Herquet, F. Maltoni, O. Mattelaer and T. Stelzer, *MadGraph 5 : Going Beyond*, *JHEP* **06** (2011) 128, [1106.0522].

[72] J. Alwall, R. Frederix, S. Frixione, V. Hirschi, F. Maltoni, O. Mattelaer et al., *The automated computation of tree-level and next-to-leading order differential cross sections, and their matching to parton shower simulations*, *JHEP* **07** (2014) 079, [1405.0301].

[73] T. Sjostrand, S. Mrenna and P. Z. Skands, *PYTHIA 6.4 Physics and Manual*, *JHEP* **05** (2006) 026, [hep-ph/0603175].

[74] M. L. Mangano, M. Moretti, F. Piccinini and M. Treccani, *Matching matrix elements and shower evolution for top-quark production in hadronic collisions*, *JHEP* **01** (2007) 013, [hep-ph/0611129].

[75] S. Hoeche, F. Krauss, N. Lavesson, L. Lonnblad, M. Mangano, A. Schalicke et al., *Matching parton showers and matrix elements*, in *HERA and the LHC: A Workshop on the implications of HERA for LHC physics: Proceedings Part A*, 2006. hep-ph/0602031.

[76] J. Alwall et al., *Comparative study of various algorithms for the merging of parton showers and matrix elements in hadronic collisions*, *Eur. Phys. J.* **C53** (2008) 473–500, [0706.2569].

[77] DELPHES 3 collaboration, J. de Favereau, C. Delaere, P. Demin, A. Giammanco, V. Lemaître, A. Mertens et al., *DELPHES 3, A modular*

framework for fast simulation of a generic collider experiment, *JHEP* **02** (2014) 057, [1307.6346].

[78] CMS collaboration, S. Chatrchyan et al., *Identification of b-quark jets with the CMS experiment*, *JINST* **8** (2013) P04013, [1211.4462].

[79] S. Catani, L. Cieri, G. Ferrera, D. de Florian and M. Grazzini, *Vector boson production at hadron colliders: a fully exclusive QCD calculation at NNLO*, *Phys. Rev. Lett.* **103** (2009) 082001, [0903.2120].

[80] M. Grazzini, S. Kallweit, D. Rathlev and M. Wiesemann, *$W^{\pm}Z$ production at hadron colliders in NNLO QCD*, *Phys. Lett.* **B761** (2016) 179–183, [1604.08576].

[81] J. M. Campbell, R. K. Ellis and C. Williams, *Vector boson pair production at the LHC*, *JHEP* **07** (2011) 018, [1105.0020].

[82] D. T. Nhung, L. D. Ninh and M. M. Weber, *NLO corrections to WWZ production at the LHC*, *JHEP* **12** (2013) 096, [1307.7403].

[83] C. Muselli, M. Bonvini, S. Forte, S. Marzani and G. Ridolfi, *Top Quark Pair Production beyond NNLO*, *JHEP* **08** (2015) 076, [1505.02006].

[84] A. Das, P. Konar and S. Majhi, *Production of Heavy neutrino in next-to-leading order QCD at the LHC and beyond*, *JHEP* **06** (2016) 019, [1604.00608].

[85] C. Degrande, O. Mattelaer, R. Ruiz and J. Turner, *Fully-Automated Precision Predictions for Heavy Neutrino Production Mechanisms at Hadron Colliders*, *Phys. Rev.* **D94** (2016) 053002, [1602.06957].

[86] D. Adams et al., *Towards an Understanding of the Correlations in Jet Substructure*, *Eur. Phys. J.* **C75** (2015) 409, [1504.00679].

[87] M. Cacciari and G. P. Salam, *Dispelling the N^3 myth for the k_t jet-finder*, *Phys. Lett.* **B641** (2006) 57–61, [hep-ph/0512210].

[88] CMS collaboration, V. Khachatryan et al., *Identification techniques for highly boosted W bosons that decay into hadrons*, *JHEP* **12** (2014) 017, [1410.4227].

[89] M. Wobisch and T. Wengler, *Hadronization corrections to jet cross-sections in deep inelastic scattering*, in *Monte Carlo generators for HERA physics. Proceedings, Workshop, Hamburg, Germany, 1998-1999*, pp. 270–279, 1998. hep-ph/9907280.

[90] C. G. Lester and D. J. Summers, *Measuring masses of semiinvisibly decaying particles pair produced at hadron colliders*, *Phys. Lett.* **B463** (1999) 99–103, [hep-ph/9906349].

[91] W. S. Cho, K. Choi, Y. G. Kim and C. B. Park, *Gluino Stransverse Mass*, *Phys. Rev. Lett.* **100** (2008) 171801, [0709.0288].

[92] A. J. Barr, T. J. Khoo, P. Konar, K. Kong, C. G. Lester, K. T. Matchev et al., *Guide to transverse projections and mass-constraining variables*, *Phys. Rev.* **D84** (2011) 095031, [1105.2977].

[93] M. Burns, K. Kong, K. T. Matchev and M. Park, *Using Subsystem MT2 for Complete Mass Determinations in Decay Chains with Missing Energy at Hadron Colliders*, *JHEP* **03** (2009) 143, [0810.5576].

[94] P. Konar, K. Kong, K. T. Matchev and M. Park, *Dark Matter Particle Spectroscopy at the LHC: Generalizing M(T2) to Asymmetric Event Topologies*, *JHEP* **04** (2010) 086, [0911.4126].

[95] J. H. Kim, K. Kong, K. T. Matchev and M. Park, *Probing the Triple Higgs Self-Interaction at the Large Hadron Collider*, *Phys. Rev. Lett.* **122** (2019) 091801, [1807.11498].

[96] https://twiki.cern.ch/twiki/pub/Main/ABCDMethod/ABCDGuide_draft18Oct18.pdf.

[97] A. Das, P. Konar and A. Thalapillil, *Jet substructure shedding light on heavy Majorana neutrinos at the LHC*, *JHEP* **02** (2018) 083, [1709.09712].

[98] P. S. B. Dev, A. Pilaftsis and U.-k. Yang, *New Production Mechanism for Heavy Neutrinos at the LHC*, *Phys. Rev. Lett.* **112** (2014) 081801, [1308.2209].

[99] D. Alva, T. Han and R. Ruiz, *Heavy Majorana neutrinos from $W\gamma$ fusion at hadron colliders*, *JHEP* **02** (2015) 072, [1411.7305].

[100] A. Atre, T. Han, S. Pascoli and B. Zhang, *The Search for Heavy Majorana Neutrinos*, *JHEP* **05** (2009) 030, [0901.3589].

[101] E. Nardi, E. Roulet and D. Tommasini, *Limits on neutrino mixing with new heavy particles*, *Phys. Lett.* **B327** (1994) 319–326, [hep-ph/9402224].

[102] E. Nardi, E. Roulet and D. Tommasini, *New neutral gauge bosons and new heavy fermions in the light of the new LEP data*, *Phys. Lett.* **B344** (1995) 225–232, [hep-ph/9409310].

[103] J. de Blas, *Electroweak limits on physics beyond the Standard Model*, *EPJ Web Conf.* **60** (2013) 19008, [1307.6173].

[104] F. del Aguila, J. de Blas and M. Perez-Victoria, *Effects of new leptons in Electroweak Precision Data*, *Phys. Rev.* **D78** (2008) 013010, [0803.4008].

[105] E. Akhmedov, A. Kartavtsev, M. Lindner, L. Michaels and J. Smirnov, *Improving Electro-Weak Fits with TeV-scale Sterile Neutrinos*, *JHEP* **05** (2013) 081, [1302.1872].

[106] A. Bhardwaj, P. Konar, T. Mandal and S. Sadhukhan, *Probing the inert doublet model using jet substructure with a multivariate analysis*, *Phys. Rev. D* **100** (2019) 055040, [1905.04195].

[107] A. Belyaev, G. Cacciapaglia, I. P. Ivanov, F. Rojas-Abatte and M. Thomas, *Anatomy of the Inert Two Higgs Doublet Model in the light*

of the LHC and non-LHC Dark Matter Searches, Phys. Rev. **D97** (2018) 035011, [1612.00511].

[108] J. Chakrabortty, P. Konar and T. Mondal, *Copositive Criteria and Boundedness of the Scalar Potential*, Phys. Rev. **D89** (2014) 095008, [1311.5666].

[109] I. F. Ginzburg, K. A. Kanishev, M. Krawczyk and D. Sokolowska, *Evolution of Universe to the present inert phase*, Phys. Rev. **D82** (2010) 123533, [1009.4593].

[110] B. Świeżewska, *Yukawa independent constraints for two-Higgs-doublet models with a 125 GeV Higgs boson*, Phys. Rev. **D88** (2013) 055027, [1209.5725].

[111] M. E. Peskin and T. Takeuchi, *Estimation of oblique electroweak corrections*, Phys. Rev. **D46** (1992) 381–409.

[112] Particle Data Group collaboration, *Review of particle physics*, Phys. Rev. D **98** (Aug, 2018) 030001.

[113] A. Arhrib, R. Benbrik and N. Gaur, *$H \to \gamma\gamma$ in Inert Higgs Doublet Model*, Phys. Rev. **D85** (2012) 095021, [1201.2644].

[114] B. Swiezewska and M. Krawczyk, *Diphoton rate in the inert doublet model with a 125 GeV Higgs boson*, Phys. Rev. **D88** (2013) 035019, [1212.4100].

[115] ATLAS, CMS collaboration, G. Aad et al., *Measurements of the Higgs boson production and decay rates and constraints on its couplings from a combined ATLAS and CMS analysis of the LHC pp collision data at $\sqrt{s} = 7$ and 8 TeV*, JHEP **08** (2016) 045, [1606.02266].

[116] ATLAS collaboration, G. Aad et al., *Measurements of the Higgs boson production and decay rates and coupling strengths using pp collision data at $\sqrt{s} = 7$ and 8 TeV in the ATLAS experiment*, Eur. Phys. J. **C76** (2016) 6, [1507.04548].

[117] E. Lundstrom, M. Gustafsson and J. Edsjo, *The Inert Doublet Model and LEP II Limits*, *Phys. Rev.* **D79** (2009) 035013, [0810.3924].

[118] G. Belanger, B. Dumont, A. Goudelis, B. Herrmann, S. Kraml and D. Sengupta, *Dilepton constraints in the Inert Doublet Model from Run 1 of the LHC*, *Phys. Rev.* **D91** (2015) 115011, [1503.07367].

[119] A. Pierce and J. Thaler, *Natural Dark Matter from an Unnatural Higgs Boson and New Colored Particles at the TeV Scale*, *JHEP* **08** (2007) 026, [hep-ph/0703056].

[120] Planck collaboration, P. A. R. Ade et al., *Planck 2015 results. XIII. Cosmological parameters*, *Astron. Astrophys.* **594** (2016) A13, [1502.01589].

[121] G. Belanger, F. Boudjema, A. Pukhov and A. Semenov, *MicrOMEGAs: A Program for calculating the relic density in the MSSM*, *Comput. Phys. Commun.* **149** (2002) 103–120, [hep-ph/0112278].

[122] XENON100 collaboration, E. Aprile et al., *Dark Matter Results from 225 Live Days of XENON100 Data*, *Phys. Rev. Lett.* **109** (2012) 181301, [1207.5988].

[123] LUX collaboration, D. S. Akerib et al., *Results from a search for dark matter in the complete LUX exposure*, *Phys. Rev. Lett.* **118** (2017) 021303, [1608.07648].

[124] R. Barbieri, L. J. Hall and V. S. Rychkov, *Improved naturalness with a heavy Higgs: An Alternative road to LHC physics*, *Phys. Rev.* **D74** (2006) 015007, [hep-ph/0603188].

[125] J. Giedt, A. W. Thomas and R. D. Young, *Dark matter, the CMSSM and lattice QCD*, *Phys. Rev. Lett.* **103** (2009) 201802, [0907.4177].

[126] Y. Mambrini, *Higgs searches and singlet scalar dark matter: Combined constraints from XENON 100 and the LHC*, *Phys. Rev.* **D84** (2011) 115017, [1108.0671].

[127] A. Belyaev, T. R. Fernandez Perez Tomei, P. G. Mercadante, C. S. Moon, S. Moretti, S. F. Novaes et al., *Advancing LHC probes of dark matter from the inert two-Higgs-doublet model with the monojet signal*, *Phys. Rev.* **D99** (2019) 015011, [1809.00933].

[128] P. Poulose, S. Sahoo and K. Sridhar, *Exploring the Inert Doublet Model through the dijet plus missing transverse energy channel at the LHC*, *Phys. Lett.* **B765** (2017) 300–306, [1604.03045].

[129] D. Borah and A. Gupta, *New viable region of an inert Higgs doublet dark matter model with scotogenic extension*, *Phys. Rev.* **D96** (2017) 115012, [1706.05034].

[130] CMS collaboration, V. Khachatryan et al., *Search for disappearing tracks in proton-proton collisions at* $\sqrt{s} = 8$ *TeV*, *JHEP* **01** (2015) 096, [1411.6006].

[131] M. Krawczyk, D. Sokolowska, P. Swaczyna and B. Swiezewska, *Constraining Inert Dark Matter by* $R_{\gamma\gamma}$ *and WMAP data*, *JHEP* **09** (2013) 055, [1305.6266].

[132] S. Banerjee and N. Chakrabarty, *A revisit to scalar dark matter with radiative corrections*, *JHEP* **05** (2019) 150, [1612.01973].

[133] A. Alloul, N. D. Christensen, C. Degrande, C. Duhr and B. Fuks, *FeynRules 2.0 - A complete toolbox for tree-level phenomenology*, *Comput. Phys. Commun.* **185** (2014) 2250–2300, [1310.1921].

[134] C. Degrande, C. Duhr, B. Fuks, D. Grellscheid, O. Mattelaer and T. Reiter, *UFO - The Universal FeynRules Output*, *Comput. Phys. Commun.* **183** (2012) 1201–1214, [1108.2040].

[135] J. Pumplin, D. R. Stump, J. Huston, H. L. Lai, P. M. Nadolsky and W. K. Tung, *New generation of parton distributions with uncertainties from global QCD analysis*, *JHEP* **07** (2002) 012, [hep-ph/0201195].

[136] https://cp3.irmp.ucl.ac.be/projects/madgraph/wiki/FAQ-General-13.

[137] https://cp3.irmp.ucl.ac.be/projects/madgraph/wiki/IntroMatching.

[138] CMS collaboration, V. Khachatryan et al., *Search for dark matter in proton-proton collisions at 8 TeV with missing transverse momentum and vector boson tagged jets*, *JHEP* **12** (2016) 083, [1607.05764].

[139] ATLAS collaboration, M. Aaboud et al., *Search for dark matter in events with a hadronically decaying vector boson and missing transverse momentum in pp collisions at $\sqrt{s} = 13$ TeV with the ATLAS detector*, *JHEP* **10** (2018) 180, [1807.11471].

[140] B. Hespel, D. Lopez-Val and E. Vryonidou, *Higgs pair production via gluon fusion in the Two-Higgs-Doublet Model*, *JHEP* **09** (2014) 124, [1407.0281].

[141] G. Balossini, G. Montagna, C. M. Carloni Calame, M. Moretti, O. Nicrosini, F. Piccinini et al., *Combination of electroweak and QCD corrections to single W production at the Fermilab Tevatron and the CERN LHC*, *JHEP* **01** (2010) 013, [0907.0276].

[142] N. Kidonakis, *Theoretical results for electroweak-boson and single-top production*, *PoS* **DIS2015** (2015) 170, [1506.04072].

[143] P. Konar, K. Kong and K. T. Matchev, *$\sqrt{\hat{s}}_{min}$: A Global inclusive variable for determining the mass scale of new physics in events with missing energy at hadron colliders*, *JHEP* **03** (2009) 085, [0812.1042].

[144] P. Konar, K. Kong, K. T. Matchev and M. Park, *RECO level $\sqrt{s}_{min}$ and subsystem $\sqrt{s}_{min}$: Improved global inclusive variables for measuring the new physics mass scale in E_T events at hadron colliders*, *JHEP* **06** (2011) 041, [1006.0653].

[145] A. Bhardwaj, J. Dutta, P. Konar, B. Mukhopadhyaya and S. K. Rai, *Boosted jet techniques for a supersymmetric scenario with gravitino LSP*, 2007.00351.

[146] J. Dutta, P. Konar, S. Mondal, B. Mukhopadhyaya and S. K. Rai, *Search for a compressed supersymmetric spectrum with a light Gravitino*, *JHEP* **09** (2017) 026, [1704.04617].

[147] J. Dutta, B. Mukhopadhyaya and S. K. Rai, *Identifying a Higgsino-like NLSP in the context of a keV-scale gravitino LSP*, *Phys. Rev. D* **101** (2020) 075040, [1904.08906].

[148] S. P. Martin, *A Supersymmetry primer*, hep-ph/9709356.

[149] P. Meade, M. Reece and D. Shih, *Prompt Decays of General Neutralino NLSPs at the Tevatron*, *JHEP* **05** (2010) 105, [0911.4130].

[150] L. Covi, J. Hasenkamp, S. Pokorski and J. Roberts, *Gravitino Dark Matter and general neutralino NLSP*, *JHEP* **11** (2009) 003, [0908.3399].

[151] K. T. Matchev and S. D. Thomas, *Higgs and Z boson signatures of supersymmetry*, *Phys. Rev.* **D62** (2000) 077702, [hep-ph/9908482].

[152] W. Porod and F. Staub, *SPheno 3.1: Extensions including flavour, CP-phases and models beyond the MSSM*, *Comput. Phys. Commun.* **183** (2012) 2458–2469, [1104.1573].

[153] W. Porod, *SPheno, a program for calculating supersymmetric spectra, SUSY particle decays and SUSY particle production at e+ e- colliders*, *Comput. Phys. Commun.* **153** (2003) 275–315, [hep-ph/0301101].

[154] ATLAS collaboration, M. Aaboud et al., *Search for pair production of higgsinos in final states with at least three b-tagged jets in $\sqrt{s} = 13$ TeV pp collisions using the ATLAS detector*, *Submitted to: Phys. Rev.* (2018) , [1806.04030].

[155] CMS collaboration, A. M. Sirunyan et al., *Combined search for electroweak production of charginos and neutralinos in proton-proton collisions at* $\sqrt{s} = 13$ *TeV*, *JHEP* **03** (2018) 160, [1801.03957].

[156] CMS collaboration, A. M. Sirunyan et al., *Search for Physics Beyond the Standard Model in Events with High-Momentum Higgs Bosons and Missing Transverse Momentum in Proton-Proton Collisions at 13 TeV*, *Phys. Rev. Lett.* **120** (2018) 241801, [1712.08501].

[157] ATLAS collaboration, M. Aaboud et al., *Search for supersymmetry in events with four or more leptons in* $\sqrt{s} = 13$ *TeV pp collisions with ATLAS*, 1804.03602.

[158] ATLAS collaboration, M. Aaboud et al., *Search for squarks and gluinos in final states with jets and missing transverse momentum using 36 fb*$^{-1}$ *of* $\sqrt{s} = 13$ *TeV pp collision data with the ATLAS detector*, *Phys. Rev. D* **97** (2018) 112001, [1712.02332].

[159] CMS Collaboration collaboration, *Search for supersymmetry in proton-proton collisions at 13 TeV in final states with jets and missing transverse momentum*, Tech. Rep. CMS-PAS-SUS-19-006, CERN, Geneva, 2019.

[160] ATLAS collaboration, M. Aaboud et al., *Search for chargino and neutralino production in final states with a Higgs boson and missing transverse momentum at* $\sqrt{s} = 13$ *TeV with the ATLAS detector*, 1812.09432.

[161] ATLAS Collaboration collaboration, *Search for direct production of electroweakinos in final states with one lepton, missing transverse momentum and a Higgs boson decaying into two b-jets in pp collisions at* $\sqrt{s} = 13$ *TeV with the ATLAS detector*, Tech. Rep. ATLAS-CONF-2019-031, CERN, Geneva, Jul, 2019.

[162] ATLAS collaboration, https://atlas.web.cern.ch/Atlas/GROUPS/PHYSICS/CombinedSummaryPlots/SUSY/ATLAS_SUSY_EWSummary_higgsino/ATLAS_SUSY_EWSummary_higgsino.png.

[163] CMS collaboration, http://cms-results.web.cern.ch/cms-results/public-results/publications/SUS-17-004/CMS-SUS-17-004_Figure_012.png.

[164] CMS collaboration, A. M. Sirunyan et al., *Search for Higgsino pair production in pp collisions at $\sqrt{s}$ = 13 TeV in final states with large missing transverse momentum and two Higgs bosons decaying via $H \to b\bar{b}$*, *Phys. Rev. D* **97** (2018) 032007, [1709.04896].

[165] J. Dutta, P. Konar, S. Mondal, B. Mukhopadhyaya and S. K. Rai, *A Revisit to a Compressed Supersymmetric Spectrum with 125 GeV Higgs*, *JHEP* **01** (2016) 051, [1511.09284].

[166] A. Arbey, M. Battaglia, L. Covi, J. Hasenkamp and F. Mahmoudi, *LHC constraints on Gravitino Dark Matter*, *Phys. Rev.* **D92** (2015) 115008, [1505.04595].

[167] L. Covi, M. Olechowski, S. Pokorski, K. Turzynski and J. D. Wells, *Supersymmetric mass spectra for gravitino dark matter with a high reheating temperature*, *JHEP* **01** (2011) 033, [1009.3801].

[168] M. Viel, J. Lesgourgues, M. G. Haehnelt, S. Matarrese and A. Riotto, *Constraining warm dark matter candidates including sterile neutrinos and light gravitinos with WMAP and the Lyman-alpha forest*, *Phys. Rev.* **D71** (2005) 063534, [astro-ph/0501562].

[169] E. A. Baltz and H. Murayama, *Gravitino warm dark matter with entropy production*, *JHEP* **05** (2003) 067, [astro-ph/0108172].

[170] A. Boyarsky, J. Lesgourgues, O. Ruchayskiy and M. Viel, *Lyman-alpha constraints on warm and on warm-plus-cold dark matter models*, *JCAP* **0905** (2009) 012, [0812.0010].

[171] D. Dercks, N. Desai, J. S. Kim, K. Rolbiecki, J. Tattersall and T. Weber, *CheckMATE 2: From the model to the limit*, Comput. Phys. Commun. **221** (2017) 383–418, [1611.09856].

[172] CMS collaboration, *Identification of double-b quark jets in boosted event topologies*, .

[173] R. Brun and F. Rademakers, *ROOT: An object oriented data analysis framework*, Nucl. Instrum. Meth. **A389** (1997) 81–86.

[174] R. D. Ball et al., *Parton distributions with LHC data*, Nucl. Phys. B **867** (2013) 244–289, [1207.1303].

[175] W. Beenakker, R. Hopker and M. Spira, *PROSPINO: A Program for the production of supersymmetric particles in next-to-leading order QCD*, hep-ph/9611232.

[176] T. Plehn, *Measuring the MSSM Lagrangean*, *Czech. J. Phys.* **55** (2005) B213–B220, [hep-ph/0410063].

[177] M. Spira, *Higgs and SUSY particle production at hadron colliders*, in *Supersymmetry and unification of fundamental interactions. Proceedings, 10th International Conference, SUSY'02, Hamburg, Germany, June 17-23, 2002*, pp. 217–226, 2002. hep-ph/0211145.

[178] W. Beenakker, M. Kramer, T. Plehn, M. Spira and P. M. Zerwas, *Stop production at hadron colliders*, Nucl. Phys. **B515** (1998) 3–14, [hep-ph/9710451].

[179] W. Beenakker, R. Hopker, M. Spira and P. M. Zerwas, *Squark and gluino production at hadron colliders*, Nucl. Phys. **B492** (1997) 51–103, [hep-ph/9610490].

[180] A. Bhardwaj, P. Konar, P. Sharma and A. K. Swain, *Exploring CP phase in τ-lepton Yukawa coupling in Higgs decays at the LHC*, J. Phys. G **46** (2019) 105001, [1612.01417].

[181] K. Hagiwara, T. Li, K. Mawatari and J. Nakamura, *TauDecay: a library to simulate polarized tau decays via FeynRules and MadGraph5*, *Eur. Phys. J.* **C73** (2013) 2489, [1212.6247].

[182] T. Sjostrand, S. Mrenna and P. Z. Skands, *A Brief Introduction to PYTHIA 8.1*, *Comput. Phys. Commun.* **178** (2008) 852–867, [0710.3820].

[183] M. Kramer, J. H. Kuhn, M. L. Stong and P. M. Zerwas, *Prospects of measuring the parity of Higgs particles*, *Z. Phys.* **C64** (1994) 21–30, [hep-ph/9404280].

[184] S. Berge, W. Bernreuther and J. Ziethe, *Determining the CP parity of Higgs bosons at the LHC in their tau decay channels*, *Phys. Rev. Lett.* **100** (2008) 171605, [0801.2297].

[185] R. Ellis, I. Hinchliffe, M. Soldate and J. V. D. Bij, *Higgs decay to $\tau^+\tau^-$ a possible signature of intermediate mass higgs bosons at high energy hadron colliders*, *Nuclear Physics B* **297** (1988) 221 – 243.

[186] S. Maruyama, *Stochastic mass-reconstruction: a new technique to reconstruct resonance masses of heavy particles decaying into tau lepton pairs*, 1512.04842.

[187] A. Elagin, P. Murat, A. Pranko and A. Safonov, *A New Mass Reconstruction Technique for Resonances Decaying to di-tau*, *Nucl. Instrum. Meth.* **A654** (2011) 481–489, [1012.4686].

[188] L.-G. Xia, *An improved mass reconstruction technique for a heavy resonance decaying to $\tau^+\tau^-$*, 1601.02454.

[189] B. Gripaios, K. Nagao, M. Nojiri, K. Sakurai and B. Webber, *Reconstruction of Higgs bosons in the di-tau channel via 3-prong decay*, *JHEP* **03** (2013) 106, [1210.1938].

[190] A. K. Swain and P. Konar, *Constrained $\sqrt{\hat{S}_{min}}$ and reconstructing with semi-invisible production at hadron colliders*, *JHEP* **1503** (2015) 142, [1412.6624].

[191] P. Konar and A. K. Swain, *Mass reconstruction with M_2 under constraint in semi-invisible production at a hadron collider*, *Phys. Rev.* **D93** (2016) 015021, [1509.00298].

[192] P. Konar and A. K. Swain, *Reconstructing semi-invisible events in resonant tau pair production from Higgs*, *Phys. Lett.* **B757** (2016) 211–215, [1602.00552].

[193] K. Hagiwara, K. Ma and S. Mori, *Probing CP violation in $h \to \tau^- \tau^+$ at the LHC*, 1609.00943.

[194] ATLAS collaboration, M. Aaboud et al., *Reconstruction of primary vertices at the ATLAS experiment in Run 1 proton–proton collisions at the LHC*, *Eur. Phys. J.* **C77** (2017) 332, [1611.10235].

[195] ATLAS collaboration, G. Aad et al., *Evidence for the Higgs-boson Yukawa coupling to tau leptons with the ATLAS detector*, *JHEP* **04** (2015) 117, [1501.04943].